Artificial Kitaev chains in Two-Dimensional Electron Gases

Wang, Q.

DOI
10.4233/uuid:89e0dda2-685d-459f-9d8a-472c6b1ba747

Publication date
2025

Document Version
Final published version

Citation (APA)
Wang, Q. (2025). *Artificial Kitaev chains in Two-Dimensional Electron Gases*. [Dissertation (TU Delft), Delft University of Technology]. https://doi.org/10.4233/uuid:89e0dda2-685d-459f-9d8a-472c6b1ba747

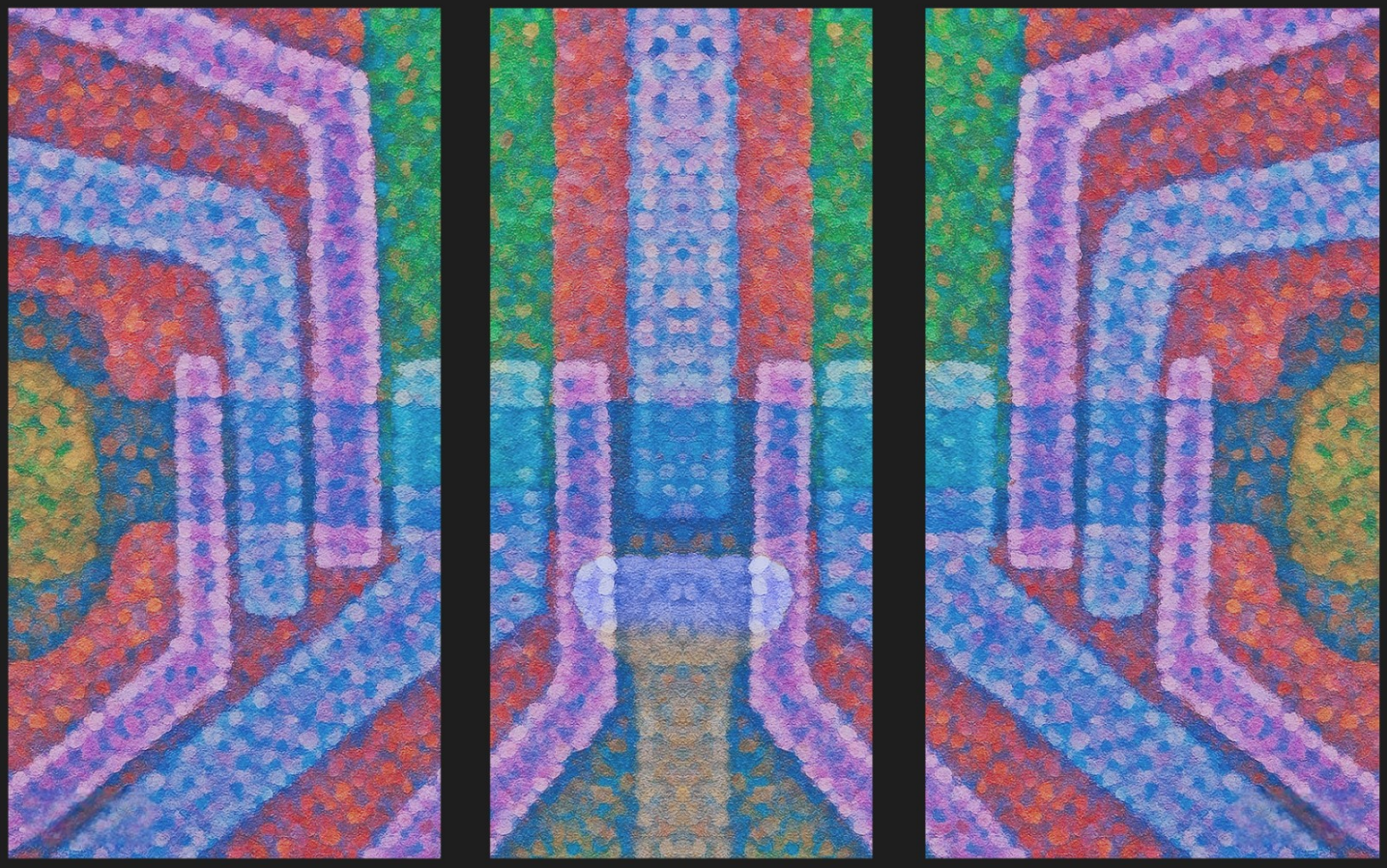

Artificial Kitaev Chains

in Two-Dimensional Electron Gases

Qingzhen Wang

Artificial Kitaev chains in Two-Dimensional Electron Gases

Artificial Kitaev chains in Two-Dimensional Electron Gases

Dissertation

for the purpose of obtaining the degree of doctor
at Delft University of Technology
by the authority of the Rector Magnificus, prof.dr.ir. T.H.J.J van der Hagen, chair of the Board for Doctorates
to be defended publicly on
Tuesday 9th September 2025 at 12:30 o'clock

by

Qingzhen WANG

Master of Science in Materials Science,
RWTH Aachen, Germany,
born in Qingdao, China.

This dissertation has been approved by the promotors.

Composition of the doctoral committee:

Rector Magnificus,	Chairperson
Prof.dr.ir. L.P. Kouwenhoven,	Delft University of Technology, promotor
Dr. S. Goswami,	Delft University of Technology, copromotor
Independent members:	
Prof.dr. A.F. Otte,	Delft University of Technology
Prof.dr. Y.V. Nazarov,	Delft University of Technology
Prof.dr. F. Kuemmeth,	University of Regensburg, Germany
Dr. C.K. Andersen,	Delft University of Technology
Dr. G. Scappucci,	Delft University of Technology
Dr. M.T. Wimmer,	Delft University of Technology, reserve member

Keywords: Two dimensional electron gas, Majorana zero modes, hybrid quantum dot, Cooper pair splitter, Kitaev chain

Printed by: proefschriftenprinten.nl

Cover: Nanoelectronics in pointillism style.

Design by Yihan Li and Qingzhen Wang, powered by via BYLO.AI

ISBN 978-94-6384-830-5

An electronic version of this dissertation is available at https://repository.tudelft.nl/

To my parents and Yihan.

Contents

Summary

Majorana zero modes are neutral excitations—equal superpositions of an electron and a hole in a superconductor. Their non-Abelian statistics make them promising building blocks for topological quantum computation. In semiconductor–superconductor hybrids, however, disorder and trivial bound states often obscure Majorana signatures, making conclusive evidence elusive. This challenge motivates new device concepts or alternative engineering strategies.

In this thesis, we bridge a traditional and a new bottom-up routes to realize Majorana modes in two-dimensional electron gases (2DEGs), and develop a fabrication workflow for complex device geometries. We first implement the Lutchyn–Oreg approach in gate-defined wires and develop multiprobe spectroscopy with multiple tunnel probes to assess spatial uniformity. These measurements reveal subgap states that are often uncorrelated between neighboring probes, though some devices show striking probe-to-probe correlations. These observations indicate that disorder and inhomogeneity can drive inconsistent behavior across similar devices, limiting prospects for a robust global topological phase.

This motivates an alternative pathway: constructing artificial Kitaev chains using quantum dots. In the second experiment, we establish controllable elastic cotunneling and crossed Andreev reflection, via gate-tunable Andreev bound states that couple the dots. We demonstrate Cooper pair splitting and at finite magnetic field, we are able to resolve substantial triplet correlations due to the strong spin orbit coupling in the 2DEGs.

In the third experiment, we push the system into the strong-coupling regime and realize a two-site Kitaev chain. By tuning dot levels, the ABS energy, and the in-plane magnetic-field orientation, we reach "sweet spots" with correlated zero-bias peaks that are robust to local perturbations. Notably, these peaks can already appear at zero Zeeman energy—consistent with a spinful two-site chain. Comparing the full excitation spectrum to numerical simulations allows us to estimate the Majorana polarization in representative settings.

We conclude this thesis by outlining next steps: extending the Kitaev chain and implementing parity readout to enable manipulation and measurement of multiple MBSs. We also assess alternative material platforms for proof-of-principle Kitaev-chain devices.

Samenvatting

Majorana-nulmodi zijn neutrale excitaties—gelijke superposities van een elektron en een gat in een supergeleider. Door hun niet-Abelse statistiek gelden zij als veelbelovende bouwstenen voor topologische kwantumcomputatie. In halfgeleider–supergeleiderhybriden vertroebelen wanorde en triviale gebonden toestanden echter vaak de Majorana-signaturen, waardoor ondubbelzinnig bewijs uitblijft. Deze uitdaging motiveert nieuwe apparaatconcepten of alternatieve engineeringsstrategieën.

In dit proefschrift overbruggen wij een traditionele top-down benadering en een nieuwe bottom-up route om Majorana-modi in tweedimensionaal elektrongases (2DEGs) te realiseren, en ontwikkelen wij een fabricageworkflow voor complexe apparaatgeometrieën. Eerst implementeren we de Lutchyn–Oreg-aanpak in poortgedefinieerde draden en ontwikkelen we multiprobe-spectroscopie met meerdere tunnelprobes om de ruimtelijke uniformiteit te beoordelen. Deze metingen onthullen subgaptoestanden die vaak niet gecorreleerd zijn tussen naburige probes, al vertonen sommige apparaten opvallende correlaties van probe tot probe. Deze observaties wijzen erop dat wanorde en inhomogeniteit tot inconsistente responsen tussen vergelijkbare apparaten kunnen leiden, wat de vooruitzichten op een robuuste, globale topologische fase beperkt.

Dit motiveert een alternatieve route: het construeren van kunstmatige Kitaev-ketens met kwantumstippen. In het tweede experiment realiseren we controleerbare elastische cotunneling en gekruiste Andreev-reflectie via poort-tuneerbare Andreev-gebonden toestanden (ABSs) die de stippen koppelen. We demonstreren het splitsen van Cooperparen en, bij een eindig magneetveld, lossen we substantiële tripletcorrelaties op dankzij de sterke spin–baankoppeling in het 2DEG.

In het derde experiment brengen we het systeem in het sterke-koppelingregime en realiseren we een twee-site Kitaev-keten. Door de niveaus van de stippen, de ABS-energie en de in-vlakoriëntatie van het magneetveld te tunen bereiken we “sweet spots” met gecorreleerde nul-bias-pieken die robuust zijn tegen lokale verstoringen. Opmerkelijk genoeg kunnen deze pieken al verschijnen bij nul Zeeman-energie—consistent met een spinvolle twee-site-keten. Vergelijking van het volledige excitatiespectrum met numerieke simulaties stelt ons in staat de Majorana-polarisatie te schatten voor representatieve configuraties.

Tot slot schetsen we vervolgstappen: het verlengen van de Kitaev-keten en het implementeren van pariteitsuitlezing om manipulatie en meting van meerdere

MBS'en mogelijk te maken. Ook evalueren we alternatieve materiaalplatforms voor proof-of-principle-apparaten van Kitaev-ketens.

1

Introduction

In a speech from Richard Feynman in 1982: "Nature isn't classical, and if you want to make a simulation of Nature, you'd better make it quantum mechanical [1]. The pursuit of quantum computing is driven by its potential to solve problems intractable for even the most advanced classical supercomputers. Those problems which are classically hard but "quantumly" easy can be found in cryptography, search and optimization, simulation of quantum systems [2]. A qubit constitutes a fundamental unit of quantum information that exists in a superposition of $|0\rangle$ and $|1\rangle$. However, the inherent fragility of qubits presents significant challenges, as quantum information is highly susceptible to decoherence and noise from the environment. Due to short coherence times, encoding a logical qubit requires numerous physical qubits to mitigate errors. For example, Google's recent experiments demonstrated that approximately 100 superconducting qubits were necessary to encode a single logical qubit with improved coherence times [3]. This immense overhead remains a major bottleneck in the development of scalable quantum computers.

A promising alternative to mitigate this bottleneck is the concept of topological quantum computing, which is predicted to be intrinsically immune to environmental noise. The principle of topology is that certain global properties of a system remain unchanged under continuous deformations. If quantum states could be stored in such a manner, they would be naturally protected from small imperfections and environmental change.

The theoretical foundation of topological quantum computing was laid by Alexei Kitaev [4, 5],who proposed that exotic quasiparticles called Majorana bound states could serve as the building blocks of topological qubits. These Majorana modes, predicted to emerge in topological superconductors, obey non-Abelian statistics, meaning their exchange ("braiding") leads to a transformation between

1

the ground states in a robust way. This non-Abelian nature makes them prime candidates for robust quantum information storage and manipulation.

Over the past two decades, the pursuit of Majorana bound states has led to intense theoretical and experimental efforts, among platforms such as in fractional quantum Hall systems, magnetic adatoms on conventional superconductor and semiconductor-superconductor hybrids [6]. We want to focus on the semiconductor-superconductor heterostructure, because it holds great promise in realizing scalable and flexible architectures. The earlier studies in 2010s focus on the devices based on Lutchyn-Oreg model. However, despite the experimental signatures such as zero-bias conductance peaks or the *2e-1e* transitions in Coulomb peaks, subsequent studies revealed that disorder and alternative trivial states, such as Andreev bound states, can also lead to the observations of these results [7, 8]. Despite sophisticated improvements in device quality, the existence of Majorana modes in Microsoft's platform [9] remains highly controversial [10, 11].

Under this context, this dissertation aim to investigate two complementary approaches: one focuses on exploring novel device geometries to gain more understanding and provide conclusive evidence for the existence of Majorana bound states, while the other seeks to engineer Majorana modes through an alternative strategy—engineering the artificial Kitaev chain based on hybrid quantum dots.

In this thesis, Chapter 2 summarizes the key theoretical concepts of hybrid superconductor-semiconductor QD. We starts with the basics of QD-S system, including the atomic limit and ground state phase transition. We further explore two non-local processes in QD-S-QD system–crossed Andreev reflection and Elastic Co-tunnelling, focusing on filtering techniques and the tunability of their amplitudes. In strong coupling regime, the system eventually emulates a minimal Kitaev chain. We thus review the original Kitaev chain, analyze the eigenstates in a two-site chain, and conclude with a case study on a spinful two-site Kitaev chain at zero magnetic field.

Chapter 3 concerns the nanofabrication techniques of the devices made in this dissertation. We start with introducing the InSbAs 2DEG with epitaxially grown aluminium as the major material platform, and then discuss the fabrication steps for a simple spectroscopy devices, with a focus on selective aluminium etching and the contact materials. To make more advanced devices with new geometries, we implement fabrication procedures with multiple dielectric and gate layers, and stress the design and challenges. We finish the chapter by discussing the challenges in optimizing selective Al etching.

In Chapter 4, we give a brief introduction to the Lutchyn-Oreg before presenting the results. We investigate the spatial uniformity of a gate-defined hybrid wire using a new type of device geometry – the multiprobe device. The microscopic

material parameters vary significantly along the wire for one device, while some other devices exhibit striking correlations in local density of states and thus uniform material properties. We discuss potential sources of these variations.

In Chapter 5, we demonstrate Cooper pair splitting in a semiconductor two-dimensional electron gas using quantum dots coupled to a superconductor-semiconductor hybrid region. By operating the QDs as charge filters, we achieve efficient CPS. By lifting the spin degeneracy and operating the QDs as spin filteres, we reveal both conventional singlet pairing and significant triplet correlations due to strong spin-orbit interaction.

Chapter 6 is where we put everything together. We realize a two-site Kitaev chain in same device architecture in Chapter 5, but in a strong coupling regime. We tune the system to "sweet spots" where robust correlated zero-bias peaks appear, via either magnetic field rotating or gating. By tracking the energy spectrum, we estimate the Majorana polarization. Notably, correlated zero-bias peaks emerge even without a magnetic field, which connects with a spinful Kitaev chain in Chapter 2

Chapter 7 we discuss on prospective experiments, such as extension of the Kitaev chain and the techniques for parity-readout, both paving the way towards advanced experiments require manipulation and readout of multiple MBSs. Furthermore, we examine the suitability of alternative material platforms and discuss whether they could serve as viable candidates for studying Kitaev chain physics.

2

Theory

I...a universe of atoms...an atom in the universe.

Richard P. Feynman

In this chapter I present the essential theoretical background supporting the following experimental chapters. I assume the readers are familiar with the fundamentals of solid state band theory, quantum transport in low-dimensional systems and the Bardeen-Cooper-Schrieffer (BCS) superconductivity.

2

2.1 QD-S: proximitized QD

The section is about the behavior of a quantum dot (QD) when it is in proximity to a superconductor (S). We first introduce semiconductor QD and Andreev bound states (ABSs), two essential elements in our studies. We then study the hybrid QD-S system under varying coupling strengths within the atomic limit. In the regime, the interplay between charging energy and the superconducting pairing potential leads to a distinct ground-state phase transition. We conclude by discussing the effect of an external Zeeman field and the limitation of the atomic limit assumptions.

2.1.1 Semiconductor QD

For a small and isolated semiconductor QD, where the electrons are confined in all three dimensions, both charge quantization and quantum confinement play signanificant roles [12]. The former is due to the Coulomb interaction and is characterized by the charging energy E_c, which is the energy cost to add an additional charge into the system:

$$E_c = e^2/C \tag{2.1}$$

where C is the total capacitance of the system. The latter is characterized by the so-called level spacing ΔE and becomes significant once the the system size approaches the Fermi wavelength, which is at the order of 100 nm for semiconductors. For a QD of size L in a semiconductor 2DEG heterostructure, the level spacing ΔE at the Fermi energy E_F is given by [13]:

$$\Delta E = \frac{1}{\pi}\frac{\hbar^2\pi^2}{m^* L^2} \tag{2.2}$$

where $\hbar$ is the reduced Plank constant and m^* the effective mass. Therefore, the smaller the QD size, the larger the level spacing. Note that the spin degeneracy has already been included in this value. For an orbital level with a two-fold spin degeneracy, this then implies that the filling of the first electron requires an energy cost of $\Delta E + E_c$, but the second electron only needs to overcome merely the E_c.

Experimentally, QDs are laterally confined by the metallic gates that are capacitively coupled to the semiconductor region via a thin layer of dielectric with a capacitance C_G. The metallic gate have an applied gate voltage V_G. Rather than working with the absolute free energy $E(N) = \frac{E_c}{2}(N - n_g)^2$, it is more practical to describe the electron transport in the QD using the energy difference between two

charge states, i.e. the electrochemical potential μ_N [13]:

$$\mu(N) \equiv E(N) - E(N-1) = E_c(N - n_g - \frac{1}{2}) + \epsilon_N \tag{2.3}$$

where E_c is the charging energy, N the number of electrons in the ground state at given gate voltages, $n_g \equiv (C_S V_S + C_G V_G)/e$ the gate induced charge , ϵ_N the orbital energy of the N-the occupied electron.

There are a few advantages of using μ to describe the quantum transport. First, the linear dependence of μ on the applied voltages makes it easy to convert between the change in the V_g and change in μ, up to a prefactor $\alpha \equiv \frac{eC_g}{C}$, which is known as the *lever arm* [14]. Secondly, the electron transfer can be visualized easily now with an energy diagram. Charge can only flow if the electro-chemical potential μ of a dot level lies within the bias window, which is the difference between the source and drain bias energies. Otherwise, the transport is blocked and no current flows through the QD.

At a fixed gate voltages configuration, the *change* of electrochemical potential by adding a new electron corresponds to the addition energy E_{add}

$$E_{\text{add}} \equiv \mu(N) - \mu(N-1) = E_c + \Delta E \tag{2.4}$$

where ΔE is the level spacing introduced before. This energy scale takes both the Coulomb effect and the quantum confinement into account. If the bias window becomes larger than the E_{add}, then electrons can always transfer between the source and drain due to the presence of at least one level within the bias window.

2.1.2 ANDREEV BOUND STATE

Before analyzing a QD in proximity to a superconductor, we first examine the effects at the normal-superconductor (N-S) interface. A coherent process known as Andreev reflection (AR) can occur. In a microscopic picture, incident electrons with an excitation energies less than the superconducting gap Δ are retro-reflected as holes in the normal section, while transmitting another Cooper pair into the superconductor. The holes therefore inherit the same superconducting phase and become quantum mechanically correlated with the incident electrons. As a result, the pairing potential from the superconductor leak into the normal material, a phenomenon known as the proximity effect [15, 16].

As the hole traves away from the interface, the phase information is lost over the distance characterized by the phase coherence length. However, if the normal section is sufficiently confined, the reflected holes can bounce back and undergo a second AR at the same N-S interface. If the phase coherence is preserved, this leads to the formation of ABS. Such a bound state can occur for example when the single level in a semiconductor QD is proximitized by the superconductor.

This hybrid system has been extensively studied [17–19]. In the following we introduce a theoretical framework for the QD-S system, whose transport properties are essential for engineering Cooper pair splitters and the Kitaev chain later in this chapter.

2.1.3 The atomic limit

The basic element of the system is shown in Figure 2.1a. We consider a single spin-degenerate level in a QD, tunnel coupled to a superconductor with a superconducting gap of Δ. The system can be described with the following Hamiltonian:

$$H = H_{QD} + H_S + H_t \tag{2.5}$$

where H_{QD} is the Hamiltonian of the normal QD, H_S the superconductor and H_t the coupling term. Using the second-quantization formalism, we define d_σ as the annihilation operator for the electron with the spin $\sigma =\uparrow$ or $\downarrow$). The Hamiltonian of the QD then reads:

$$H_{\mathrm{QD}} = \mu \sum_{\sigma=\uparrow,\downarrow} d_\sigma^\dagger d_\sigma + E_Z(d_\uparrow^\dagger d_\uparrow - d_\downarrow^\dagger d_\downarrow) + U n_\uparrow n_\downarrow \tag{2.6}$$

where $U(= E_c)$ is the Coulomb interaction term, $E_Z = g\mu_B B$ the Zeeman energy, and $n_\sigma = d_\sigma^\dagger d_\sigma$ the number operator. A single level implies that the dot can only be occupied with 0, 1 or 2 electrons. Therefore, for convenience here we re-define $\mu \equiv \mu(N = 1) = E_c(-n_g + 1/2)$ to better relate μ with n_g.

The superconductor is described with the effective mean-field BCS Hamiltonian [20, 21]:

$$H_{\mathrm{S}} = \sum_{\mathbf{k},\sigma} \epsilon_{\mathbf{k}} c_{\mathbf{k},\sigma}^\dagger c_{\mathbf{k},\sigma} - \sum_{\mathbf{k}} \Delta c_{\mathbf{k},\uparrow}^\dagger c_{-\mathbf{k},\downarrow}^\dagger + \Delta^* c_{-\mathbf{k},\downarrow} c_{\mathbf{k},\uparrow} \tag{2.7}$$

where $\epsilon_{\mathbf{k}}$ is the single-particle kinetic energies and Δ the order parameter. The $c_{\mathbf{k},\sigma}$ with crystal momentum $\mathbf{k}$ and spin σ ($\sigma \in \uparrow, \downarrow$) are the same annihilation operators as d_σ, but for the quasi-particles within the superconductor.

Finally, the tunnelling Hamiltonian between the QD and the superconductor reads:

$$H_{\mathrm{t}} = t_S \sum_{\mathbf{k},\sigma} d_\sigma^\dagger c_{\mathbf{k},\sigma} + c_{\mathbf{k},\sigma}^\dagger d_\sigma \tag{2.8}$$

where t_S is the real, constant tunnel rate between the dot level and all quasi-particles in the superconductor. Note that only spin-conserving processes are considered here. The spin-flipping events due to the presence of the spin-orbit coupling is discussed later in the chapter.

To solve the Hamiltonian, two approximations can be introduced to describe the system in the so-called superconducting atomic limit, without losing much of the insight.

A brief summary of [19, 22, 23]is presented here. The first assumption is to replace the entire quasi-particle continuum with one pair of electrons with the excitation energy Δ. This is called the zero-bandwidth limit (ZBW) and can be justified by considering the energy spectrum of a superconductor. The quasi-particles at $\pm\Delta$ have the lowest excitation energy and also diverging density of states. As the QD levels are ideally at sub-gap energies, these electrons at $\pm\Delta$ thus contribute the most to the tunnelling events between the QD level and the superconductor. The new H_S^{ZBW} and H_t^{ZBW} can be written as:

$$\begin{aligned} H_S^{\mathrm{ZBW}} &= \Delta c_\uparrow^\dagger c_\downarrow^\dagger + \Delta c_\downarrow c_\uparrow \\ H_t^{\mathrm{ZBW}} &= t_S \sum_\sigma d_\sigma^\dagger c_\sigma + c_\sigma^\dagger d_\sigma \end{aligned} \tag{2.9}$$

The second approximation is to consider the limit $\Delta \to \infty$. This prohibits the single-electron exchange between the QD and the superconductor and only allows the second-order tunnelling term, namely the transfer of a Cooper pair. This process virtually excites a quasi-particle to the superconducting gap edge, which then relaxes to the ground state by receiving another electron and forming a Cooper pair at the Fermi energy. Now, in this so-called superconducting atomic limit, the effect of the superconductor can be absorbed in the coupling term Γ_S and the effective Hamiltonian of the whole system H_{eff} reads:

$$\begin{aligned} H_{\mathrm{eff}} &= H_{QD} + \Gamma_S(d_\uparrow^\dagger d_\downarrow^\dagger + d_\uparrow^\dagger d_\downarrow^\dagger) \\ &= \mu \sum_\sigma d_\sigma^\dagger d_\sigma + E_Z(d_\uparrow^\dagger d_\uparrow - d_\downarrow^\dagger d_\downarrow) + U n_\uparrow n_\downarrow + \Gamma_S(d_\uparrow^\dagger d_\downarrow^\dagger + d_\uparrow^\dagger d_\downarrow^\dagger) \end{aligned} \tag{2.10}$$

where $\Gamma_S \equiv -\pi\rho_S|t_S|^2$, with ρ_S the normal density of states at the excitation energy of $= \pm\Delta$. Both ρ_S and t_S are assumed to be constant.

Before we solve the Hamiltonian and present a detailed interpretation of the results, it is insightful to compare Equation 2.10 with Equation 2.7. In the absence of Zeeman energy and charging energy, i.e. $E_Z = 0$ and $U = 0$, they share almost the same form. The role of Γ_S is therefore analogous to the order parameter Δ in the bulk superconductor. In other words, a larger Γ_S (due to large t_S) induces a stronger pairing correlation in the hybrid QD system, such that it favors even states (0- or 2-electron occupation) more than the odd states (1-electron occupation). Γ_S can also be viewed as the "induced gap" in the excitation picture, because it equals to the lowest energy of the excited states. This becomes clear and crucial in the situation where two or more proximitized QDs are strongly coupled to each other, such as in the case of an artificial Kitaev chain.

2.1.4 Ground state phase transition

In the many-particle formulation, the effective Hamiltonian H_{eff} can be written in a 4×4 matrix form with the basis $\{|0\rangle, |\uparrow\downarrow\rangle, |\uparrow\rangle, |\downarrow\rangle\}$:

$$H_{\text{eff}} = \begin{pmatrix} 0 & \Gamma_S & 0 & 0 \\ \Gamma_S & 2\mu+U & 0 & 0 \\ 0 & 0 & \mu+E_Z/2 & 0 \\ 0 & 0 & 0 & \mu-E_Z/2 \end{pmatrix} \tag{2.11}$$

Note that $|\uparrow\downarrow\rangle = d_\uparrow^\dagger d_\downarrow^\dagger |0\rangle$ fixes the choice of signs. The top-left block is the even state manifold, where the two basis states $|0\rangle$ and $|\uparrow\downarrow\rangle$ are coupled to each other by the finite Γ_S. Therefore, the eigenstates at a given coupling become the superposition of $|0\rangle$ and $|\uparrow\downarrow\rangle$. The bottom-right block is the manifold with odd parity states, $|\uparrow\rangle$ and $|\downarrow\rangle$, which are not affected by the presence of the superconductor.

The Hamiltonian is block diagonal and thus easily solvable. The eigenstates in the odd manifold are simply $|\uparrow\rangle$ and $|\downarrow\rangle$, and are collectively referred as the *doublet* with the eigenenergies:

$$E_{o\pm} = \mu \pm \frac{E_Z}{2} \tag{2.12}$$

The eigenstates in the even manifold are two *singlet* states. Conventionally, they are defined as $|S_-\rangle = u|0\rangle - v|\uparrow\downarrow\rangle$ and $|S_+\rangle = v|0\rangle + u|\uparrow\downarrow\rangle$. The u and v are BCS coherence factors defined as:

$$u^2 = 1-|v|^2 = \frac{1}{2}\left[1 + \frac{\mu+\frac{U}{2}}{\sqrt{(\mu+\frac{U}{2})^2+\Gamma_S^2}}\right] \tag{2.13}$$

The corresponding even state eigenenergies are

$$E_{e\pm} = \left(\mu+\frac{U}{2}\right) \pm \sqrt{(\mu+\frac{U}{2})^2+\Gamma_S^2} \tag{2.14}$$

Assuming for a moment that $|S_-\rangle$ is the system ground state, we can define:

$$\begin{aligned} E_{0-} &\equiv E_{o-} - E_{e-} \\ E_{0+} &\equiv E_{o+} - E_{e-} \end{aligned} \tag{2.15}$$

E_{0-} is the energy required for the lowest excitation $|S_-\rangle \to |\downarrow\rangle$, and E_{0+} for the second lowest excitation $|S_-\rangle \to |\uparrow\rangle$.

The state with the lowest energy between the singlet $|S_-\rangle$ and the doublet ($|\downarrow\rangle$) is the ground state of the system. In other words, a positive E_{0-} indicates a singlet ground state while a negative E_{0-} a doublet one. At $E_{0-} = 0$, the two states are

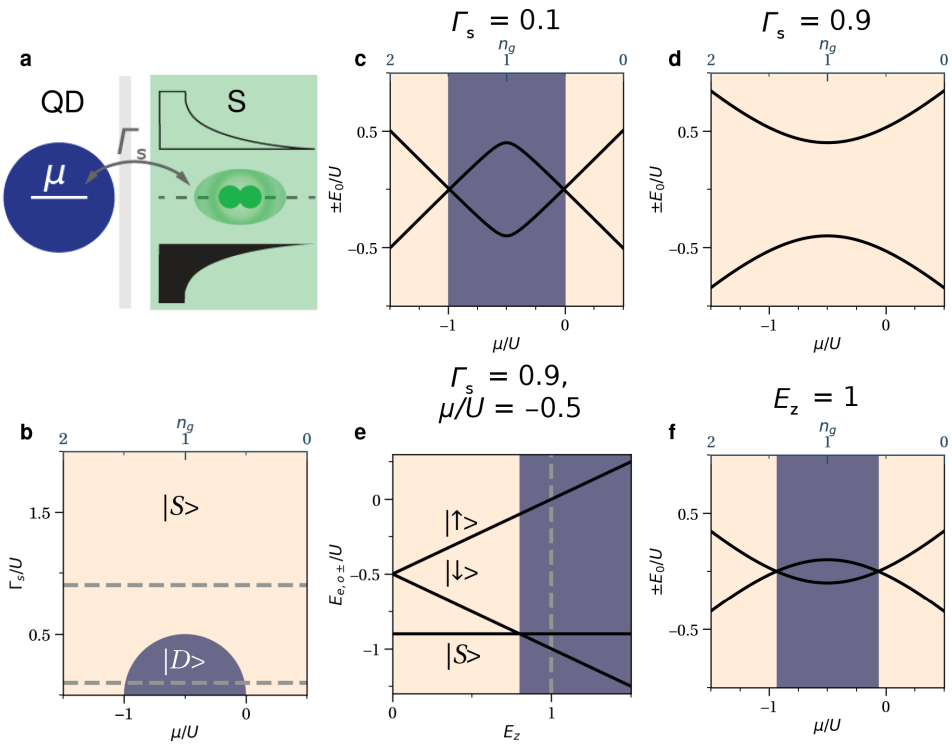

Figure 2.1: **Ground states transition in the QD-S system.(a)** A quantum dot level is coupled to a superconductor with a coupling parameter Γ_S. **(b)** The dome phase diagram. The corresponding charge number n_g is shown in the top axis. The singlet states (beige) and doublet states (purple) are color-coded. **(c)** With a smaller Γ_S, the ground state can switch from singlet to doublet, when the excitation energy E_0 crosses zero. **(d)** With a larger Γ_S, the ground state is always singlet. **(e)** The eigenenergies of the even and the odd states as a function of Zeeman energy E_z. **(f)** The singlet-doublet phase transition at $E_z = 1$

energetically degenerate and the boundary of the ground state phase transition is defined by its solution:

$$(\frac{\mu}{U}+\frac{1}{2})^2+(\frac{\Gamma_S}{U})^2=\frac{1}{4} \tag{2.16}$$

In the phase diagram plotted as a function of Γ_S and μ (both normalized with U), the area with a doublet ground state resembles the shape of a dome, as shown in Figure 2.1b. Now let us take a closer look on the effect of the external parameters on the ground state phase, starting with the Γ_S. If Γ_S is small, then there is a tight competition between the rather weak pairing potential and the Coulomb effect. The ground state thus alternate between singlet and doublet depending on the electrochemical potential μ (more intuitively, the induced gate charge n_g). In

Figure 2.1c, especially in the middle range around $n_g = 1$ (marked by the purple shade), the system always favors an odd ground state (doublet) to minimize its total energy. The addition of a second electron there is suppressed by the charging energy. As n_g moves towards to 0 or 2, the ground state eventually switches to the even states once E_0 reaches zero. This type of coupling and ground states switching behaviour is often referred as the Yu-Shiba-Rusinov (YSR) regime [24]. The name is earned due to the similar subgap conductance spectrum in this regime to that of a YSR-state, which was originally used to model a superconductor with a magnetic impurity.

Increasing Γ_S further lowers the energy of the even states, and consequently expands the range of μ where the ground state remains the singlet state. In the limit when $\Gamma_S \gtrsim U$, Cooper pairing tunnelling dominates over the Coulomb repulsion, and thus the system is always a BCS-like singlet, regardless of the original normal dot charge numbers. This scenario is depicted in Figure 2.1d with a large Γ_S above the dome. $|E_0|$ is always larger than zero in the whole range, and the ground state of the system remains an even state while changing the charge occupation from 0 to 2. This is often called the ABS limit.

So far, we have only considered the system at zero magnetic field. The singlet-doublet phase transition can also be driven by a finite Zeeman energy. As shown in Equation 2.12, the Zeeman energy E_Z splits the eigenenergies of the odd ground states $E_{o\pm}$, while leaving the $E_{e\pm}$ unaffected. Figure 2.1e shows that even for a system with sizable Γ_S, increasing the Zeeman energies lowers the energies of the spin $|\downarrow\rangle$ -state and it eventually becomes lower than the $|S\rangle$ at around $n_g = 1$. The evolution of E_0 as a function of μ for $E_Z = 1$ is shown in Figure 2.1f, confirming that the ground state has transited to a doublet at intermediate electrochemical potential. At regions where the expected dot charge number is even, however, the ground states remain even, as pair-wise electron transfer is still energetically preferable over single-electron charging.

The superconducting atomic limit offers an effective framework to understand the key physics in the QD-S system. However, some limitations cannot be ignored, especially in the context of QD-S-QD device to be discussed soon. First, the assumption of an infinite large superconducting gap is not realistic. The hybrid materials used throughout this thesis have an induced gap Δ_{ind} of about 250 μeV. This finite superconducting gap imposes an upper bound of the observable excitations, namely only those with $E_0 < \Delta_{\text{ind}}$ are accessible in transport measurements. The energies of the excitations will not keep increasing but rather flatten out at $E = \Delta_{\text{ind}}$, as seen at the edges in Figure 2.1c-d. Secondly, the superconductor was considered as a bulk material and therefore poses no charging effect. In reality, the counterpart of the superconductor shown in Figure 2.1a is a short proximitized semiconductor section. Due to the small size and the inherent disorder, a finite charging energy is

often present and must be considered when interpreting the measurement results. For example, the tunnelling spectroscopy of the middle proximitized section may exhibit the same "eye-shaped" feature as shown in Figure 2.1c (Chapter 6, Supplementary S4). These realistic constrictions have been studied both theoretically and experimentally [24–27], and we refer readers to those publications for further details.

2.2 QD-S-QD: WEAK COUPLING REGIME

For local processes, the physical size of the superconductor is irrelevant and can, in principle, be arbitrarily large. However, the situation becomes intriguing, if the superconductor is confined to a width comparable to the coherence length ξ and sandwiched by two normal sections. Two extra, non-local processes then takes place: elastic Co-tunnelling (ECT) and crossed Andreev reflection (CAR). If one QD with large E_c is created on either of the normal section, the resulting device geometry is the so-called Cooper pair splitter (CPS) [28]. This is because now the two electrons, splitting from a Cooper pair, are forced to tunnel into opposite side as the double occupation in single dot is energetically unfavorable. We first discuss the experimental detection of the CAR and ECT under different conditions in such a device. Next, we introduce a control mechanism allowing us to flexibly adjust the strength of these processes, which enables us to construct a highly efficient CPS in Chapter 5, and towards realizing an artificial Kitaev chain in Chapter 6.

2.2.1 CAR AND ECT: EXPERIMENTAL DETECTION

A possible transport mechanism responsible for Cooper pair splitting is CAR, in which two electrons are simultaneously injected into the superconductor to form a Cooper pair. A competing non-local process is ECT, where an electron tunnels from one side to the other side via a virtual intermediate state. In previous studies, measuring these two virtual processes independently was challenging because local AR was insufficiently suppressed. This difficulties likely arose from the large bandwidth of the dot levels or a soft induced superconducting gap [19]. This has been largely improved in the device under study in this thesis, thanks to the advancement of material growth and nanofabrication [29]. Therefore, we will only take CAR and ECT into account in the following discussion, unless mentioned specifically.

We begin the investigation of the transport mechanism by examining an experimental configuration (Figure 2.2a) in which only CAR is allowed . The system consists of two leads, two dot levels in the normal section and an ABS in the superconductor. To conserve energy during this process, the electrochemical potential of the two dots must be equal and opposite relative to the Fermi level. The negative bias voltages are applied both to the left and right lead, such that the electrons only

flow from the lead to the grounded superconductor. Crucially, the bias voltages need to be the same,to suppress the ECT. They also cannot exceed the ABS energy, to suppress direct resonant tunnelling through the ABS to the superconductor.

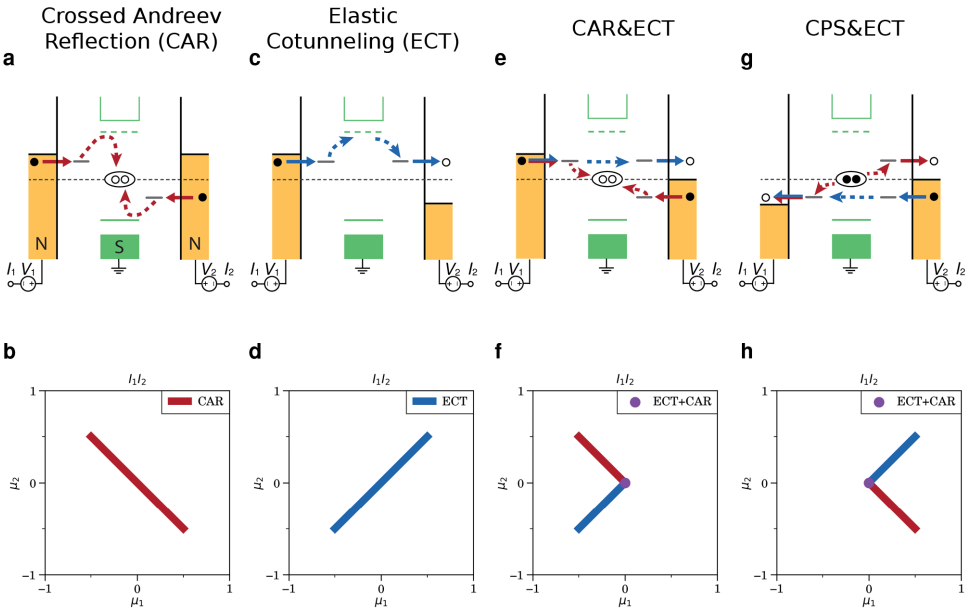

Figure 2.2: **Basics of CAR and ECT. (a)** In CAR, two electrons from the normal lead hop into the dots and then recombine as a Cooper pair in the hybrid section. Negative bias voltages of the same magnitude are applied to the left and right leads, while the middle hybrid section remains grounded. (**b**) Charge stability diagram (CSD) of the product of the measured currents $I_1 I_2$. CAR appears as finite currents observed along a negative slope. **(c)** In ECT, a single electron transfer from the one side to the other mediated by the ABS. Opposite but equal bias voltages are applied. **(d)** CSD shows ECT-only signal as with currents along a positive slope. **(e)** Both CAR and ECT are allowed when the right bias voltages is set to zero. When both dot levels are at zero under this condition, CAR and ECT coexist. **(f)** The resulting CSDs shows the combined features. Note the halved energy window of the left dot. **(g-h)** Similarly, a positive left bias and zero right bias allows Cooper pair splitting (CPS) and ECT, due to the reserved flow of electrons.

The CSD of the product of the expected current response $I_1 I_2$ is plotted in Figure 2.2b. This quantity is finite only if non-local transport occurs and here CAR is identified by a finite signal only along a negative slope. The energy window of both dot levels are equal and centered around the charge degeneracy points.

We continue to discuss the configuration where only allows ECT in Figure 2.2c. Dot levels now have to be aligned to transfer the same-energy electrons and the bias voltages of same magnitude but opposite polarity are required on either side to filter out CAR The resulting CSDs is shown in Figure 2.2d where $I_1 I_2$ are only finite along a positive slope, but spanning the same dot energy windows as CAR.

These two above cases illustrate the role of bias voltages in filtering the non-local processes. In fact, as far as the left and right bias voltages differ in magnitude, CAR and ECT will co-exist in the $\mu_1 - \mu_2$ parameter space. In Figure 2.2e, while the negative bias voltages are kept on the left side, the right side has zero bias voltages. The electron supplied from the left lead can now either fill the empty level on the right, via *ECT*, or recombine with another electron to form a Cooper pair, via *CAR*, depending only on the right dot levels. When both dot levels are at zero, both CAR and ECT are allowed. The resulting CSDs in Figure 2.2f thus contains two lines with opposite slopes, with the merging point enabling simultaneous CAR and ECT. The energy window of the left dot is also halved since it has to stay above the Fermi level to provide the electron. Figure 2.2g illustrates another similar situation, where positive biases are applied on the left and zero biases on the right. The right dot level still determines whether CAR or ECT can happen, but opposite to the situation in Figure 2.2e since the left side can only accept electrons. As a result, a point-symmetric CSD with respect to the Figure 2.2h is expected in Figure 2.2h. In summary, by adjusting the bias voltages and dot energy levels, one can selectively enable CAR or ECT within a finite parameter space. The intrinsic strength of these processes remains however constant, which is the topic of the next subsection.

2.2.2 Electrostatic tuning of CAR and ECT

Beyond selectively detecting the CAR and ECT , it is also crucial to control their amplitudes. This enables us to tune the system to the so called "sweet spot" in parameter space to study the topological superconductivity. Early studies faced challenges in achieving this control because the dot levels were coupled via the superconducting continuum. However, it was later proposed [30, 31] that this tunability of CAR and ECT amplitude can be realized when the two QDs are coupled via extended ABSs. The word "extended" refers to that the wavefunction of the ABSs has overlap with both QDs, thanks to the longer coherence length in the proximitized semiconductor. More specifically, this is achieved due to the change of the energy and charge character of the ABSs as function of an external gate voltages.

We focus on a system at zero magnetic field, which implies a two-fold spin degeneracy of a normal QD level. The finite field cases, together with the spin-orbit coupling will be addressed in the next section. The total Hamiltonian of the QD-ABS-QD system can be written as:

$$H = H_D + H_{\mathrm{ABS}} + H_T \tag{2.17}$$

where H_D describes the two normal QD, H_{ABS} the hybrid section hosting ABS and H_T the tunnelling term. The QD with a single level has the Hamiltonian:

$$H_{\mathrm{D}} = \mu_L d^\dagger_{L,\sigma_L} d_{L,\sigma_L} + \mu_R d^\dagger_{R,\sigma_R} d_{R,\sigma_R} \tag{2.18}$$

The ABS has been discussed before and we take it from Eq. 2.10:

$$H_{\mathrm{ABS}} = \mu_{\mathrm{ABS}} \sum_{\sigma=\uparrow,\downarrow} c_\sigma^\dagger c_\sigma + \Gamma_S (c_\uparrow^\dagger c_\downarrow^\dagger + c_\downarrow c_\uparrow) \tag{2.19}$$

note that $c^\dagger$ now represents the creation operator of a Bogoliubov quasi-particle in the hybrid part, distinguishing it from the $d^\dagger$ which is used in the QD.

Finally, the coupling term reads:

$$H_T = -\sum_{\sigma_L,\sigma_R} t_L d_{L,\sigma_L}^\dagger c_{\sigma_L} + t_R d_{R,\sigma_R}^\dagger c_{\sigma_R} + h.c. \tag{2.20}$$

where t_L and t_R are both non-zero in the presence of an extended ABS.

The system can be described with a combined quantum states $|L, M, R\rangle$, where:

$$\begin{aligned} L &\in \{\downarrow, \uparrow\}, && \text{left QD} \\ M &\in \{S_-, \downarrow, \uparrow\}, && \text{ABS} \\ R &\in \{\downarrow, \uparrow\}, && \text{right QD} \end{aligned} \tag{2.21}$$

The ABS in the hybrid part warrants a bit more discussion as it is crucial in affecting the transition rate of CAR and ECT processes. We recall that to transit between the singlet and the doublet states, the required excitation energy is either E_{0-} ($|S_-\rangle \to |\downarrow\rangle$) or E_{0+} ($|S_-\rangle \to |\uparrow\rangle$). At zero field these two energies become degenerate and are collectively denoted as E_0, which reads:

$$E_0 = \sqrt{\mu_M^2 + \Gamma_S^2} \tag{2.22}$$

if the charging energy in the hybrid section is low, i.e., $U_{\mathrm{ABS}} \to 0$. The BCS coherence factors u and v, as defined in Eq. 2.13 can then be simplified to:

$$u^2 = 1 - |v|^2 = \frac{1}{2}\left[1 + \frac{\mu_M}{\sqrt{\mu_M^2 + \Gamma_S^2}}\right] \tag{2.23}$$

These dependencies are plotted in the top panel of Figure 2.3a. We define the charge neutrality point as where $\mu_M = 0$. There, the ABS reaches its lowest energy and $u = v = \frac{1}{2}$. As the system move from the charge neutrality point, u becomes much larger than v on the negative side, while v dominates on the positive side. The ABS energy always get higher and eventually saturate at the induced gap Δ_{ind}.

During CAR and ECT, the middle ABS virtually occupies its excited state first, and then relaxes back to the ground state to reset the system for the next cycle.

The transition rate W of CAR and ECT can be calculated by using Fermi's golden rule with H_T as the perturbation term. The results are [30]:

$$\begin{aligned} W_{\mathrm{ECT}}^{\downarrow\downarrow} &= W_{\mathrm{ECT}}^{\uparrow\uparrow} = \alpha \left| \frac{u^2 - v^2}{E_0} \right|^2 \\ W_{\mathrm{ECT}}^{\downarrow\uparrow} &= W_{\mathrm{ECT}}^{\uparrow\downarrow} = 0 \\ W_{\mathrm{CAR}}^{\downarrow\downarrow} &= W_{\mathrm{CAR}}^{\uparrow\uparrow} = 0 \\ W_{\mathrm{CAR}}^{\downarrow\uparrow} &= W_{\mathrm{CAR}}^{\uparrow\downarrow} = \alpha \left| \frac{-2uv}{E_0} \right|^2 \end{aligned} \tag{2.24}$$

where α is a constant depending on the tunnel rate between the QD and ABS. The superscript marks the spin channel, namely the available spin species of the left (first index) and the right QD (second index).

We notice a few aspects in the equations before describing its trend: First, since these are second-order virtual processes, it makes sense that $|E_0|^2$ appears at the denominator The higher the excitation energy, the harder it becomes to virtually occupy the states to mediate the non-local transport and thus the lower transition rate. Secondly, the reason that u and v appear in the numerator is because the singlet ground state of the ABS $|S_-\rangle = u|0\rangle - v|\uparrow\downarrow\rangle$. To inject an electron to the ABS equals to apply a creation operator on it and this is only possible on the zero states. The electron component u is involved when the ABS absorb an electron, as the creation operator $c^\dagger$ acts only on the vacuum state $|0\rangle$. Similarly, removing an electron (or injecting a hole) involve the annihilation operator c, which acts only on the $|\uparrow\downarrow\rangle$, linking this step to the hole component v.

The allowed CAR and ECT rates are plotted as a function of μ_M in the bottom panel Figure 2.3a. Although the two processes are similar in transport cycles, they have distinctively different dependencies on the μ_M. At $\mu_M = 0$, ECT is vanishing while CAR reach its maximum rate, due to that $|uv|$ reaches its maximum and $|u^2 - v^2|$ equals to zero. Besides, the lowest E_0 at this point contributes to the maximal CAR rate, and also explains the fast decaying CAR when the system moves away from $\mu_M = 0$. On the other hand, away from the charge neutrality point, the ECT rate first increases due to the increase in the $|u^2 - v^2|$, before it decays again as the increase in E_0 become more dominant.

Now we try to develop an intuitive picture on the different dependencies of CAR and ECT. Essentially, this is due to the quantum interference between different paths. Two exemplary processes are presented schematically here where the detailed calculation can be found in Appendix. A. For a $\downarrow\uparrow$-CAR in Figure 2.3b, it starts with injecting an electron from one QD to excite the ABS to the doublet state, which later relax back to the singlet by absorbing another electron of *opposite* spin from another QD. This process can start either from the left dot (the upper),

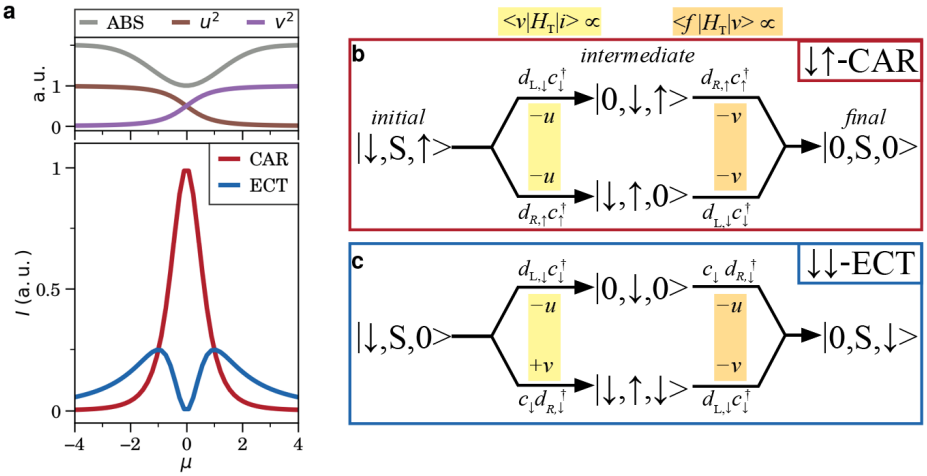

Figure 2.3: **CAR and ECT: the gate tunability and quantum interference. (a)** Top panel: the energy and the charge character (electron component u^2 and hole component v^2) of the ABS excitation as a function of the electrochemical potential μ. Bottom panel: the transition rate of the CAR and ECT mediated by the ABS. **(b)** The constructive interference of CAR. For each step, the relevant component in Hamiltonian H_T and the net contribution to the numerator in Eq 2.24 are labeled on the arrow. The top and bottom path each contributes to $(-uv)$. **(c)** The destructive interference of ECT. The top path contributes u^2 and the bottom path contributes $-v^2$. These terms are summed before taking the absolute value, leading to destructive interference between the two paths. For detailed calculation see Appendix A.

or the right dot (the lower), where the relevant term in H_T are labeled on the path arrows, respectively. For both pathways, the first step gives $-u$ and the second step gives $-v$. Since both paths contribute $+uv$ equally and are microscopically indistinguishable, constructive interference occurs and this leads to the $2 * (uv)/E_0^2$ transition rate in Eq. 2.24. Note that what matters here is the relative phase between the two pathways instead of the absolute phase.

The situation with ECT is more interesting,as shown in Figure 2.3c. The upper path is straightforward: the ABS receive an electron from the left QD, excited to the doublet state, and later relax back to the $|S\rangle$ by emitting the same electron to the other QD. Both steps here involve the filling and emptying of the vacuum-component $u|0\rangle$ in the singlet and therefore together contribute a u^2 in the numerator. In contrast, in the lower path the ABS receives first a hole from the otherwise empty right QD, thanks to $\uparrow\downarrow$-component in the singlet state. This creates a $\downarrow$-state in the right QD and an doublet-$\uparrow$ state in the ABS. By absorbing the $\downarrow$-electron from the left QD, the ABS relaxes to the singlet ground state. In either case the fermionic operators act on the $v|\uparrow\downarrow\rangle$ component, leading to a $-v^2$ component. Intuitively, this minus sign can be understood via the exchange statis-

tics of the electrons: In the upper path, the ↓-electron was created first in the ABS and then later in the right dot, whereas in the lower path, it was created in the opposite order, namely first the right dot and then the ABS. To reach the same final quantum state as the upper path, an additional exchange of the electron is required, which induces a global minus sign of the wavefunction. As a result, destructive interference occurs, which leads to the vanishing ECT amplitude at the charge neutrality point.

2.2.3 Triplet pairing in QD-S-QD

In common BCS superconductors, the ground state consists of singlet Cooper pairs with the form $|\uparrow\downarrow\rangle - |\downarrow\uparrow\rangle$. However, more exotic forms of superconductivity exist, such as triplet pairing, in which the Cooper pair condensate consists of two electrons with equal spin polarization. In a QD-S-QD system, this type of pairing enables the co-existence of CAR and ECT within the same spin configuration, which is crucial in constructing an artificial Kitaev chain, as discussed in the subsequent section. For now, we will briefly discuss how to realize such a pairing mechanism by introducing spin-orbit coupling in a hybrid system.

We start by a brief recap of the spin-orbit interaction, focusing on the Rashba type. Both because of its simplicity and also because it is expected to be the dominant SOC mechanism in the materials used in this thesis. The Rashba term is described by the Hamiltonian $H_{\mathrm{SO}} \propto (\vec{k} \times \vec{E}) \cdot \vec{\sigma}$ where $\vec{k}$ is the crystal momentum, $\vec{E}$ is the electric field and $\vec{\sigma}$ denotes the electron's spin. If we consider only an electric field along z-axis and momentum along x-axis (effectively reducing the system to 1D), the Hamiltonian simplifies to:

$$H_{\mathrm{SO}} = B_{\mathrm{SO}} \sigma_y \tag{2.25}$$

where $B_{\mathrm{SO}} = \alpha k_x$ with α the so-called Rashba parameter absorbing the effect of the electric field. The parameter α characterizes the SOC strength and is commonly used to compare different material systems. Importantly, the direction of B_{SO} is now fixed at a given electrostatic environment, while its magnitude depends on the momentum. When the applied external field B is orthogonal to the B_{SO}, there is a competition between the two spin-quantization axes. At $k = 0$ the B_{SO} is efficiently absent, meaning the electron spin aligns only with the external field. On the other hand, B_{SO} could become dominant at large momenta over the finite B and therefore determine the polarization axis. This interplay between Zeeman effect and SOC is the essential for engineering triplet pairing.

So far we have only considered spin conserving processes, namely equal-spin ECT and opposite-spin CAR. This holds as along as the external field aligns with the B_{SO}. However, when an external field (e.g. B_x) is applied perpendicular to B_{SO}, spin-flipping processes become allowed, specially opposite-spin ECT and

equal-spin CAR. In a classical picture, a spin-↑ electron (along B_x) will precess around B_{SO} and become a spin-↓ electron after traveling for a spin-orbit length $l_{SO} = \hbar^2/(m^*\alpha)$ [14]. In another word, SOC in the hybrid section introduces a finite spin flipping probability between the QDs, thereby enabling CAR couplings between two nominally equal-spin electrons.

We conclude the discussion on this topic by considering the detection technique of the triplet component. Instead of operating these QDs as charge filters, as shown in Figure 2.2, they can also be used as spin filters to acquire the spin information in the transport processes. Singlet Cooper pairs can only support opposite-spin CAR, and therefore currents are only finite when both dots have opposite spins. Same-spin CAR should be completely blocked, yielding no detectable currents. If triplet pairing was present, then that blockade would be lifted and thus ↑↑- and ↓↓ CAR currents should be visible. This observation thus should establish the triplet pairing between the two QDs and also the co-existence of CAR and ECT at the same parameter space.

2.3 QD-S-QD: strong coupling regime

So far, we have focused on the scenarios where the interactions between the QDs are week, namely smaller ECT and CAR transition rates. In another word, both t and Δ between the QDs are smaller than the broadening (thermal or tunnel), leading to a situation where excited states are always populated. Significantly larger t and Δ (i.e. stronger coupling) push excited states to higher energies. Under appropriate conditions, the system enters a topological phase and hosts a delocalized ground state at zero energy. Before discussing a finite system in details, it is useful to first examine the original Kitaev chain of infinite length.

2.3.1 The original Kitaev chain

The Kitaev chain is a one-dimensional model of spinless fermions and the simplest example which exhibit topological superconductivity. Such a chain with open boundary conditions is described by the following Hamiltonian [5]:

$$H = -\mu \sum_{j=1}^{N} d_j^\dagger d_j + \sum_{j=1}^{N-1} \left[-t(d_j^\dagger d_{j+1} + d_{j+1}^\dagger d_j) + \Delta(d_{j+1}^\dagger d_j^\dagger + d_j d_{j+1}) \right] \tag{2.26}$$

where μ is the on-site energy, t the hopping amplitude between the neighboring sites and Δ the superconducting pairing term. The Δ-term is unconventional, as it pairs up two nearest-neighbor electrons with the same spin. Note that both t and Δ are assumed to be real here.

Before solving the Hamiltonian under different conditions, we first introduce two new operators:

$$\gamma_{j,1} \equiv d_j^\dagger + d_j, \quad \gamma_{j,2} \equiv i(d_j^\dagger - d_j) \tag{2.27}$$

These operators are clearly hermitian, satisfying $\gamma_{j,1(2)} = \gamma_{j,1(2)}^\dagger$, and thus correspond to Majorana operators. In other words, creating such a quasiparticle is equivalent to annihilating one. As a result, the eigenstates corresponding to this operator must have zero energies. They further satisfy the relations:

$$\gamma_{j,1}, \gamma_{k,2} = 2\delta_{j,k}, \quad \gamma_{j,1}^2 = \gamma_{j,2}^2 = 1 \tag{2.28}$$

which follows from the fermion anti-commutation algebra. The original fermionic operators are expressed as:

$$d_j = \frac{1}{2}(\gamma_{j,1} + i\gamma_{j,2}), \quad d_j^\dagger = \frac{1}{2}(\gamma_{j,1} - i\gamma_{j,2}) \tag{2.29}$$

and thus rewrite the original Hamiltonian in Eq. 2.26 as:

$$H = \frac{-i\mu}{2}\sum_{j=1}^{N}\gamma_{j,1}\gamma_{j,2} + \frac{i}{2}\sum_{j=1}^{N-1}\left[(\Delta+t)\gamma_{j,2}\gamma_{j+1,1} + (\Delta-t)\gamma_{j,1}\gamma_{j+1,2}\right] \tag{2.30}$$

note that μ couples the two Majoranas at the same site, while $(\Delta - t)$ and $(\Delta + t)$ couples the Majoranas from neighboring sites.

We now consider two special conditions. If $t = \Delta = 0$ and $\mu \neq 0$, the system is trivial and behaves as a chain of standard fermions:

$$H_{trivial} = -\frac{i\mu}{2}\sum_{j=1}^{N}\gamma_{j,1}\gamma_{j,2} \tag{2.31}$$

However, if $t = \Delta \neq 0$ and $\mu = 0$, the Hamiltonian simplifies to:

$$H = it\sum_{j=1}^{N-1}\gamma_{j,2}\gamma_{j+1,1} \tag{2.32}$$

This is a non-trivial case. Here, instead of same-site coupling, the Majorana operators from neighboring sites are coupled across the entire chain. Notably, the two end Majorana $\gamma_{1,1}$ and $\gamma_{N,2}$ are missing from the Hamiltonian. If we now define a new set of fermionic operators $\hat{d}_j$ and $\hat{d}_j{}^\dagger$ using neighboring Majorana operators:

$$\hat{d}_j = \frac{1}{2}(\gamma_{j,2} + i\gamma_{j+1,1}), \quad \hat{d}_j{}^\dagger = \frac{1}{2}(\gamma_{j,2} - i\gamma_{j+1,1}) \tag{2.33}$$

and thus rewrite the Eq. 2.32 as:

$$H = 2t \sum_{j=1}^{N-1} (\hat{d}_j^{\dagger} \hat{d}_j - \frac{1}{2}) \tag{2.34}$$

It is clear that only $N-1$ fermions are included under this condition while the original Hamiltonian contains N fermions. The two missing Majoranas commute with the Hamiltonian $[H, \gamma_{1,1}] = [H, \gamma_{N,2}] = 0$ and thus corresponds to the zero energy ground states. The two end-Majorana together define one non-local fermion. These are the so-called Majorana zero modes (MZMs) or Majoranas bound states (MBSs), which we use interchangeably.

A few key points should be noted: first, this ground state degeneracy is unusual because the two states differ in fermion parity. This behavior contrasts sharply with conventional superconductors, where the ground state typically has even parity and the total parity remains conserved. Secondly, MZMs exist not only at the one spot ($t = \Delta \neq 0$ and $\mu = 0$), but in a broader area in the parameter space, distinguishing two different phases of the system. Specifically, MBSs will be present as long as $|\mu| < 2|t|$ and $\Delta \neq 0$ [32].

Although conceptually simple, realizing such a system is challenging due to the difficulties of simultaneously controlling the couplings t and Δ in a spinless chain. Fortunately, we have seen that the presence of the SOC enables the co-existence of both CAR and ECT. In the following section, we explore how to implement a Kitaev chain using quantum dots as fermionic sites, where t is provided with ECT and Δ with the CAR.

2.3.2 Spinless two-site Kitaev chain

A strongly coupled QD-S-QD system has been shown to host MZMs under certain conditions, as analyzed in detail in [33]. The Hamiltonian closely resembles Eq. 2.26 and reads:

$$H = \mu_1 d_1^{\dagger} d_1 + \mu_2 d_2^{\dagger} d_2 + t(d_1^{\dagger} d_2 + d_2^{\dagger} d_1) + \Delta(d_2^{\dagger} d_1^{\dagger} + d_1 d_2) \tag{2.35}$$

where t is the ECT amplitude and Δ is the CAR amplitude. Using the following Majorana operators:

$$\begin{aligned} d_1 &= \frac{1}{\sqrt{2}}(\gamma_1 + i\gamma_2), \quad d_1^{\dagger} = \frac{1}{\sqrt{2}}(\gamma_1 - i\gamma_2) \\ d_2 &= \frac{1}{\sqrt{2}}(\gamma_3 + i\gamma_4), \quad d_2^{\dagger} = \frac{1}{\sqrt{2}}(\gamma_3 - i\gamma_4) \end{aligned} \tag{2.36}$$

the Hamiltonian simplifies to:

$$H = i[\mu_1 \gamma_1 \gamma_2 + \mu_2 \gamma_3 \gamma_4 + (t - \Delta)\gamma_1 \gamma_4 + (-t - \Delta)\gamma_2 \gamma_3] + (\mu_1 + \mu_2) \tag{2.37}$$

A schematic representation of such a system is shown in Figure 2.4a. The Majoranas at the same site are coupled via μ, while those at neighboring sites are coupled via $(\Delta - t)$ and $(\Delta + t)$. In general, all Majoranas are connected such that no Majoranas remain isolated. However, γ_1 and γ_4 become unconnected if the system is at the "sweet spot", as illustrated in Figure 2.4b. This scenario mirrors the delocalized fermion in the original Kitaev chain.

Single-particle formulation

To further analyze the system, we solve its eigenstates and eigenenergies in the Nambu basis. Using the basis $\Psi = (d_1, d_2, d_1^\dagger, d_2^\dagger)^T$, the Hamiltonian can be expressed as a 4×4 matrix:

$$H_m = \begin{pmatrix} \mu_1 & t & 0 & \Delta \\ t & \mu_2 & -\Delta & 0 \\ 0 & -\Delta & -\mu_1 & -t \\ \Delta & 0 & -t & -\mu_2 \end{pmatrix} \tag{2.38}$$

We first consider the system at the sweet spot, $t = \Delta$ and $\mu_1 = \mu_2 = 0$. The solutions of the Bogoliubov-de Gennes equations $H_m\psi_i = E_i\psi_i$ are:

$$\begin{aligned} \psi_a &= \frac{1}{\sqrt{2}}\begin{pmatrix}1 & 0 & 1 & 0\end{pmatrix}^T, & E_a &= 0 \\ \psi_b &= \frac{i}{\sqrt{2}}\begin{pmatrix}0 & 1 & 0 & -1\end{pmatrix}^T, & E_b &= 0 \\ \psi_c &= \frac{1}{2}\begin{pmatrix}-1 & 1 & 1 & 1\end{pmatrix}^T, & E_c &= -2t \\ \psi_d &= \frac{1}{2}\begin{pmatrix}1 & 1 & -1 & 1\end{pmatrix}^T, & E_d &= 2t \end{aligned} \tag{2.39}$$

The zero-energy states ψ_a and ψ_b correspond to the MZMs, whereas ψ_c and ψ_d correspond to the lowest single-particle excitation. The second quantization operators are given by $\hat{\gamma}_i = \Psi \cdot \psi_i$:

$$\hat{\gamma}_a = \frac{1}{\sqrt{2}}(d_1 + d_1^\dagger) \quad \hat{\gamma}_b = \frac{i}{\sqrt{2}}(d_2 - d_2^\dagger) \tag{2.40}$$

We confirm these are the operators defined early in Eq. 2.36.

The next step is to investigate how the system responds when the parameters deviate from the sweet spot. By diagonalizing H_m, we obtain the general eigenvalues of the matrix

$$\lambda^2 = \mu_+^2 + \mu_-^2 + t^2 + \Delta^2 \pm 2\sqrt{(\mu_+^2 + \Delta^2)(\mu_-^2 + t^2)} \tag{2.41}$$

where $\mu_\pm = \mu_1 \pm \mu_2/2$. At $|t| = |\Delta|$, zero-energy solution exist as long as either $\mu_1 = 0$ or $\mu_2 = 0$. If only one dot level, say μ_1, is shifted from zero, the eigenstates of the

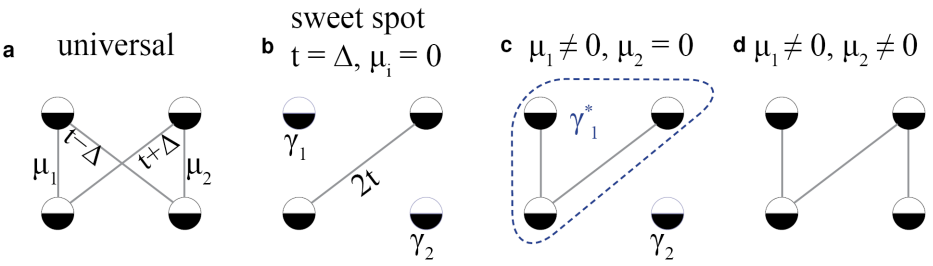

Figure 2.4: **Majoranas in a two-site Kitaev chain. (a)** In general, all four Majoranas are coupled. **(b)** At the sweet spot, only γ_2 and γ_3 are coupled with $2t$, leading to isolated Majorana modes γ_1 and γ_4 each on one site. **(c)** Detuning the μ_1 from zero fuses three Majorana together and has no effect on γ_4. **(d)** Detuning both μ_1 and μ_2 from zero however connects all Majoranas together and thus instantaneously destroys the zero-energy states.

lowest energies become:

$$\begin{aligned} \tilde{\psi}_a &= \frac{1}{2\sqrt{1+\delta^2}}\begin{pmatrix}1 & -\delta & 1 & -\delta\end{pmatrix}^T, & E_a &= 0 \\ \tilde{\psi}_b &= \frac{1}{\sqrt{2}}\begin{pmatrix}0 & 1 & 0 & -1\end{pmatrix}^T, & E_b &= 0 \end{aligned} \tag{2.42}$$

where $\delta = \mu_1/2t$. While $\tilde{\psi}_b$ is still completely localized on the right site, $\tilde{\psi}_a$ acquires a component proportional to δ. This is illustrated in Figure 2.4c. Due to a non-zero μ_1, the $\tilde{\psi}_a$ involves three Majoranas, leading to an extension of its wave function towards the right side.

The MZMs are however, not robust against the change of the chemical potential in both dot levels. To leading order, their energy $E_{a,b} \propto \mu_1\mu_2/2t$ [33]. Therefore, the zero energy modes are vulnerable to a quadratic, simultaneous change of the chemical potential. As shown in Figure 2.4d, non-local MZMs no longer exist in that situation.

The system is even more fragile when the $t = \Delta$ condition is violated. A small deviation results into $E_{a,b} = |(t-\Delta)|$, causing an immediate split from zero energies for the MZMs. Therefore, to maintain MZMs, μ_i must remain small, and t and Δ should be as close as possible.

Many-body formulation

Besides the single particle picture, the two-site chain can be analyzed in terms of its many-particle states. This approach provides a clearer distinction between states with different parities. Each dot level can either be empty ($|0\rangle$) or occupied ($|1\rangle$). Using the combined number basis $|\text{dot1}, \text{dot2}\rangle$,=($|00\rangle, |11\rangle, |10\rangle, |01\rangle$), the Hamiltonian

is given by:

$$H = \begin{pmatrix} 0 & \Delta & 0 & 0 \\ \Delta & \mu_1 + \mu_2 & 0 & 0 \\ 0 & 0 & \mu_1 & t \\ 0 & 0 & t & \mu_2 \end{pmatrix} \tag{2.43}$$

where the even states $|00\rangle$ and $|11\rangle$ are coupled via Δ and the odd states $|10\rangle$ and $|01\rangle$are coupled via t. Note that this matrix closely resembles the one in Eq. 2.11, where the spin-up/spin-down index of an orbital level is replaced by the charge number in the basis. The block-diagonal structure allows the even- and odd-parity manifolds to be treated separately, with eigenenergies:

$$E_{e,\pm} = \mu_+ \pm \sqrt{\Delta^2 + \mu_+^2} \quad E_{o,\pm} = \mu_+ \pm \sqrt{t^2 + \mu_-^2} \tag{2.44}$$

where we recall $\mu_\pm = (\mu_1 \pm \mu_2)/2$. The ground state of the QD-S-QD system is either even or odd, depending on whether $E_{e,-}$ or $E_{o,-}$ is lower. At the sweet spot, the solutions simplifies to :

$$\begin{aligned} |e,-\rangle &= -\frac{1}{\sqrt{2}}(|00\rangle - |11\rangle), & E_{e,-} &= -t \\ |o,-\rangle &= \frac{1}{\sqrt{2}}(|01\rangle - |10\rangle), & E_{o,-} &= -t \\ |e,+\rangle &= \frac{1}{\sqrt{2}}(|00\rangle + |11\rangle), & E_{e,+} &= t \\ |o,+\rangle &= \frac{1}{\sqrt{2}}(|01\rangle + |10\rangle), & E_{o,+} &= t \end{aligned} \tag{2.45}$$

The ground states contain both $|e,-\rangle$ and $|o,-\rangle$, which are degenerate in energies but differ in parity.

Parity plays a crucial role in this system. Applying the Majorana operators (as defined in 2.40) flips the parity of the ground state:

$$\begin{aligned} \hat{\gamma_a}\,|e_-\rangle &= \frac{1}{2}\left(+d_1 d_1^\dagger d_2^\dagger |00\rangle - d_1^\dagger |00\rangle\right) &&= \frac{1}{\sqrt{2}}\,|o_-\rangle \\ \hat{\gamma_b}\,|e_-\rangle &= \frac{i}{2}\left(-d_1^\dagger d_2 d_2^\dagger |00\rangle + d_2^\dagger |00\rangle\right) &&= \frac{i}{\sqrt{2}}\,|o_-\rangle \end{aligned} \tag{2.46}$$

Since the non-local fermion is defined as $f = \hat{\gamma_a} - i\hat{\gamma}_4/2$, its number operator is given by:

$$n_f = f^\dagger f = (1 - i\gamma_1\gamma_4)/2 \tag{2.47}$$

The eigenstates of the Hamiltonian are also eigenstates of n_f:

$$n_f\,|o_\pm\rangle = 0, \quad n_f\,|o_\pm\rangle = |o_\pm\rangle \tag{2.48}$$

Thus, the two-fold degeneracy corresponds to a system with either even or odd parity. This degeneracy allows for encoding quantum information using the parity of the Majorana bound states.

2.3.3 Spinful two-site Kitaev chain

A key assumption in the Kitaev chain model is that it consists of spinless fermions. Experimentally, this is achieved by applying a magnetic field such that the Zeeman energy in the QD greatly exceeds the effective couplings t and Δ. An relevant edge case to explore is the system's behavior at zero magnetic field. This condition is particular interesting because breaking the time-reversal symmetry is often necessary for a topological phase transition. In this subsection, we discuss how the large charging energy E_c (typically several meV) leads to a different ground-state degeneracy and the emergence of "spinful" MBSs. These states are protected similarly to the PMM in a spinless system. We further discuss how to distinguish the states arising under these two conditions.

the Hamiltonian a QD-S-QD system at zero magnetic field reads [34]:

$$H = \sum_{i,\sigma} \mu_i n_{i\sigma} + \sum_i U_i n_{i\uparrow} n_{i\downarrow} + t \sum_\sigma d^\dagger_{1\sigma} d_{2\sigma} + \Delta \sum_\sigma \eta_\sigma d^\dagger_{1\sigma} d^\dagger_{2\bar{\sigma}} + \text{H.c.} \tag{2.49}$$

where $n_{i\sigma} = d^\dagger_{i\sigma} d_{i\sigma}$ is the number operator on site i with spin σ, U_i the charging energy. $\eta_\sigma = +1$ (if $\sigma = \downarrow$) or -1 (if $\sigma = \uparrow$) and $\bar{\sigma} = -\sigma$ is used to ensure the singlet pairing. By tuning the relative strength of t and Δ, a sweet spot can always be found where the ground states become degenerate. An increasing U enhances the protection of the ground state degeneracy against local fluctuations in μ_L or μ_R [34]. In the limit $U \to \infty$, the full protection to local noise is achieved, similar to a spinless chain case. The Hamiltonian then simplifies to:

$$H = \sum_\sigma (\mu_1 n_\sigma + \mu_2 n_\sigma) + t \sum_\sigma d^\dagger_{1\sigma} d_{2\sigma} + \Delta \sum_\sigma \eta_\sigma d^\dagger_{1\sigma} d^\dagger_{2\bar{\sigma}} + \text{H.c.} \tag{2.50}$$

To examine the eigenstates, we express the Hamiltonian in this enlarged combined basis:

$$|00\rangle, |\uparrow\downarrow\rangle, |\downarrow\uparrow\rangle, |\downarrow\downarrow\rangle, |\uparrow\uparrow\rangle, |\downarrow 0\rangle, |0\downarrow\rangle, |\uparrow 0\rangle, |0\uparrow\rangle$$

where the first five states have even parity and the other have odd parity. This

resulting 9×9 matrix representation of the Hamiltonian is:

$$H=\begin{pmatrix}
0 & \Delta & -\Delta & & & & & & \\
\Delta & \mu_1+\mu_2 & 0 & & & & & & \\
-\Delta & 0 & \mu_1+\mu_2 & & & & & & \\
 & & & \mu_1+\mu_2 & 0 & & & & \\
 & & & 0 & \mu_1+\mu_2 & & & & \\
 & & & & & \mu_1 & t & & \\
 & & & & & t & \mu_2 & & \\
 & & & & & & t & \mu_1 & t \\
 & & & & & & & t & \mu_2
\end{pmatrix} \tag{2.51}$$

First, we consider the odd-parity 4×4 block in the the bottom-right corner. It contains two identical 2×2 matrices, each resembling the Hamiltonian of the spinless case. The eigenenergies are identical to the spinless case (Eq. 2.44)

$$E_{o,\pm}=\mu_+\pm\sqrt{t^2+\mu_-^2} \tag{2.52}$$

with $\mu_\pm=(\mu_1\pm\mu_2)/2$. These states have a multiplicity of 2 due to the Kramer degeneracy.

The even sector can also be treated using two separate matrices:

$$H_{e,1}=\begin{pmatrix}0&\Delta&-\Delta\\ \Delta&\mu_1+\mu_2&0\\ -\Delta&0&\mu_1+\mu_2\end{pmatrix}\qquad H_{e,2}=\begin{pmatrix}\mu_1+\mu_2&0\\0&\mu_1+\mu_2\end{pmatrix} \tag{2.53}$$

The eigenvalues of the two matrices are

$$E_{e,1}=\begin{cases}E^t_{e,1}=2\mu_+,\\ E^s_{e,1,\pm}=\mu_+\pm\sqrt{2\Delta^2+\mu_+^2},\end{cases}\qquad E^t_{e,2}=2\mu_+, \tag{2.54}$$

where the superscript t denotes triplet states and s denotes singlet states. Note that $E^s_{e,1,\pm}$ are almost identical to the ones in Eq. 2.44, except for the presence of $2\Delta^2$ instead of Δ^2 under the square root. The condition for degenerate ground states, obtained by setting $E_{o,-}=E^s_{e,1,-}$, is now:

$$t^2-2\Delta^2=\mu_1\mu_2 \tag{2.55}$$

Thus, the new "sweet spot" condition becomes:

$$t=\sqrt{2}\Delta,\mu_1=\mu_2=0 \tag{2.56}$$

The ground state degeneracy now consist of two odd states and one even state, all with energy $E_{gs} = -t$:

$$\begin{aligned} |GS,\downarrow\rangle &= \frac{1}{\sqrt{2}}(|0\downarrow\rangle - |\downarrow 0\rangle) \\ |GS,\uparrow\rangle &= \frac{1}{\sqrt{2}}(|\uparrow 0\rangle - |0\uparrow\rangle) \\ |GS,S\rangle &= -\left[\frac{1}{\sqrt{2}}|00\rangle - \frac{1}{2}(|\uparrow\downarrow\rangle - |\downarrow\uparrow\rangle)\right] \end{aligned} \tag{2.57}$$

These states are analogous to those obtained in the spinless case (Eq. 2.45). Specifically, $|GS,\downarrow\rangle$ and $|GS,\uparrow\rangle$ differ from $|o,-\rangle$ by introduction of the spin indices. The global minus sign between $|GS,\downarrow\rangle$ and $|GS,\uparrow\rangle$ is a consequence of the time-reversal symmetry. $|GS,S\rangle$ are almost identical to $|E,-\rangle$, except that the triplet term is replaced by a singlet term. Transitions between these ground states give rise to the zero energy excitations.

To fully understand the energy spectrum, we now examine the excited states. The first excited state manifold, denoted as $|ES1\rangle$, consists of triplet states, which have even parity and an energy $E_{es1} = 0$:

$$\begin{aligned} |ES1,\downarrow\rangle &= -|\downarrow\downarrow\rangle \\ |ES1,\uparrow\rangle &= +|\uparrow\uparrow\rangle \\ |ES1,0\rangle &= -\frac{1}{\sqrt{2}}(|\downarrow\uparrow\rangle + |\uparrow\downarrow\rangle) \end{aligned} \tag{2.58}$$

The second excited states manifold is again triply degenerate with an energy $E_{es2} = +t$

$$\begin{aligned} |ES2,\downarrow\rangle &= -\frac{1}{\sqrt{2}}(|0\downarrow\rangle + |\downarrow 0\rangle) \\ |ES2,\uparrow\rangle &= +\frac{1}{\sqrt{2}}(|\uparrow 0\rangle + |0\uparrow\rangle) \\ |ES2,S\rangle &= -\left[\frac{1}{\sqrt{2}}|00\rangle + \frac{1}{2}(|\uparrow\downarrow\rangle - |\downarrow\uparrow\rangle)\right] \end{aligned} \tag{2.59}$$

In summary, the lowest three manifolds all feature three-fold degeneracy, as shown in Figure 2.5f. The degeneracy of each manifold is maintained upon varying one local on-site energy, demonstrating the protection of strong zero modes to this perturbation [34]. Both $|GS\rangle$ and $|ES2\rangle$ contain two odd and one even parity states. In contrast, $|ES1\rangle$ only consists of three triplet states of even parity. The presence of $|ES1\rangle$ leads to an extra transition in the system and asymmetry in the energy spectrum, which we will explained in the following subsection.

Spinless vs spinful PMM

This part aims to compare the energy spectrum of a spinless and a spinful two-site chain, highlighting both the similarities and difference.

We start with a spinless chain shown in Figure 2.5a, $t_{\downarrow\downarrow}$ and $\Delta_{\downarrow\downarrow}$ are coupling the dot levels. The available states (grouped by their parities) and the transitions are shown in Figure 2.5b. Since transport occurs via single-fermion transfers, transport can only happen between the odd and even parity states, but not within the same parity manifold. As a result, there are zero-energy excitation $E_0 = 0$ (between degenerate ground states) and first excitation E_1 (between ground states and excited states). Importantly, E_1 can be driven by either accepting an electron (e.g. from $|00\rangle \Rightarrow |0\downarrow\rangle$) or a hole (from $-|\downarrow\downarrow\rangle \Rightarrow |\downarrow 0\rangle$). This results in a mirroring in the excitation spectrum around $E = 0$.

To complete our discussion of the spinless case, we now examine how to system respond to the variation of μ_1, which provides insight into the robustness of the MZMs. From Eq. 2.44, the energy levels are:

$$E_{\pm} = \frac{1}{2}\left(\mu_1 \pm \sqrt{4t^2 + \mu_1^2}\right) \tag{2.60}$$

The evolutions of the energy levels and the excitation energies are plotted in Figure 2.5c and Figure 2.5d, respectively. First, we notice that the two-fold degeneracy is preserved at all values μ_1 , giving rise to persisting zero energy states over the whole range (blue arrow and line). E_1 (the green arrow) reaches its minimum at $mu_1 = 0$ and increase symmetrically as mu_1 deviate from zero. Indeed, in Figure 2.5d, E_1 has an minimum of $2t$ and is mirrored vertically over $E = 0$, as the transitions can be driven with either electrons or holes.

Now we focus on a spinful chain, where only spin conserving processes are allowed due to the time-reversal symmetry. Consequently, equal-ECT and opposite-spin CAR are non-locally coupling the two dots (Figure 2.5e.) The three lowest eigenstates at the sweet spot are shown in Figure 2.5f, along with the allowed excitations. While the E_0 (blue) and E_2 (green) excitations are reminiscent of those in Figure 2.5b, the first excited states (triplet) and the E_1 excitations (pink-orange) are unique for a spinful system. Note that it is only possible to drive the E_1 excitations via electron (but not hole), leading to an asymmetric excitation spectrum.

Plotting the eigenenergies of the system in Figure 2.5g as a function μ_1 confirms that the ground and second excited states match those in Figure 2.5c. This is expected, as the two groups of states in the spinful case differ from those in the spinless case in two ways: the triplet component is replaced with the singlet one (due to the nature of the coupling), and the number of odd states is doubled(due to the Kramer degeneracy). However, the E_1 excitation introduces an additional line

and is only present in positive energies, because it can only be driven by adding an electron. Furthermore, E_1 decreases monotonically in energy and eventually approaches zero as μ_1 become much negative. Both features have been successfully identified experimentally by performing tunneling spectroscopy to distinguish between spinless and spinful Majorana modes in Chapter 6 .

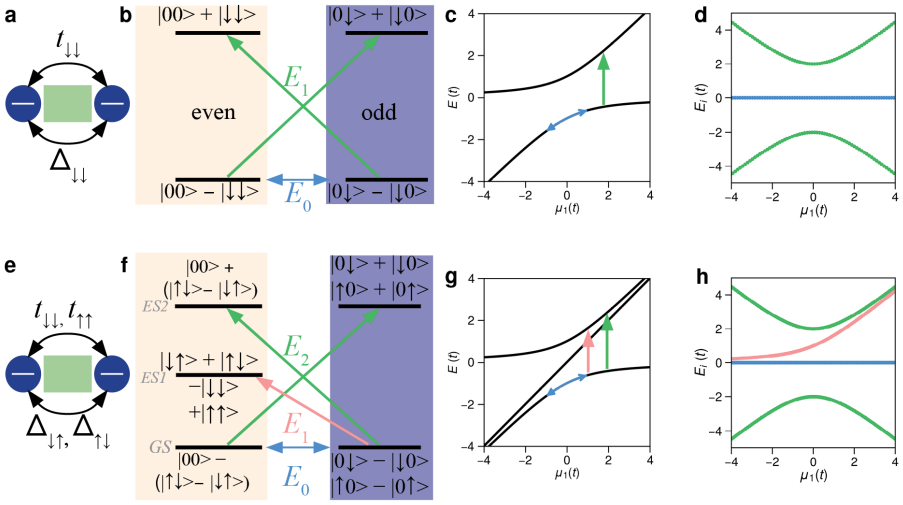

Figure 2.5: **Spinless and spinful PMM. (a)** A spinless two-site chain. **(b)** The eigenstates at the sweet spot. The possible excitations are labeled with arrows. The eigenenergies **(c)** and the excitation energies **(d)** are plotted as a function of μ_1, which is the only variable deviating from the sweet spot condition. The two degenerate ground states give rise to the zero energy excitation $E_0 = 0$. The lowest excitation E_1 is symmetric around $\mu_1 = 0$. **(e)** A spinful two-site chain. **(f)**The eigenstates at the sweet spot and the transitions. Note that E_1 is only possible by adding an electron to the odd ground states. The eigenenergies **(g)** and the excitation energies **(h)** are plotted as a function of μ_1. A decreasing μ_1 leads to a smaller and eventually diminishing E_1. Furthermore, E_1 is only possible at the positive energies because only electron transfer is accepted.

In conclusion, we discussed how to engineer the minimal two-site Kitaev chain based on coupled quantum dots. Unlike the topological states in a p-wave superconductors, these poor-man Majorana modes lack strong protection, as small deviations in the $t = \Delta$ break their quadratic protection against chemical potential fluctuations. The protection can be enhanced by scaling up the system and there are two possible directions. One is to literally extend the chain by adding more QDs and eventually emulate the original Kitaev chain. It was shown that a chain consisting of only five sites is enough to show the some robustness against the disorder [35]. Despite of its conceptual simplicity, this approach requires great

effort in nanofabrication due to the increased number of control gates. The other solution is to engineer the Hamiltonian with the conventional materials, such as the semiconductor nanowires and the *s*-wave superconductor. Essentially, the atomic sites in the Kitaev chain are approximated by the unit cells in the crystal structure. Within this thesis, this approach is explored and briefly summarized at the beginning of Chapter 4.

3

Fabrication Methods

From the heights of these pyramids, forty centuries look down on us.

Napoleon Bonaparte

3.1 The 2DEG growth and materials

It has become clear from the theory chapter that studying topological superconductivity requires a few ingredients: a semiconductor with high mobility, strong spin-orbit coupling, and excellent proximity to a superconductor. On the other hand, studying non-Abelian statistics through fusion or braiding of MBSs often involves complex device architectures [36–38], highlighting the need for a flexible and scalable platform. A semiconductor two-dimensional electron gas (2DEG) coupled to a superconductor is an ideal candidate for this purpose. The top-down fabrication process brings great flexibility in constructing the desired device architectures, which enables the creation of devices shown in Figure 3.1f and Figure 3.6k with the additional tunnel contacts probing the bulk of the system. This presents minimal challenges in a 2DEG system, but could be challenging to realize in other platform, for example the hybrid nanowires. It is thus crucial to develop a two-dimensional (2D) platform with excellent material properties for advanced studies.

Over the past few decades, Molecular beam epitaxy (MBE) has become a well-established method for producing high quality 2DEGs. This technique utilizes an electron beam to hit the effusion cells, causing atoms to be ejected and deposited on a substrate in an ultra-high vacuum chamber. It enables the growth of single-crystal layers with precise control over layer thickness and chemical composition. Bandgap engineering, which involves sandwiching the semiconductor of interest between two other layers with larger band gaps, is employed to confine the electrons in a 2D plane. Potential lattice mismatches between adjacent layers can be mitigated using the relaxation layer, which consists of a series of layers with gradually varying chemical compositions.

Besides carefully designed MBE growth, it is also crucial to select appropriate semiconductor and superconductor materials. The hybrid 2DEG used throughout this thesis is InSbAs, a ternary III-V semiconductor, with in-situ grown epitaxial Al. We have previously demonstrated this material to have high mobility, strong SOC, and excellent proximity to the superconductor [29]. Characterization in Hall bar devices reveals a peak mobility between 20 000 cm^2/Vs and 28 000 cm^2/Vs. The band structure calculation shows that the Rashba parameter α strongly depends on the As-concentration [39, 40]. By studying weak anti-localization, the extracted α lies in between 100 meVÅ and 400 meVÅ, signifying a strong spin-orbit interaction, even larger than the values in the binary constituents (InSb and InAs). We have also demonstrated the excellent interface between the superconductor and the semiconductor, where we have observed an induced hard superconducting gap of 220 μeV in tunneling spectroscopy. Note that this is a surface 2DEG, meaning there is no top semiconductor barrier above the active 2DEG regions to enhance the proximity effect. It has been reported that by adding 40 nmAlInSb top barriers to the 2DEG, without in-situ grown Al, a peak mobility up to 240 000 cm^2/Vs and

a Rashba parameter of about 300 meVÅ were observed [41]. Despite the improvements in semiconductor properties, the effect of induced superconductivity remains unexplored in buried 2DEGs. In summary, the established material properties of this surface hybrid 2DEG make it highly promising for the further investigation of topological superconductivity across various types of devices. The Figure 3.1a-c

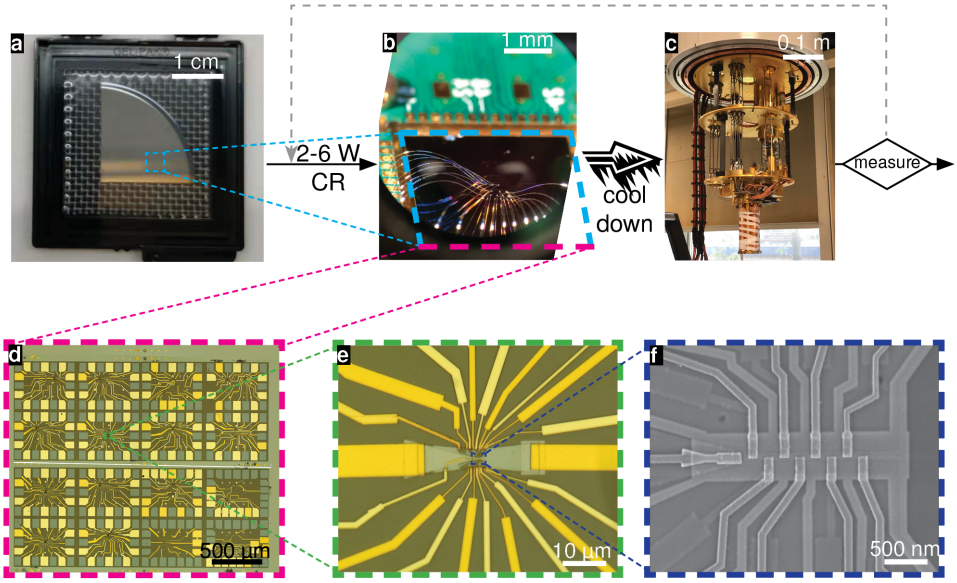

Figure 3.1: **A glimpse on the journey: a sample at different times and in different length scales.** (**a**) The fabrication process starts with a MBE-grown InSbAs-Al wafer of quarter-2" size. Dicing such a wafer produces approximately 10 to 15 chips, each measuring 5 mm x 5 mm. **(b)**A finished chip is glued onto the cold finger and wire-bonded **(c)** This unit is subsequently loaded into a (dilution) refrigerator for characterization and measurement. If needed, the fabrication process is repeated to create new devices. **(d)** A low-magnification optical microscope image of the chip shows 16 devices, each surrounded by up to 20 large bond pads for wire bonding. **(e)** A close-up of a single device shows a semiconductor mesa (central dark green region), contacted by two ohmic contacts (golden) on the left and right. The remaining golden leads are gate electrodes. **(f)** A SEM ultimately reveals a details view of the nanostructures at the center, which corresponds to the device studied in Chapter 4.

offers a glimpse of our workflow, from receiving a fresh wafer to performing measurement. The layout and medium to large structures on a chip can be seen under an optical microscope, as shown in Figure 3.1d and e. These pictures are captured after nearly every fabrication step to to monitor outcomes. To resolve the feature size at the order of a few hundreds nanometers, Scanning Electron Microscope (SEM) is used to produce images such as the one shown in Figure 3.1f. Recently, concerns have been raised about the potential detrimental effect of electron beams

on the device transport behavior. As a precaution, SEM images are primarily taken of the sister devices, which are the closest replica on the chip to the actual devices being measured.

The remaining sections of this chapter focus on the "2-6 weeks" period in the cleanroom. Key fabrication processes are covered, starting from simple spectroscopy devices highlighting the process optimization, and progressing to the fabrication of three-site Kitaev chain devices with more than 15 fabrication steps. Important details regarding device design and associated challenges are also discussed.

3.2 Device fabrication: the old “simple" days

The device shown in Figure 3.1f is naturally not the first one I made to study the topological superconductivity. In 2019, the InSbAs-Al hybrid 2DEG was relatively new to us, and we started making gate-defined hybrid wire with one tunnel junction at the end. Such a geometry has been studied in the InAs/Al hybrid 2DEG [42], where the emergence of zero-bias conductance peak was associated with Majorana zero modes. Despite the simple device geometry, establishing a fabrication flow and the ability to repeatedly make functional devices was crucial. The section below underscores the fabrication of this simple spectroscopy device with a single gate layer.

To start with, Figure 3.2a shows a stack of InSbAs coupled to in-situ grown Al. The ternary 2DEG with 14% As concentration is used throughout this thesis due to its stronger SOC and extended gate tunability [29]. The two monolayers of InAs are added to prevent the diffusion of Al into the 2DEG through an exchange reaction, which can lead to a degradation of the interface [43]. Since the exchange reaction is thermally activated, we incorporated a few procedures to keep the process temperatures as low as possible, which include the vacuum oven baking (usually 2 hrs) and the low-temperature Atomic Layer Deposition (ALD). The extra long baking time particularly slows down the optimization process, where multiple turnaround cycles are required.

First, the wafer needs to be diced to small pieces of 5 mm x 5 mm to fit within the circuit board. In the preparation phase, coarse markers were deposited across the wafer using standard nanofabrication techniques, including PMMA spin-coating, E-beam lithography (EBL), Ti/Au metal evaporation, and liftoff. These markers serve as alignment references for the subsequent lithography steps and also as guidelines during the dicing. Just prior to the dicing, we spin-coat the photo-resist S1813 as the dicing resist to prevent the re-deposition of residues onto the surface. After stripping the photoresist, we spin-coat PMMA on each small chip to stop further oxidation and store them in the desiccator.

With a chip shown in Figure 3.2b, the next step is to create multiple isolated

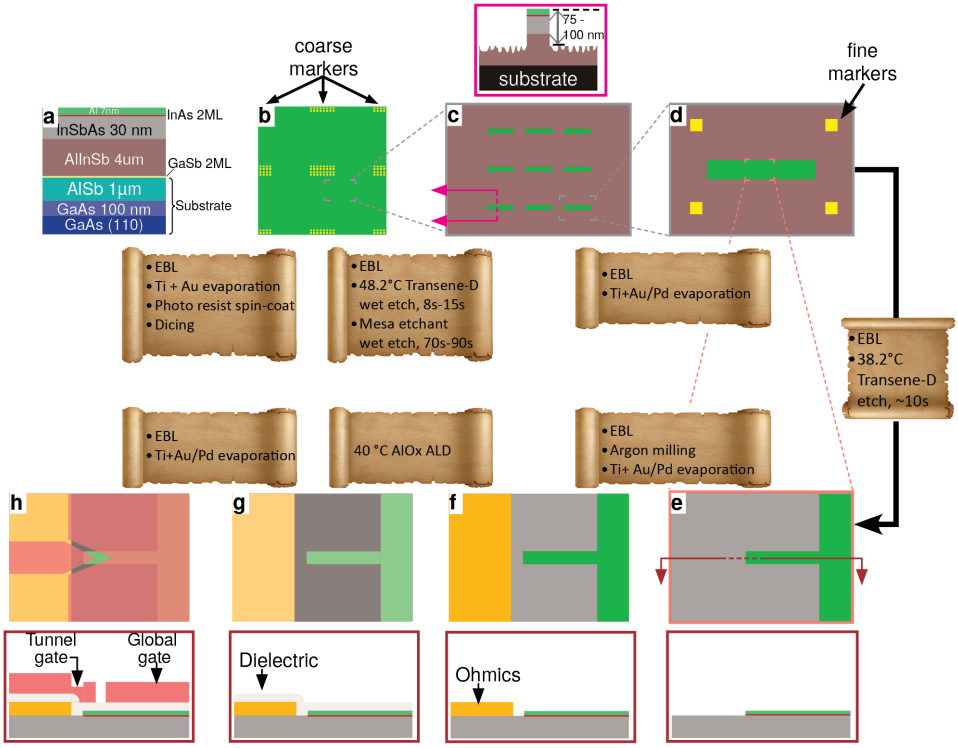

Figure 3.2: **The fabrication steps for a simple spectroscopy device. (a)** The wafer stack of the InSbAs/Al heterostructure. The two monolayers (ML) of InAs are placed to prevent the diffusion between the Al and the 2DEG. The first step is to dice the wafer into small pieces, by following the steps within the box in between the two stages of the sample. **(b)** Top view of a diced 5 mm x 5 mm chip with the alignment markers. Next, the aluminium and III-V materials in certain areas are removed by Transene D and mesa cocktail etchant, respectively, creating multiple isolated hybrid islands (called "mesa") on the sample. **(c)** An area containing nine mesas. A cross-sectional view shows that the active InSbAs in between two mesas are fully removed. **(d)** A mesa surrounded by fine alignment markers, for improved alignment accuracy between different EBL steps. **(e)** The middle area of a mesa with a thin Al strip. A horizontal cut along the strip is shown for this and the following steps. **(f)** The sample with one side normal contacts. **(g)** The sample with a global 40 deg ALD of AlOx dielectric. The low-temperature process prevents the intermixing between Al and Sb. **(h)** The sample with the tunnel gate and the global gate electrode.

"mesas". We use undeveloped PMMA as the mask, and perform two wet etch steps: A 8 s to 15 s etch in 48.2 °C Transene aluminium etchant Type D (referred as "Transene D") to remove the Al, followed by a 70 s to 90 s etch in a room-temperature III-V etchant mixture. This removes the 2DEG and leads to an etch depth from 70 nm to 100 nm (Figure 3.2c). The mixer is made of 560 mL H_2O, 5 mL H_2O_2, 4 mL 85% H_3PO_4, and then 9.6 g citric acid.

Zooming in on one single mesa surrounded by the extra fine markers Figure 3.2d, the next step is to define the fine structure of the aluminium. This is achieved using a 38.2 °C Transene D etch for about 10 s. The temperature is chosen to balance controllable level of etch time and mask delamination risk. Similarly, etch tie is tuned to avoid both the incomplete etching and the over-etch. Given the significance of this etch process, it is discussed in more detail in Figure 3.3.

Once we have succeeded in defining the fine structures, we deposit normal contacts adjacent to them. They consist of 5 nm Ti (sticking layer) and another 20 nm Au or Pd, with Pd preferred due to its ability to form a continuous film even at thin layers). Before metal deposition, a gentle in-situ Argon milling step is performed in the evaporator's load-lock, to remove the potential oxide on the surface and thus increase the contact transparency. Alternatively, aluminium can also be used as ohmic contacts. The comparison between superconducting and normal metal contacts is discussed in Figure 3.4. Next, the sample is covered with a global AlOx dielectric layer, grown at 40 °C using ALD, as shown by the translucent layer in Figure 3.2g. This process is chosen due to the thermal budget for processing this hybrid material. Tunneling spectroscopy measurements using this dielectric layer yield much cleaner results compared to previous approaches using sputtered SiNx [44]. The final stage is another Ti+Au/Pd evaporation to create the gate electrodes (Figure 3.2h). The global gate depletes the 2DEG surrounding the Al strip, thereby defining the 1D hybrid wire. The pointy tunnel gate controls the transparency of the tunnel barrier, which is the semiconductor region between the wire and the contacts. This enables tunnel spectroscopy at the wire end, allowing us to study the density of states as a function of various parameters, such as gate voltages or the external magnetic field.

3.2.1 Selective aluminium etch

As mentioned in the previous section, the most crucial step in fabrication is the selective fine Al etch. Without a well-defined nanostructure, such as a strip with sharp edges and corners, it is challenging to fabricate the desired devices, as well as to interpret the measurement results. However, the available etch methods are limited in this context. Dry etching usually delivers a precise result, but no known etchant gases selectively remove Al while preserving III-V semiconductors. At the same time, it is extremely difficult to achieve accurate time control over the etch depth, due to the weak signal in the endpoint detection method as a result of the thin and small Al film size There, we opt for wet etching using undeveloped PMMA as the etch mask and Transene D as the etchant. Transene D was chosen due to it is reasonably compatibility with III-V materials. However, it is important to note that its etch rate was typically calibrated for removing Al layers much thicker than the 7 nm- film used in our materials. One practical limitation is that the first

few seconds of etching process are likely spent removing the native surface oxide before the etch of Al itself. Given that the total working etch time is around 10 s, this process is extremely time-sensitive.

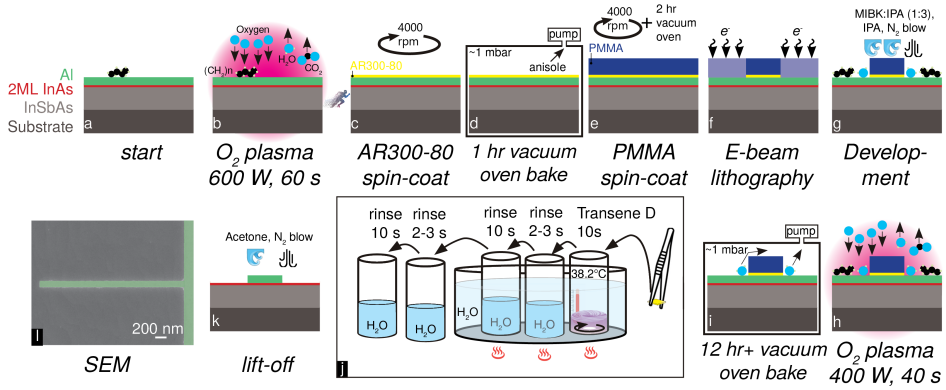

Figure 3.3: **Trasene D wet etch in details. (a)** Cross-sectional view of a sample at stage Figure 3.2d. The organic residues originates from incomplete removal of the e-beam resist in the previous step. **(b)** A strong oxygen plasma session removes these residues. **c** spin-coating of AR300-80 adhesion promoter to improve adhesion between the sample surface and PMMA. **(d)** 1 hr vacuum oven baking for AR300-80. **(e)** Spin-coating of PMMA followed by a 2 hr vacuum over bake. **(f)** E-beam exposure where the unexposed PMMA serves as the etching mask. **(g)** The exposed PMMA was dissolved using an MIBK/IPA mix. **(h)**. Another gentle oxygen plasma step post-development to remove the organic contamination. **(i)** A 12 hr+ vacuum oven post-bake to pump away the surface-adsorbed water and potentially enhance resist adhesion. **(j)** Transene D wet etch setup with one Transene D and two DI water beakers kept in the hot water bath. Two more beakers with room temperature DI water are there for further rinsing. **(k)** Lift-off of the remaining resist with cold acetone. **(j)** A SEM of an etched structure.

Let us now dive into the details of Transene D etch in Figure 3.3. The first step is to surface cleaning using oxygen plasma to remove organic residues from previous lithography steps. Once the sample is taken out of the oven, we immediately spin-coat the sample with two droplets of AR300-80 adhesion promoter to minimize re-deposition of water or dust particles. The sample then undergoes a 1 hr-bake in the vacuum oven to remove the solvent and enhance the resist adhesion. Following this treatment, PMMA is spin-coated and baked for 2 hr in preparation for E-beam lithography. During lithography, the electron beams break chemical bonds within the PMMA polymer matrix, rendering the exposed areas soluble during development. The development process consists of a 50 s dip in an MIBK/IPA (1:3) solution, followed by an IPA rinse and nitrogen blow-drying. This results in the desired patterning, where the middle section of Figure 3.3g remains covered with resist.

After development, a mild oxygen plasma step is used to remove any residual

organics, followed by a 12 hr+ vacuum oven post-bake. This ensures complete desorption of water from the surface. The sample is taken out from the oven just a few minutes before immersion in Transene D to minimize re-adsorption of contaminants.

The wet etch setup is sketched in Figure 3.3j, where we place 125 mL of Transene D and 250 mL of water (2x) in beakers in a water bath. A thermometer and magnetic stirrer are positioned in the Transene D beaker, where the temperature is regulated by a PID controller. The four water rinses ensure an immediate and complete stop of etching once the sample left the Transene D. The entire process is performed using beakers of specific dimensions and carefully maintained liquid levels to improve reproducibility.

Once the etch is complete, lift-off is performed using cold acetone and the same is inspected under an optical microscope and ultimately SEM.

At this point, it should be clear why this process is slow, especially when the optimization of the exact etch time is required. The best etch time was found to vary slightly between wafers due to tiny differences in the Al growth and the in-situ oxidation process. Still, with a good sufficient amount of time in the clean room– and a bit of luck– a well-defined etch result like the one shown in Figure 3.3l can be achieved. We will revisit this topic in section 3.4 when we review the challenges and the recent development in this process.

3.2.2 Transport: normal vs superconducting contacts

Instead of the normal metal, the in-situ grown superconducting Al also works as a contact. Previous studies on InAs/Al hybrid 2DEG devices have demonstrated this approach, reporting a hard superconducting gap and ballistic transport [45]. One obvious advantage is that it eliminates one lithography step from the process, leading to a cleaner surface. Here we compare normal contacts and superconducting contacts in our hybrid InSbAs/Al 2DEG devices via the tunnelling spectra to find the most suitable option for our experiments.

We add a few remarks on top of the general fabrication procedures outlined in Figure 3.2. To make normal metal contact, we remove the aluminium that near the end of the Al strip (Figure 3.4a) to avoid the possible proximity effect. In contrast, superconducting contacts are created by defining a gap of about 100 nm between the Al strip and plane via Al etching (Figure 3.4e). The fabrication for both types of devices is completed following the deposition of ALD AlOx and the gate electrodes in Figure 3.4b and Figure 3.4f.

Both devices are measured in the dilution refrigerator to probe the local DOS at wire end. The transport process for a N-S junction is illustrated in Figure 3.4c. The applied bias voltages on the contact change its chemical potential and the applied tunnel gate voltages create a tunnel barrier. Figure 3.4d shows the measured

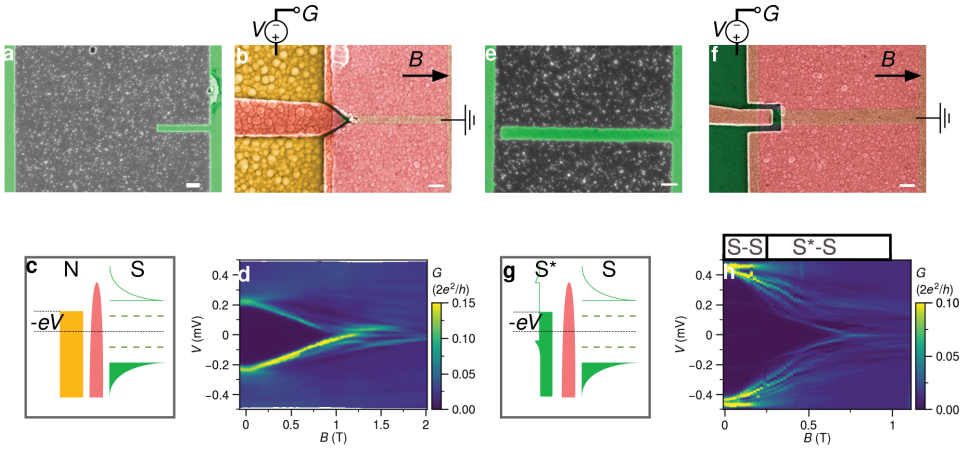

Figure 3.4: **Transport measurements of the spectroscopy device.** SEM images of the N-S device after Al etch **(a)** and after the gate deposition **(b)**. **(c)** Energy diagram for the transport at a finite field. The coherence peaks and the sub-gap states (dark green) are resolved in the measurement by the finite tunnelling conductance. **(d)** A typical field evolution of the measured conductance spectrum. With an increasing magnetic field, the subgap states get lower in energy and eventually reach zero bias. SEM image of the S-S device after Al etch **(e)** and after the gate deposition **(f)**. The large Al plane is now much closer to the Al strip and works as a contact. **(g)** Energy diagram for transport at a finite field. The Al plane has a roughly constant DOS over the whole range, thus making it a "normal" contact. **(h)** A field evolution of the measured conductance spectrum All scale bars here are 200 nm.

tunnelling spectra where we observe a hard superconducting gap of 0.22 meV at zero field. With increasing magnetic field, the lowest subgap states shift towards zero bias and persist for more than 0.7 T.

For the S-S device, the induced superconductivity in the Al plane is quenched at lower magnetic field compared to the strip. In that situation, as shown in Figure 3.4g, the DOS in the Al plane remains roughly constant over the relevant bias ranges, making it effectively a "normal" probe. Figure 3.4h shows that the gap at zero field is now (0.44 meV), twice that of the N-S device. Signals appearing within gap arise from supercurrent and multiple Andreev reflections (MARs). The gap quickly collapses to 0.22 meV when the field reaches around 0.26 T, marking the required field to lift the hard superconducting gap of the Al plane. With an increasing magnetic field, subgap states gradually reach zero energies.

In conclusion, both the normal and the in-situ grown Al function as good contacts and enable reasonable tunnelling spectroscopy results. However, superconducting contacts pose a few caveats: (i) the fabrication is more difficult to achieve due to the narrow gap required in wet etch process. (ii) MARs-related signals lead to a denser subgap spectra, and obscure the identification of the subgap states stemming from the hybrid wire, especially in the open regimes Thus, we only implement normal metal contacts in the subsequent fabrications.

3.3 Device fabrication: the new complex times

3.3.1 Fabrication of a two-site Kitaev chain

The transport results on one wire end are difficult to reproduce inconclusive regarding existence of the MBS [46]. To advance the study of topological superconductivity in the hybrid materials, we introduce two new device architectures:

- **Multiprobe Device**– Probes the spatial distribution of the LDOS using up to nine tunnel contacts in a gate-defined hybrid wire using the Lutchyn-Oreg framework.
- **Artificial Kitaev Chain**– Emulates the original Kitaev chain by coupling two (or more!) proximitized dots. The first implementation consists of two sites and thus realizes the so-called ‘poor man’s Majoranas’ [33].

By leveraging the prior fabrication techniques Figure 3.2, we extend the workflow to realize these devices. This section highlights and illustrates the key stages in fabrication and design considerations.

The important steps for a two-site Kitaev chain are shown in Figure 3.5, where an essential modification is the employment of two layers of gate electrodes. This prevents lift-off issues of closely packed gate structures. For instance, in Figure 3.4b, the separation between two gates is about 60 nm, making reliable liftoff challenging.

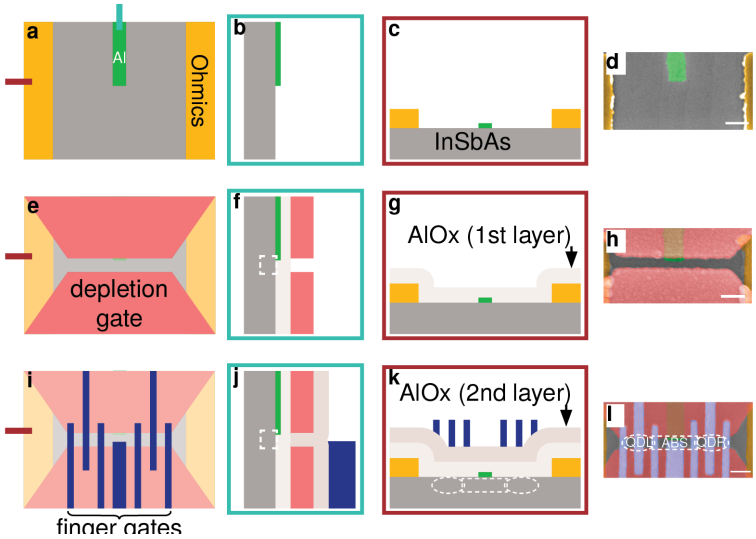

Figure 3.5: **Fabrication: a two-site Kitaev chain device.** Each row represents a fabrication step, showing a top-view schematic, two cross-sectional views (vertical in turquoise, horizontal in cherry) and a SEM image. The first row **(a-d)** is a device after the normal contacts deposition. The second row **(e-h)** is after the deposition of the two depletion gates, which defines a 1D channel. The end of the Al terminates within the channel, enabling a gate-tunable proximitized region. The third row **(i-l)** is after the deposition of seven finger gates. The central gate (shown in **(j)**) controls the ABS energies while the three side gates define a QD. All scale bars are 200 nm.

This is especially crucial for the multiprobe devices, where the first gate layer features complex geometry (see Chapter 4, Figure 4.2).

Figure 3.5a-d shows the device with the Al strip and two normal contacts. The Al strip has sharp and flat edges, which facilitates the alignment with the subsequent gates. Figure 3.5e-h shows the device after the first gate layer: the depletion gates. Energizing these two gates depletes the underlying 2DEG and confines the electrons in the channel, where quantum dots can be defined. It is important to ensure a sufficiently large separation between these two gates to prevent the channel pinch-off from fringing field. A general distance for our devices is between 175 nm and 250 nm. The end of the Al strip extends over the edge of the top depletion gates and stops within the channel, as shown in Figure 3.5h. The Al proximitize both the direct underlying and adjacent 2DEG, as in white dashed boxes in Figure 3.5f. Further electrostatic confinement induces ABS in that section. Two extra details are worth mentioning here. First, precise alignment of the Al strip and depletion gate is crucial. Misalignment risks either losing the proximitized region (if Al is covered by the top gate) or the gate tunability of the ABS (if Al continues to the bottom depletion gate). To minimize alignment drift, we use the fine alignment markers

when patterning the fine structures and 30 mins pre-exposure thermalization in the load-lock of e-beam lithography machine. Second, the depletion gates appear rather bulky compared to conventional gates in the QD [47]. This is because beyond the tunnelling spectroscopy, we were also interested in exploring dispersive gate sensing. With the common gate structures, the uncontrolled charge pockets around the finger gates introduce charge noise in the gate sensing signal [48]. To mitigate that, we route the finger gates exclusively over depletion gates to avoid direct capacitive coupling to the 2DEG. Therefore, large depletion gates simply allow more freedom in the arrangement of the fine gates. Figure 3.5i-l shows the device after the second gate layer: the finger gates. The central one, dubbed the "ABS gate" in our experiments, allows us to control the energies and the charge characteristics of the ABS. This tunability is essential for efficient Cooper pair splitter and artificial Kitaev chain. The wave function of the ABS also needs to extend over the distance between the QDs to mediate the transport, but it seems like this is never our concern in our experiments and we have observed an extended ABS up to 600 nm [49]. Each QD is defined by three finger gates: two cutters and one plunger. The outermost cutter gates can isolate the system from the reservoir of electrons in the normal contacts. This setup is useful for studying quasi-particle poisoning in a system where Al is floating. The inner cutter gates regulate the coupling strength between the two dots and are essential in engineering the Kitaev chain with a large excitation gap. The plunger gates move the dot levels, to find a spin-degenerate single orbital level.

The study of the two-site Kitaev devices in our hybrid 2DEG has yielded promising and more importantly, reproducible results, as shown in 6. This implementation in 2DEG, along with earlier realization in hybrid nanowires [50], demonstrates that the Kitaev chain physics is universal and independent of specific device geometry or material platform.

3.3.2 Fabrication of a three-site Kitaev chain

Extending the Kitaev chain is crucial for realizing topologically protected edge modes in Majorana-based qubits. In the section below, we present the endeavor in fabricating a three-site Kitaev chain, which enables the study of both edge and bulk DOS.

Figure 3.6 illustrates key fabrication stages and the final SEM. We introduce the third gate layer to for optimal functionality of such a device containing 15 gate electrodes, due to the addition of the middle contact and QD. First, Figure 3.6a shows the device before the first dielectric layer. Coupling three QDs requires two proximitized regions, and therefore two separate Al fingers. They are connected in a superconducting loop, allowing flux control of the phase difference between the Al fingers. A phase-biasing period of 40 μT is designed to ensure that required

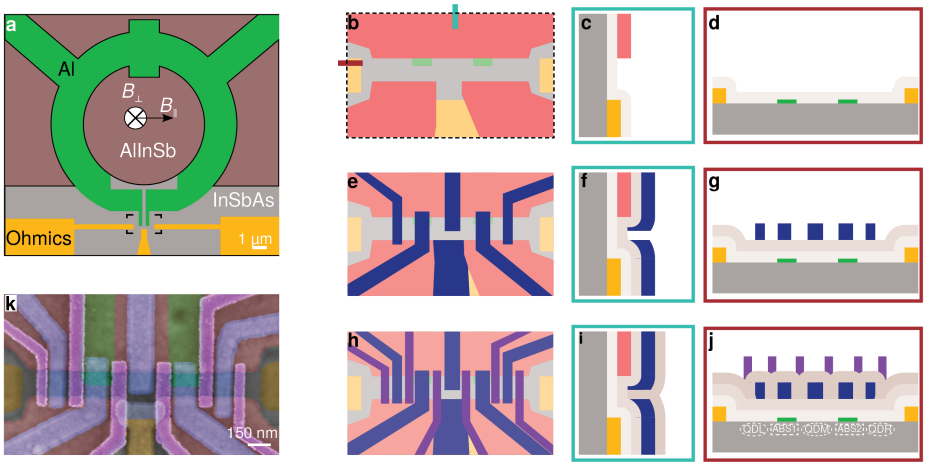

Figure 3.6: **Fabrication: a three-site Kitaev chain device. (a)** The device schematic after the normal contacts deposition. A superconducting loop with a diameter of about 10 um is used for phase-biasing. The bottom of the loop ends with two separate, narrow Al fingers, where three normal ohmics are deposited on the left, middle and right. **(b)** The device after the deposition of the depletion gates. Cross-sectional views along the vertical **(c)** and the horizontal **(d)** direction are shown as well. The different layer of AlOx dielectric is shown as a thin brown film with different tints. **(e-g)** The device after the deposition of the second layer of gates, including the three plunger gates (one for each QD), two ABS gates and the bottom cutter gate for middle QD. **(h-j)** The device after the deposition of the third layer of gates, including the outer and inner cutter gates for all three QDs. **(k)** The final SEM of the device.

magnetic field is well below the critical field of Al film, while remain robust to the flux noise within the fridge.

Figure 3.6b highlights the normal contacts and depletion gates. In order to define a 1D channel compatible with a middle tunnel probe, three depletion gates are deposited. Vertical and horizontal spacing between these gates is carefully designed to prevent unwanted depletion that could pinch off the middle probe. Furthermore, the top end of the middle contact remain lower than the bottom depletion gates to ensure propoer QD formation. Horizontal and vertical cuts are shown to illustrate the stacking of the different components of the device.

Figure 3.6e focuses on the second layer of gates: three plunger gates, two ABS gates and a middle cutter gate. Figure 3.6f shows that the bottom cutter gate is aligned to overlap with the middle contact to control the transparency of the barrier. The device is finalized in Figure 3.6h after the deposition of another six outer and inner cutter gates. The layout containing QDs and ABSs regions is shown

in Figure 3.6j, with a SEM shown inFigure 3.6k. The promising results especially on the bulk and edge density of states can be found in the manuscript [49].

With this rather short section, we conclude the standard fabrication methods for processing the InSbAs/Al 2DEG. With carefully designed layout and fabrication steps, high-quality devices with complex geometries have been realized.

3.4 The challenges: when things go wrong

This section may not be the common theme in other dissertations, but it reflects part of the journey and I believe this is the right place to document it. I have mentioned multiple times in this chapter that fine Al etch is *the* most crucial–and trickiest–step in our fabrication. Here I would like to add a personal touch to this topic by presenting some etching examples. Figure 3.7 provides a mixed collection.

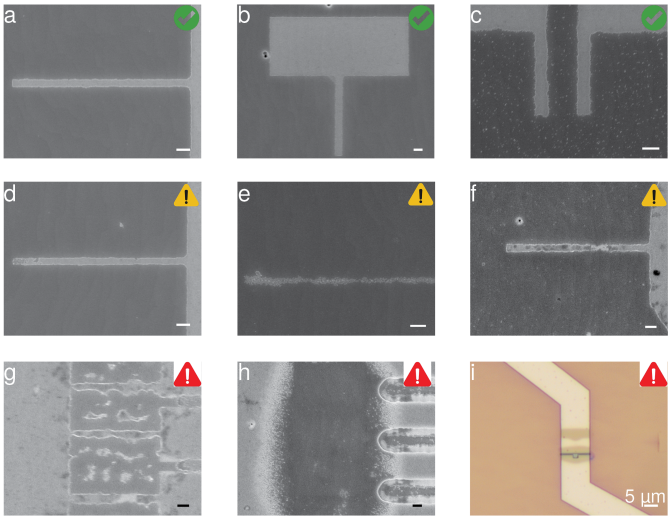

Figure 3.7: **Challenges in the selective fine aluminium etch.** Top row **(a-c)**: SEM of the devices with perfect (or good-enough) fine Al etch. The patterns match the design with a uniform creep distance within 50 nm. Middle row **(d-f)**: SEM of the devices with bad fine Al etch. Bottom row **(g-i)**: SEM (or optical image) of the device with failed fine Al etch, showing either under-etch **(g)** or excessive over-etch **(h-i)**. All scale bars are 200 nm unless specified within the image.

The first row Figure 3.7a-c show good "text-book" examples of fine etch: sharp edges, true-to-design geometry, and a uniform 30 nm to 50 nm creep. Devices with such etching results have been almost all functional, for example the device A in Chapter 4, the device 2 in Chapter 5 and the three-site device in the article [49]. There was this well-spread superstition that ugly mesoscopic devices are the best ones in the measurement. However, at this point, I stand by the belief that the beautiful ones are the true heroes.

That being said, it is easy to overlook how difficult it is to achieve a reliable fine etch. We believe the main cause of irreproducibility is poor adhesion of the PMMA mask. Therefore etchant can seep the structures underneath the mask via the capillary effect. The middle row of Figure 3.7 presents three mini examples: Figure 3.7d shares the same design and processing as Figure 3.7a on the same chip (2 mm apart). However, it shows different etch results, especially at the strip edges. We sometimes performed test runs and patterned the real devices in the second round of etch, just to increase our confidence in the etch results. Figure 3.7e is a representative image after a second etch run showing severe creep, whereas the test round yields perfect etch results. One can argue, that it is the trial etch and thus the resulting contamination degrades the result of the second etch. Figure 3.7f shows a poor etch outcome even after strictly following the standard procedure without a trial run. Since we are concerning with the creep and long subsequent fabrication time, this chip is abandoned.

There are also times when etch results get even worse despite following the exact recipe:

- Figure 3.7g: Under-etching, with poorly defined Al edges and leftover residues between the strips.
- Figure 3.7h and i: Over-etching is more common, where the fine structures are completely washed over.
- In some cases the over-etching is already visible under an optical microscope as an oval-shaped dark area on the mesa. Note that the shape of the exposed PMMA mask is still visible since Figure 3.7i (taken before the liftoff).

After enough trial and error, I managed to achieve a few decent etches. However, even up to my last etch in the cleanroom, I was never completely certain of the outcome until I checked the SEM.

Fortunately, my colleagues never stopped trying new methods and the recent development of using AlF_3 as the etch mask look quite promising. By fluorinating the top fraction of in-situ grown Al, the resulting AlF_3 mask adheres tightly to the remaining Al, improving etching reliability. I hope this new method helps fabricate the next generation of devices—and that the bad examples in this section stay in history.

4

Spatial dependence of local density of states in semiconductor-superconductor hybrids

Qingzhen Wang, Yining Zhang, Saurabh Karwal and Srijit Goswami

Majorana bound states are expected to appear in one-dimensional semiconductor-superconductor hybrid systems, provided they are homogeneous enough to host a global topological phase. In order to experimentally investigate the uniformity of the system, we study the spatial dependence of the local density of states in multiprobe devices where several local tunnelling probes are positioned along a gate-defined wire in a two-dimensional electron gas. Spectroscopy at each probe reveals a hard induced gap, and an absence of subgap states at zero magnetic field. However, subgap states emerging at finite magnetic field are not always correlated between different probes. Moreover, we find that the extracted critical field and effective g-factor varies significantly across the length of the wire. Upon studying several such devices we do however find examples of striking correlations in the local density of states measured at different tunnel probes. We discuss possible sources of variations across devices.

The work has been published in *Nano Letters* 2024, 24, 43, 13558-13563.

4.1 Prelude: Majorana in one-dimensional system

This section provides a brief introduction of the Lutchyn-Oreg model and a broader picture on the motivation of the study in this chapter.

4.1.1 Lutchyn-Oreg model

One of the assumption in the Kitaev chain model is that it the requirement of spinless electron and p-wave pairing. Materials of such properties have not been yet conclusively identified. However, it is possible to engineer the system with the conventional superconductor and semiconductor materials, and this idea was first explored by Lutchyn [51] and Oreg [52].

It is convenient to describe the hybrid one-dimensional (1D) system using the Bougoulivbov-de Gennes (BdG) formalism. The Nambu spinor basis is given by $\Psi = \left(c_{k\uparrow}, c_{k\downarrow}, c^{\dagger}_{k\uparrow}, c_{k\downarrow}, -c^{\dagger}_{k\uparrow} \right)^{T}$. This explicitly includes both electron and hole operators, as well as both spin species. The BdG Hamiltonian can then be written as:

$$H_{\mathrm{BdG}} = \zeta_k \tau_z + \alpha k_z \sigma_y \tau_z + \frac{1}{2} \mu_B g \mathbf{B_z} \boldsymbol{\sigma_z} + \Delta \tau_x \tag{4.1}$$

where the Pauli matrices τ_i and σ_i acting on the particle-hole or spin space of the Hamiltonian. The Hamiltonian contains the following terms:

- The first terms represents the kinetic energy of the electrons along the z-axis with $\zeta_k = (\frac{p_z^2}{2m^*} - \mu)$ with m^* the effective mass and μ the chemical potential
- The second term describes the Rashba spin-orbit coupling, with a spin-orbit field along y-axis
- The third term is the Zeeman energy provided by the external magnetic field along z-axis, notice that it is perpendicular to the spin-orbit field
- The last term is the s-wave pairing , characterized by the pairing parameter Δ.

The synergy of all these terms is necessary to drive the system into a topological phase. The effect of them parameters on the the band structure has been clearly discussed and visualized in multiple sources, such as this recent thesis [53]. First, MZMs appear at the edges of the wire, whose wavefunction decay exponentially into the bulk. Secondly, the superconducting gap at $k = 0$ close and then re-opens as a result of increasing Zeeman field, signaling a transition from the trivial to the topological phase. The gap at finite momentum remains finite, due to the presence of the spin-orbit coupling.

In an ideal model, the calculated energy spectrum at different locations in a wire is plotted in Figure 4.1. The calculation is done in *Kwant* for a 2.5 μm hybrid

wire with the following parameters: lattice parameter $a = 10\,\text{nm}$, $\mu = 0$, effective mass $m* = 0.016m_e$, superconducting gap $\Delta = 0.25V$ and Rashba parameter $\alpha = 0.25\,\text{eVÅ}$. At the edge, a strong zero-bias peak (ZBP) is expected due to the presence of Majorana wavefunction. As one move away from the edge into the bulk, the DOS of the ZBP gradually weakens, while the feature associated with the gap closing and reopening becomes more prominent. Experimentally, the LDOS can be detected via local tunnelling spectroscopy, where resonant tunnelling through the subgap states leads to conductance peaks at bias voltages corresponding to the transition energy E_0.

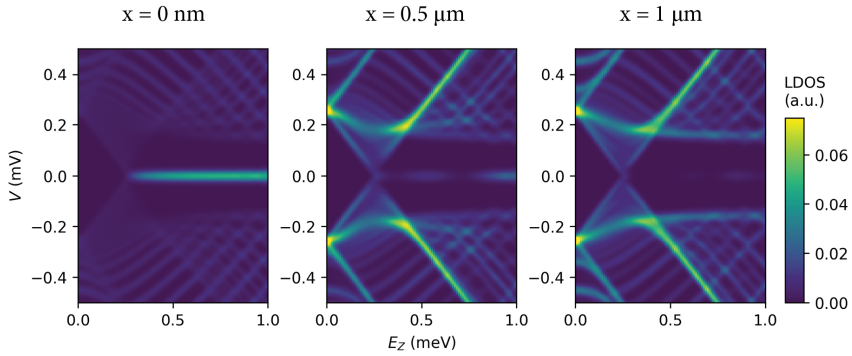

Figure 4.1: **Calculated LDOS in a Majorana wire.** For a hybrid wire of 2.5 μm, the local DOS is plotted as a function of the Zeeman energy E_z at different locations: at the edge **a**, 0.5 μm **b** and 1 μm **c** from the edge. The ZBP is strongest at the edge and weakens towards the bulk, while the gap-closing and reopening feature becomes more pronounced.

Because the LDOS at the edges of the system is most accessible, the ZBP has long been considered a hallmark signature of the MZMs and the associated topological phase. Unfortunately, this has not passed the "reality check", as many trivial reasons, such as the disorder or the smooth potentials in those hybrid wires can lead to ZBP (even at quantized values of $2e^2/h$). I refer the reader to these two reviews [7, 8] for more details on the limitations in the realistic Majorana devices. It is clear back that in order to establish the existence of the Majorana zero modes, more unique signatures are required. One of those is the concomitant observation of the bulk gap reopening and the ZBP at the edge [54, 55], which forms part of the motivation for this study. At the same time, many assumptions introduced in the Lutchny-Oreg model Eq. 4.1 was obviously oversimplified. One such example is the treatment of the proximity effect. In the model, the superconductor is only treated as a pairing potential for the electrons in the semiconductor and has no other effect. In reality, the coupling between the two materials leads to different degrees of metallization. A strong coupling leads to effectively smaller g-factor and weaker spin-orbit coupling

of the whole hybrid, because the electrons tend to inhere the material properties of the superconductor. This remained largely unexplored due to limitations of early-generation device (the nanofabrication quality and measurement techniques), until a recent notable effort by [56], which systematically investigated this issue. Along similar lines, this study aims to address this gap of knowledge in realistic devices by employing a "multiprobe" device geometry to gain deeper understanding into hybrid systems.

4.2 Introduction

Majorana bound states (MBSs) obey non-Abelian exchange statistics and are potential building blocks of topological qubits [5, 57]. In this context, one-dimensional (1D) semiconductor-superconductor hybrids have been widely studied, where a topological phase transition is accompanied by the emergence of MBSs at the system edges [51, 52]. together with a closing and reopening of the superconducting gap in the hybrid bulk [58]. Tunnelling spectroscopy provides information about the local density of states (LDOS), and is often used to search for signatures of MBS [59]. However, it has been suggested that some of these observations could arise due to trivial reasons such as disorder or inhomogeneity of the chemical potential [7, 10, 46, 60–65]. Strong local perturbations would effectively segment the wire and thus prevent the creation of a global topological phase. It has therefore become clear that a prerequisite for reliably creating MBSs is spatial uniformity of microscopic properties across the length of the 1D hybrid system. These include the chemical potential, the induced superconducting gap and the effective g-factor.

Information about the bulk density of states of the hybrid region can be inferred by measuring the non-local conductance in a three-terminal geometry [9, 56, 66–68]. However, these measurements are only sensitive to the minimum energy scale of all the bulk states, and thus do not immediately reveal local properties. An alternative method to probe the bulk, and therefore get information about the wave function of subgap states, is to perform local tunnelling spectroscopy along the hybrid. While such experiments have been performed in hybrid nanowires, technical difficulties have led to soft superconducting gaps [54] or additional tunnelling currents that obscure the direct measurement of the LDOS in the hybrid [69]. Furthermore, the transparency of these tunnel probes is not tunable, thus preventing a systematic study of LDOS in the bulk. These issues can be mitigated by using a two-dimensional electron gas (2DEG), which offers flexibility in device design and fabrication, allowing one to pattern an arbitrary number of tunable tunnel probes along the 1D hybrid, thus providing information about spatial variation in the LDOS. It has also been proposed that a gate-defined hybrid wire with multiple tunnel junctions is more resilient to inhomogeneous confinement potential, thereby making this device geometry a promising way to probe the LDOS [70]. Such a

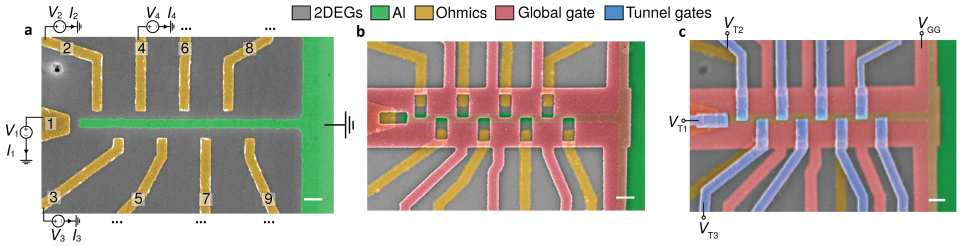

Figure 4.2: **The multiprobe device. (a)** A false-colored scanning electron microscope (SEM) image of a device with the Al strip and normal contacts. Nine normal contacts are placed from the edge of the wire ("1") to the bulk (up till "9"). In the circuit diagram, the applied bias voltages and measured currents are only shown for the first four probes for simplicity. **(b)** SEM image of a device after the global gate deposition. **(c)** SEM image of a device after the tunnel gates deposition. The applied global gate voltages V_{GG} and the applied voltages of the first four tunnel gates V_{T1} to V_{T4} are labeled. The first and second images are from lithographically similar devices. All scale bars are 200 nm.

geometry has been studied previously in devices based on InAs/Al 2DEGs [71]. However, the limited number of probes make it difficult to extract information about the spatial dependence of microscopic parameters along an extended wire.

Here we study the LDOS of quasi-1D hybrid wires, defined by electrostatic gating in an InSbAs 2DEG with epitaxial aluminium. Several tunnel probes positioned along the wire enables a simultaneous measurement of the position-dependent LDOS. At zero magnetic field, we measure a hard superconducting gap without any subgap states, confirming a strong proximity effect and the presence of clean tunnel junctions. As we increase the magnetic field, we in general do not observe any obvious correlation between the emerging subgap states at neighbouring probes, suggesting that these states are localized within 250 nm along the hybrid. Furthermore, we find that the critical field (B_c) and the effective g-factor (g^*) exhibit significant fluctuations along the wire. In contrast, some devices show remarkably correlated subgap states with a spatial extension of more than 1.1 μm. We discuss possible explanations of this inconsistency between different devices.

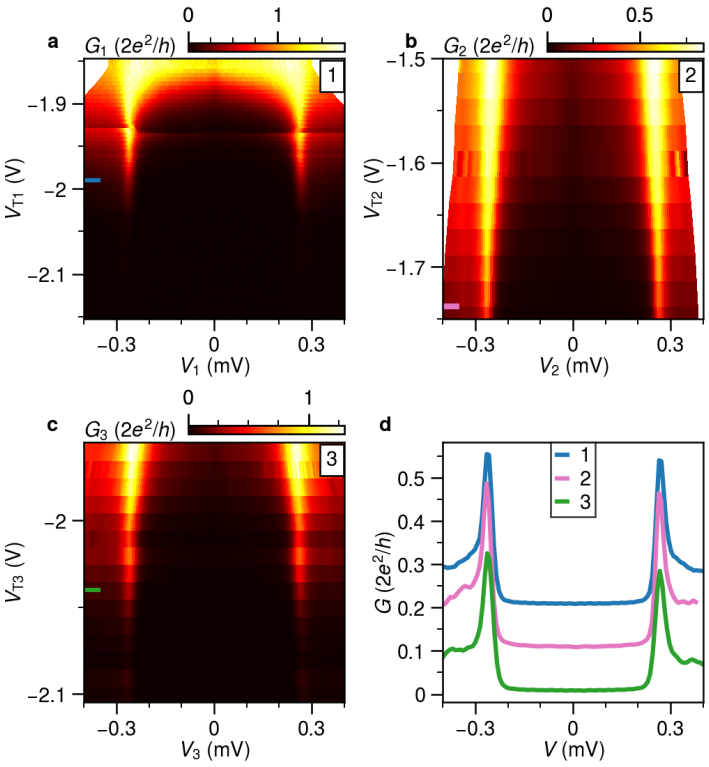

Figure 4.3: **Hard superconducting gap at zero magnetic field. (a-c)** Tunnelling conductance G_i as a function of individual tunnel gate TG_i and the corresponding applied bias voltage V_i ($i \in \{1,2,3\}$). With a substantial change of the out-of-gap state conductance, no discrete subgap states are observed within the gap, indicating clean tunnel junctions. Probe numbers are labelled on the top-right corner. **(d)** Exemplary line traces indicate that the presence of two sharp coherence peaks and a hard induced superconducting gap (the lines are laterally offsetted by $0.1G_0$ for clarity). The measured lock-in signals are higher than the noise floor due to the additional parasitic capacitance in the circuit and a detailed comparison with the numerical derivative of the DC current is made in the Fig. S1. V_{GG} is at -2.6 V.

4.3 Results

4.3.1 Device and basic characterization

The InSbAs 2DEG with epitaxial aluminium grown by molecular beam epitaxy has been shown to have a good proximity effect, high g-factor and large spin-orbit coupling [29, 41]. The structure of the multiprobe devices is illustrated in Figure 4.2, together with the circuit diagram. First a 2.5 μm-long, 130 nm-wide aluminium strip is defined by chemical etching and nine Ti/Pd normal contacts are deposited along the strip with a center-to-center separation of 250 nm. The aluminium strip remains electrically grounded during measurement, and the bias voltages applied on each contact V_i (i$\in \{1,2,...9\}$) can be varied independently. After depositing a 20 nm thick AlOx dielectric layer, a global gate (GG) is deposited. Applying a negative voltage to GG depletes the 2DEG around the Al strip, thereby defining the 1D hybrid wire. At the same time, the 2DEG between any two normal contacts is also depleted, ensuring that no current flows between neighboring tunnel probes. After depositing an additional 20 nm layer of AlOx, nine tunnel gates are deposited over the pinholes in the GG. The applied tunnel gate voltages V_{Ti} (i$\in \{1,2,...9\}$) control the individual tunnel barrier, allowing one to perform local spectroscopy along the wire. The final image of one of the three measured devices (denoted Device A) is shown in Figure 4.2c. We also present measurements of two other devices (denoted device B and C) with the same material but with only four tunnel probes (device images shown in Figure 4.6).

All measurements were conducted in a dilution refrigerator with 20 mK base temperature with standard lock-in techniques. More details about the measurement scheme can be found in the measurements methods in the supplementary information.

We begin the device characterization through tunnelling spectroscopy measurements as a function of tunnel gates. Three examples of the measured spectrum are illustrated in Figure 4.3(a-c). In the tunnelling regime (Figure 4.3d), all three probes show sharp superconducting coherence peaks at approximately $\pm$ 0.26 meV and a suppression of the in-gap conductance. The tunnel gate voltages V_{Ti} affect the transparency of the tunnel junctions. While the the out-of-gap conductance varies between around half of the G_0 to nearly zero, the coherence peaks remain at the same energies, as shown in Figure 4.3a-c. Importantly, we note that there are no obvious charging effects, and no additional subgap states appear over this range of transparency. These spurious states are often observed in hybrid devices and are attributed to a nonuniform confinement potential in the semiconductor junctions [61, 70, 72]. The absence of these subgap states at zero magnetic field allows us to extract information about the LDOS in the hybrid wire.

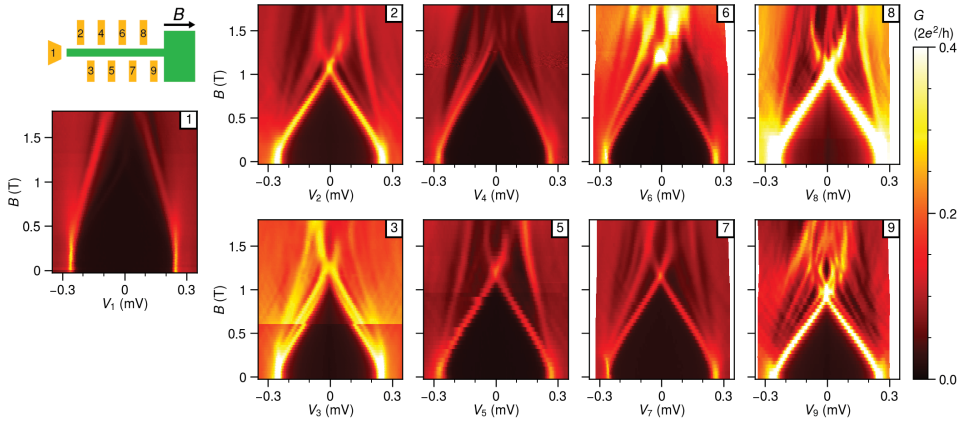

Figure 4.4: **Field evolution of LDOS for device A.** Tunnelling conductance G of each tunnel probes with a schematic of the device. The measurements of probe 1234 and 6789 are obtained by sweeping the four biases at the same time and recording the signals with four lock-in amplifiers. The spectrum of probe 5 is obtained in a three-terminal measurement circuit. No obvious correlation of subgap states between neighboring probes are observed. V_{GG} is at -2.6 V.

4.3.2 Spatial dependence of microscopic parameters

The precursor of MBSs in a 1D hybrid system is an extended Andreev bound state (ABS) across the entire wire. By applying a large enough magnetic field, a topological phase may arise, where the ABS evolves into spatially separated MBSs localized at the ends of the wire. A persisting ZBP is then expected to appear at the edges, along with a closing and reopening of the gap in the bulk of the wire. If the spatial separation of a series of tunnel probes is sufficiently small, it should then be possible to map the wave function of the MBSs, which in theory decays exponentially from the wire edge into the bulk [70].

We measure the tunnelling conductance as a function of the individual applied bias V_i and a global magnetic field B parallel to the aluminium strip, as shown in Figure 4.4. The tunnel gates voltages are adjusted such that all probes have out-of-gap conductance well below G_0, and are therefore in the tunnelling regime. The most clear observation from Figure 4.4 is that there is no systematic correlation in the field evolution of the subgap states moving from the edge to the bulk, indicating the absence of an extended ABS in the wire. For example, the field value where the lowest subgap states cross zero energy differs by about 400 mT between probe 1 and 9. Furthermore, even when we compare the subgap states from neighboring probes (separated by 250 nm), their evolution with magnetic field seems uncorrelated. For example, the subgap states from probe 2 reach zero energy

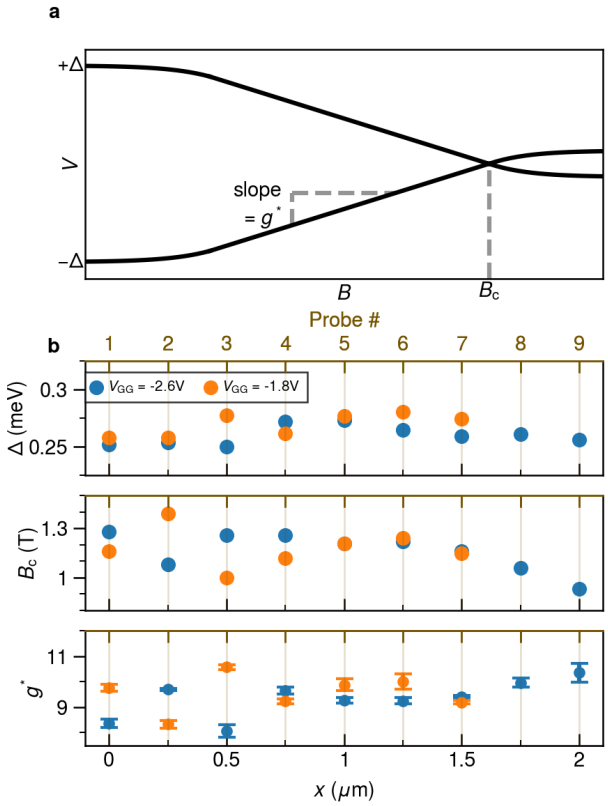

Figure 4.5: **Spatial dependence of superconducting gap Δ, critical field B_c and effective g-factor g^*. (a)** A sketch of the field dependence of the lowest subgap states. **(b)** Δ, B_c and g^* are plotted as a function of distance x to the edge of the wire (bottom axis) and the corresponding probe number (top axis).

at around 1.1 T while this occurs at 1.3 T for probe 3. The measured spectra of probe 3, 5 and 7 look qualitatively similar, but a more detailed comparison shows that the extracted microscopic parameters are different, and thus these subgap states are also not actually correlated (detailed in Figure 4.5). The measured tunnel spectra at individual probes can also depend on the chemical potential in the wire. Thus we also performed the measurements at $V_{GG} = -1.8\,V$, just below the threshold voltage required to deplete the bare 2DEG. Similarly uncorrelated subgap states are observed for this set of measurements Fig. S2).

We use the the measurement presented in Figure 4.4 and Fig. S2 to extract the spatial dependence of three microscopic parameters in the hybrid: the induced superconducting gap Δ, the critical field B_c and the effective g-factor g^* of the lowest-energy subgap states. They are labelled in an exemplar field evolution of

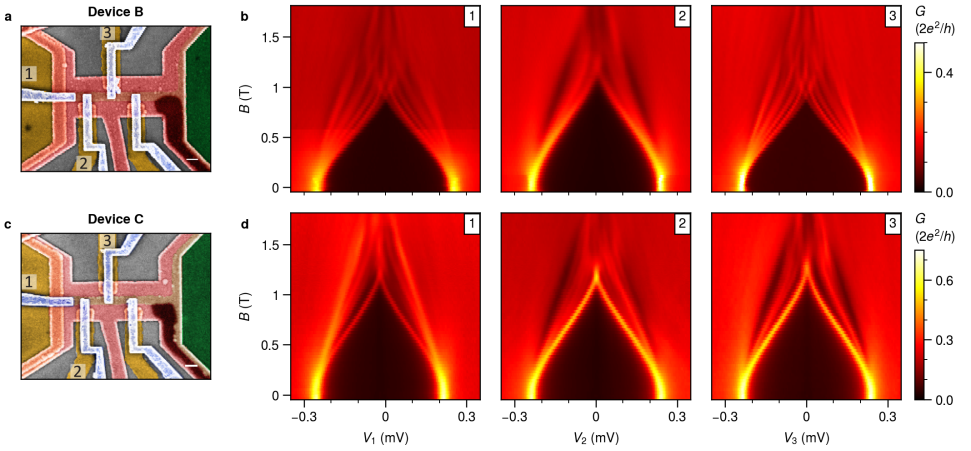

Figure 4.6: **Field evolution of LDOS on device B and C**. **(a)** The false-colored SEM image of device B with a similar shape of Al strip, but only four normal contacts that are separated by around 500 nm. The scale bar here is 200 nm. **(b))** The field dependence of the leftmost three tunnel probes. The lowest three subgap states spectra have almost the same field dependence between probe 1 and probe 3, but only the second lowest subgap states are present in probe 2. **(c)** The false-colored SEM image of another four-probe device C and **(d)** the field evolution. The lowest subgap states are almost perfectly correlated within all three probes. Details on peak-matching for confirming these correlations are shown in Fig. S6.

the lowest subgap states, as shown in Figure 4.5a. The size of the induced gap Δ, B_c and g^* characterize the degree of hybridization of the wavefunction across the superconductor-semiconductor interface. It has been shown that this coupling between the two materials in hybrid nanowires can be modulated by the use of the electric field [55, 56, 73]. Δ is determined by locating the applied bias voltages corresponding to the coherence peaks maxmima at B =0. B_c is defined here as the field value at which the lowest states reach zero energy and is extracted by locating the first local maximum in the zero-bias conductance traces as a function of magnetic field. g^* is defined by $g_{eff} = \frac{2}{\mu_B}|\frac{\Delta E}{\Delta B}|$ [74], where μ_B is Bohr magneton and $|\frac{\Delta E}{\Delta B}|$ the absolute average of the slope from the linear fitting of the lowest subgap states at positive and negative biases.

As seen in Figure 4.5b, the induced gap Δ in our devices varies between 0.25 meV and 0.28 meV along the wire, with an average value of 0.26 mV (GG = −2.6 V) and 0.27 mV (GG = −1.8 V). Additionally, the similar magnitude at two different V_{GG} is probably due to the weak gating effect of the hybrid sections, which is achieved purely by the fringing field of the applied global gate voltages. The spread of the data points can be captured by the calculated coefficient of variation (CV), which is the ratio of the standard deviation to the mean. CV_Δ about 3.1% for GG = −2.6 V

and 3.4% for GG = −1.8 V. This variation may be due to mesoscopic variations in the wire or the different tunnel broadening at each probe. For the critical field B_c, however, we find a much stronger variation of the extracted values across different probes. The averaged value is at 1.16 T for GG = −2.6 V and 1.18 T for GG = −1.8 V, with the CV reaching about 9.4% in both cases. This significant spread could arise from a nonuniform electro-chemical potential in the wire, which is undesirable in realizing a global topological phase transition. The effective g-factor is indicative of the extent of hybridization of wavefunction throughout the cross-sectional interface of the hybrid [55, 73, 74], and eventually determines the required critical field for a topological phase transition. The extracted data here shows a large amount of fluctuation, ranging from about 8 to 11. These values are significantly smaller than the g-factor of bare InSbAs 2DEG [29, 75], indicative of hybridization with the superconductor. The error bars originate from the process of linear fitting. For V_{GG} = −2.6 V, the mean is 9.4 with a CV of 6.7%, and for V_{GG} = 1.8 V, the mean is 9.6 with a CV of 7.5%. The significant spread of B_c and g^*, together with the uncorrelated LDOS shown in Figure 4.4, indicates a non-uniform chemical potential along the wire, which is nonideal for creating Majoranas.

4.3.3 Extended subgap states in other multiprobe devices

We repeat similar measurements in two additional multiprobe devices with a similar design. The SEM images of devices B and C are shown in Figure 4.6a and Figure 4.6c, respectively. These devices are fabricated with the same 2DEG heterostructures and have the identical shape of Al strip. However, four normal probes are now arranged with a larger separtion of around 500 nm. Basic characterization in Fig. S4 confirms similar hard gap and absence of subgap states in tunnelling spectroscopy, as the behaviour observed in device A. Field dependence measurements are conducted in a comparable tunnelling regime as depicted in Figure 4.4 for the first three probes from the edge for both devices. Remarkably, the subgap states of probe 1 and probe 3 now have a remarkably similar dependence on the magnetic field, which we attribute to extended states over 1.1 μm. However, spectroscopy at probe 2 looks different. While some states evolve similarly at all three probes (Fig. S6), others do not. This suggests that the wavefunction of these states is not uniform across the width of the hybrid region. The measurements for device C shows that the lowest subgap states from all probes have the same dependence on the magnetic field, confirming their spatial correlation over 1.1 μm (Fig. S6).

4.4 Discussion

The variations in the extent of the ABS wavefunction across different devices warrants a further discussion. We propose a few explanations for this observed discrepancy. First of all, we know that the semiconductor 2DEG used in this

study have a typical peak mobility of about 25 000 cm^2/Vs (which corresponds to a mean-free path of about 250 nm) [29]. Thus, intrinsic disorder could be a factor responsible for the device to device variations. Disorder can also result in a non-uniform chemical potential along the wire, causing the wavefunction of the ABSs to be spatially non-uniform across the width of the wire. This could partially explain the observations in device B.

Additionally, while the device geometry of device A looks nominally similar to that of device B/C (apart from the number of probes), they actually have different dimensions of the pinholes and dielectric thicknesses (Fig. S5), which could potentially lead to different electric fields at the hybrid region. In fact, we observe this experimentally while measuring the tunnelling spectra as a function of tunnel gate voltages at finite field (Fig. S4). The lowest energy subgap states in device A can be affected upon changing the the corresponding tunnel gate voltages, in contrast with device B/C, where they remain unaffected. To qualitatively understand this difference, we performed electrostatic simulations in COMSOL, based on the realistic device geometry (Fig. S5). We find that in device A, the tunnel gate voltages can create stronger fringing fields in the hybrid region (Fig. S3) and thereby effectively lead to the formation of invasive tunnel probes. On the other hand, as a result of the narrower pinholes and the thicker dielectric layers, the tunnel gates in device B/C have a significantly weaker effect on the hybrid region. This is in accordance with the experimental observations whereby device B/C show stronger correlations between probes as compared to device A. Therefore, it is important to take these electrostatic effects into consideration while designing devices to study the LDOS in hybrid systems.

4.5 Conclusions

In conclusion, we have used tunnelling spectroscopy to investigate the local density of states in gate-defined wires based on a 2DEG semiconductor-superconductor hybrid structure. This is achieved by implementing a multiprobe device geometry, with up to nine side probes placed at different positions along the wire. At zero magnetic field, we observed hard superconducting gaps and clean tunnel junctions, indicating uniform proximity over 2.5 μm. As the magnetic field increases, subgap states appear and eventually cross zero energy. However, these states are generally not correlated between neighboring probes. The critical field B_c and effective g-factor g^* are extracted at two different global gate voltages V_{GG} and exhibit significant spatial fluctuations. Measurements from comparable devices show a completely different behaviour, where the subgap states evolve identically as a function of magnetic field, suggesting correlations over 1.1 μm. In particular, even in the case of perfect probe-to-probe correlation, we find no clear evidence of a gap reopening, suggesting that the non-uniformity in our devices may be more than

what is required to host a global topological phase [76].

4.6 Author contributions

Q.W. and S.K. fabricated the devices. Measurements were performed by Y.Z. and Q.W. The manuscript was written by Q.W., Y.Z. and S.G., with inputs from all coauthors. S.G. supervised the experimental work.

4.7 Supporting Information

Device Fabrication, Measurement methods, COMSOL simulation, Field evolution, Effect of tunnel gates, Identification of subgap states, Characterization of measurement circuits

4.8 Acknowledgments

We would like to express our gratitude to Nick van Loo and Greg Mazur for their constant support and productive, in-depth discussions at various stages of the work. We also want to thank Ji-Yin Wang, Vukan Levajac, Bas ten Haaf and Christian Prosko for providing valuable feedback on the manuscript. We thank Di Xiao, Candice Thomas and Michael J. Manfra for providing the semiconductor heterostructures used in this work. The experimental research at Delft was supported by the Dutch National Science Foundation (NWO) and a TKI grant of the Dutch Topsectoren Program.

4.9 Personal Remark (exclusive to this thesis)

I am almost giving up on presenting this experimental observation to the scientific community, at large because the results appeared "negative," in the sense that they contradicted the predictions of the simple theoretical model.
In retrospect, I realize that I had subconsciously approached the process of writing a scientific paper as an opportunity to "showcase" achievements. This was a misconception. I now believe that the true purpose of publishing is to disseminate findings that you—if not only you—believe may hold value for the community. Everything else—the recognition, impact, or prestige—are merely by-products, like the transient gases released in a fermentation process: briefly noticeable, yet destined to dissipate into the air.

4.10 Data availability

Raw data and analysis scripts for all presented figures are available at zenodo.org/doi/10.5281/zenodo.11203149

4.11 Supplementary information

4.11.1 Fabrication

Three devices were measured to obtain the data presented in the main text and Supplementary (device A, B and C). To prevents the potential intermixing of Al and Sb at high temperature, all the fabrication processes are performed at room temperature unless otherwise specified. We use electron beam lithography to define the required nano-structures and use unexposed PMMA as etch masks. The device fabrication starts by etching the Al and the 2DEG in undesired areas. The Al etch is performed in Transene D etchant at a temperature of 48.2 °C for 9 s. Afterwards, using the same PMMA mask, the 2DEG is etched in a III-V etchant (560 mL deionized water, 5 mL H2O2 and 4 mL 85% H3PO4 and 9.6 g citric acid powder) for 70 s. This leads to an etching depth of about 75 nm and produces a series of un-etched units (called "mesa") which are electrically isolated. Then a sets of fine markers made of Ti/Au are evaporated around each mesa. The purpose of the fine markers is to improve the alignment accuracy between the Al strip, normal contacts and two gate layers to ensure the functionality of the final device. The next step is to define the Al strip, where we carry out a second Al etch in 38.2 °C Transene D for 10 s. Multiple fine normal contacts made of 5 nm/15 nm Ti/Pd are then deposited around the Al strip. Subsequently, a thicker 5 nm/115 nm Ti/Au evaporation defines the contact leads. Afterwards, we deposit a 20 nm-thick global AlOx dielectric at 40 °C. The first layer of gate electrodes (global gate) are formed with a 5 nm/25 nm Ti/Pd evaporation for the fine structures, and then a 5 nm Ti and 115 nm Au evaporation for the coarse gate leads. After depositing the second layer of 20 nm-thick global AlOx dielectric, we deposit a 5 nm/35 nm Ti/Au for the fine structure of the second gate layer and an additional 5 nm Ti/115 nm Ti/Au evaporation for the coarse gate leads.

4.11.2 Measurement Methods

For all the measurements, the alignment of the magnetic field with respect to the gate-define wire is expected to be accurate within ± 10° and calibrated through performing tunnelling spectroscopy of the hybrid section as a function of field angle. During the transport measurement, the aluminium is always electrically grounded. Each available Ohmic lead is biased with both DC and AC voltages and also connected to a current-to-voltage converter, transmitting the outcome to Keithley multimeter DM6500 and lock-in amplifer SR830. Two types of circuits are implemented: for the results presented in Fig. 2, probe 5 in Fig. 3 and Fig. 5b, a common three-terminal circuit as presented in [77] is used. The rest of measurements, in Fig. 3 and Fig. 5d, are acquired with a special multi-terminal circuit. For the case of Fig. 3, the same DC voltage biases are applied on four different probes simultaneously, but each with an AC excitation of distinct frequencies. Thus, we can register

four lock-in responses concurrently and perform more efficient measurements. In particular, we have compared the results obtained in the multi-terminal circuit configuration with those obtained with the simplistic two-terminal circuit, and found no qualitative difference in determining the energies of the subgap states Fig. S7.

In the three-terminal circuit, when a DC voltage and a lock-in AC excitation is applied to one Ohmic contact, the another one is kept grounded and vice versa. The amplitudes of AC excitations are always 5 μV and frequencies are 19.99 Hz (lockin-1) and 29.99 Hz (lockin-2). In this way, we can measure the full conductance matrix G in two measurement runs . In the multi-terminal circuits, if two DC biases are swept simultaneously, the frequencies of the AC excitations are 19.99 Hz (lockin-1) and 27.77 Hz (lockin-2). If four DC biases are swept, the frequencies of the AC excitations are 23.33 Hz (lockin-1), 27.77 Hz (lockin-2),13.33 Hz (lockin-3) and 19.99 Hz (lockin-4). Therefore, the tunnelling signals at each tunnel probe can only be demodulated by the single lock-in amplifier whose AC excitation has the same frequency. The voltage-divider effect is accounted for by correcting the real DC voltage drop on each contact with the known fridge line resistances and the resistance from the current-to-voltage converter module. In this way, the evolution of the energies of the subgap states as a function of gate voltage or magnetic field can be correctly resolved. Offsets of the applied voltage biases on each contacts are corrected via averaging the coherence peaks in the conductance line traces.

4.11.3 COMSOL Simulations

We use AC/DC module in COMSOL Multiphysics 6.1 to simulate the electrostatics in a simplified but realistic geometry. To be more precise, the following specifications are taken directly from the multiprobe devices shown in the main text: the thickness of the 2DEG, the width and thickness of the aluminium strip, the thickness of the AlOx dielectric, the relative position and the size of the pinhole, the thickness of the global gate and tunnel gate layer. Note that the 2DEG is treated as a semiconductor material with a relative permittivity of 17.7. Aluminium is kept electrically ground and the voltages are applied to the global gate and the tunnel gate. The only variance between device A and device B/C are the different AlOx thickness and the width of the pinhole. The plots shown in Figure 4.S5 are obtained by performing a parametric sweep of the V_{GG} and V_{TG} with 1 V step.

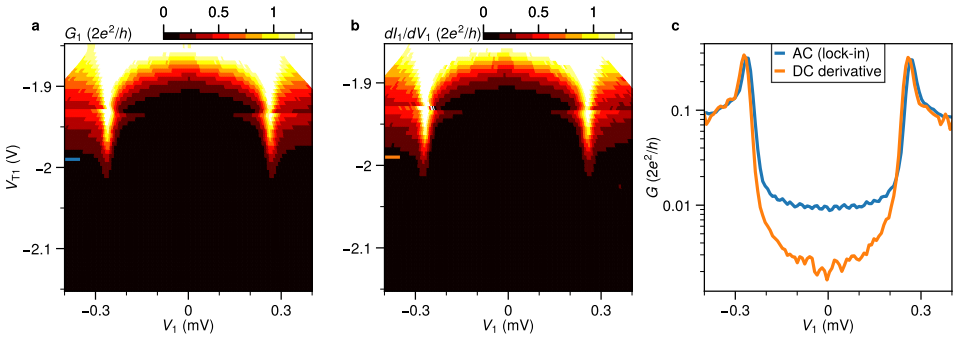

Figure 4.S1: **Comparison of the AC and DC signals** In this example, the conductance is either measured directly with lock-in amplifier (**a**, Figure 2a in the main text), or calculated with a numerical derivative of the DC current (**b**). The line-cut taken at the same gate voltage (**c**) shows that the in-gap conductance in the DC derivative is about an order of magnitude smaller that of the lock-in signal. This is because the additional parasitic components in the circuit induce an additional phase shift, thus making the amplitude of the measured lock-in signal higher. A Savitzky–Golay filter of window length of 5 is applied for the DC current before taking the numerical derivation.

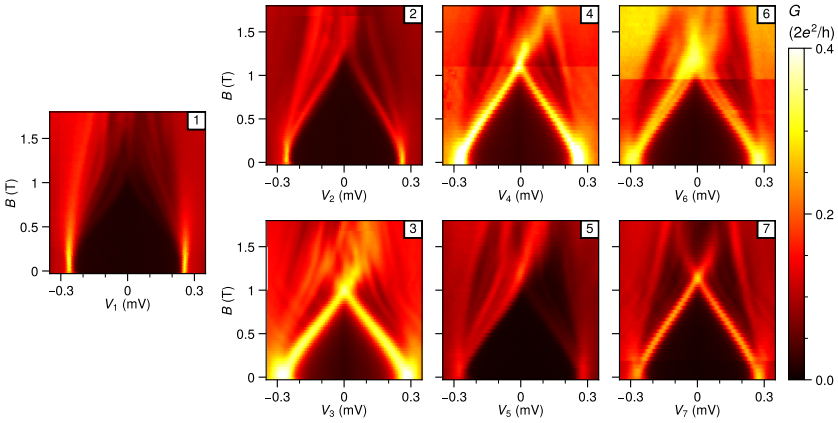

Figure 4.S2: **Field evolution of LDOS at $V_{GG} = -1.8$ V: Device A.** Similar to the behavior observed in main text FIG. 3, no obvious correlation of subgap states between neighboring probes are observed. Note that the field evolution has only been recorded for the first seven probes because of difficulties in adjusting the the tunnel gates for Probe 8 and Probe 9.

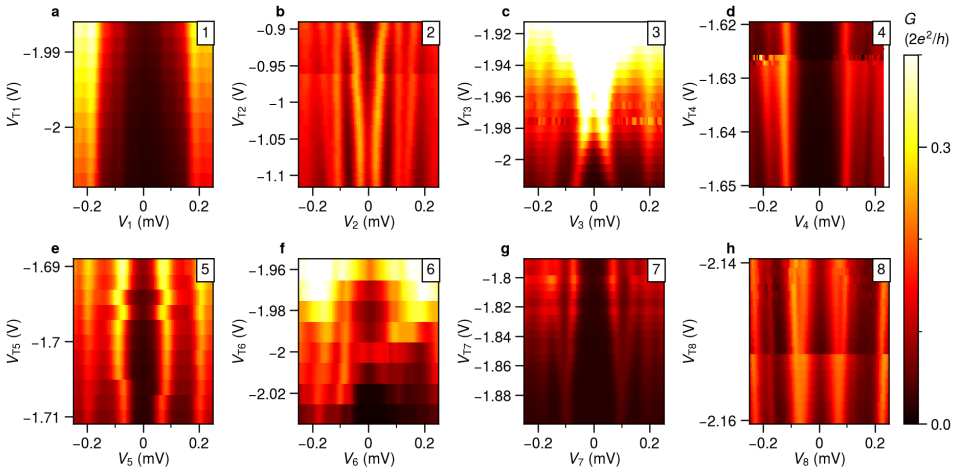

Figure 4.S3: **Effect of tunnel gates on spectroscopy: Device A**. The probe numbers are indicated in the top left of each figure. Overall, the subgap states do not stay at constant energies upon changing the corresponding tunnel gate voltages, indicating that the tunnel gates can have an effect on the hybrid region. This observation also indicates that the electrostatics can lead to false-positive observation of correlated subgap states, as a result of fine-tuned gate voltages.

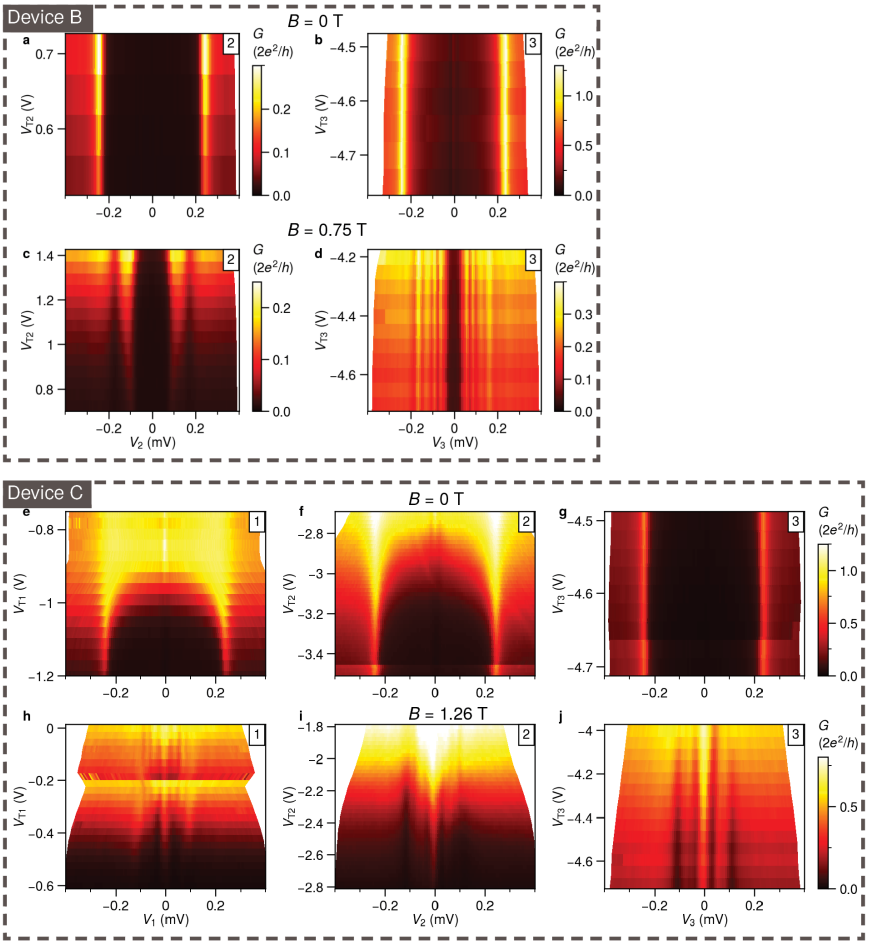

Figure 4.S4: **Effect of tunnel gates on spectroscopy: Device B and C.** Hard gaps without the subgap states (**(a-b) and (e-g)**) are observed are observed for both devices. At a finite field, the subgap states stay at almost the same energies as a function of tunnel gate voltages over a large range of transparency (**(c-d) and (h-j)**). Note that for device B, the tunnel gate T1 has almost no tunability of the junction transparency, and therefore only the T2 and T3-dependence are shown here.

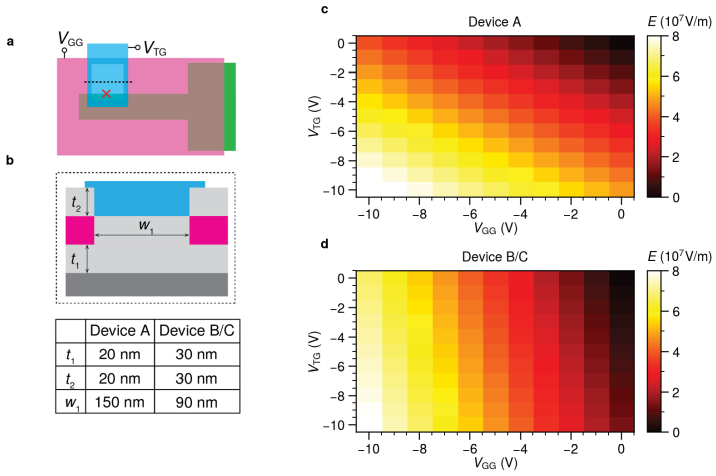

	Device A	Device B/C
t_1	20 nm	30 nm
t_2	20 nm	30 nm
w_1	150 nm	90 nm

Figure 4.S5: **COMSOL simulations of devices. (a)** Top view of the mulitprobe device, with only one representative pinhole on the global gate and only one tunnel gate. The simulated electric field strength at the red cross is chosen to represent the effect of the applied global gate voltages V_{GG} and tunnel gate voltages V_{TG}. **(b)** A cross-sectional view of the device stack, taken along the dashed line in **(a)**. The length scales that are relevant for the electrostatics are the thickness of the first ALD layer (t_1), the thickness of the second ALD layer (t_2) and the width of the pinhole (w_1). The table summarizes these parameters. **(c)** The simulated electric field norm for device A as a function of V_{GG} and V_{TG}. The change in the field amplitude as a function of only TG or GG of the same range is very similar. **(d)**The simulated electric field norm for device B/C. In contrast to **(c)**, now the global gate has a much stronger effect on the 2DEG than the tunnel gate. This is consistent with the overall thicker dielectric thickness (t_1 +t_2) and the smaller pinhole width (w_1) in device B/C, compared to device A.This may explain the weaker tunnel gate effect on the measured spectrum Figure 4.S4, and the relatively stronger gating effect in device A Figure 4.S3. More details about the COMSOL simulation can be found in the methods section.

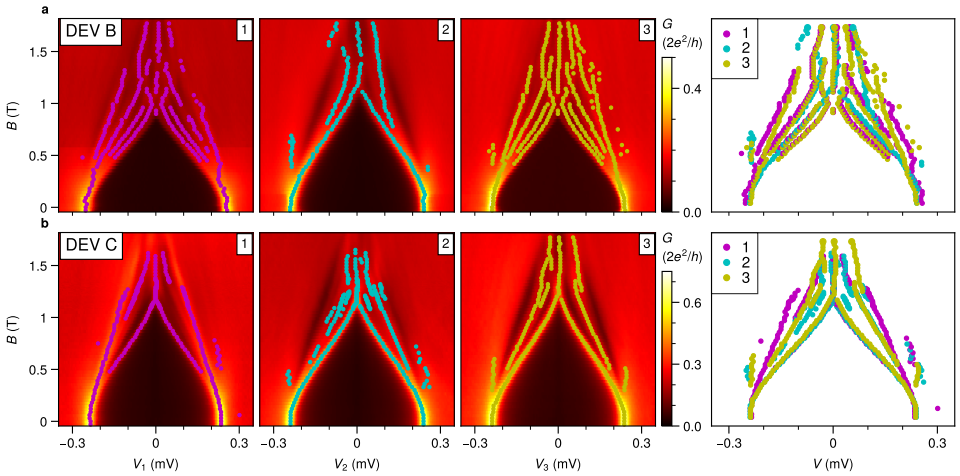

Figure 4.S6: **Identification of subgap states in Figure. 5: Device B and C**. At each field value, we find the local maxima in the tunnelling conductance and overlay these states from different probes in the last plot of each row. For device B (**(a)**,top row), the lowest subgap states of probe 1 and probe 3 show identical dependence on magnetic field, but are absent in the spectra in probe 2. However, the evolution of the second-lowest states of probe 1 and 3 matches well with that of the lowest states of probe 2. For device C(**(b)**,bottom row), the lowest energy subgap states from the three probes show identical dependence.

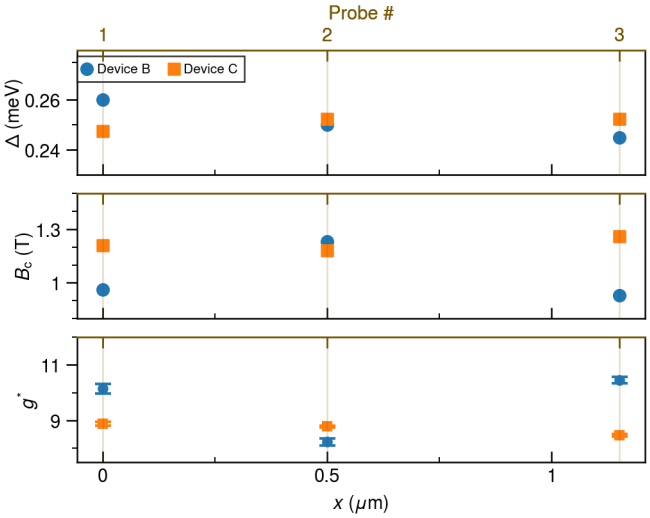

Figure 4.S7: **Spatial dependence of superconducting gap Δ, critical field B_c and effective g-factor g^* of the lowest subgap states: Device B and C.** For device B, the value of B_c and g^* at probe 2 is clearly different from those at probe 1 and 3. For Device C, however, these parameters are nearly identical at various probes.

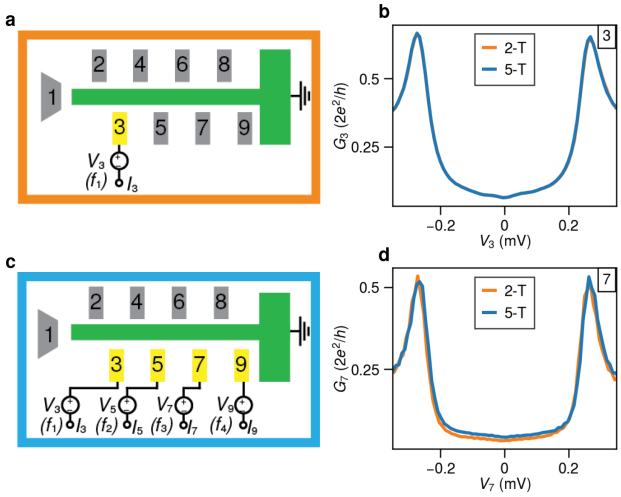

Figure 4.S8: **Comparison of the measured signal with different circuit configurations.** Measurements here are performed either with a two-terminal circuit diagram (with the voltage bias applied to either the probe 3, as shown in **(a)** or the probe 7) or a five-terminal circuit (with voltage biases applied simultaneously to four probes, shown in **(c)**). The measured conductance via two kinds of circuits are then plotted together for probe 3 (**b**) and probe 7 (**d**). There is no significant difference regarding the positions and heights of the coherence peaks between these two measurements, confirming the validity of the five-terminal circuit configuration for investigating the subgap states.

5

Triplet correlations in Cooper pair splitters realized in a two-dimensional electron gas

Qingzhen Wang†, Sebastiaan L. D. ten Haaf†, Ivan Kulesh, Di Xiao, Candice Thomas, Michael J. Manfra and Srijit Goswami

Cooper pairs occupy the ground state of superconductors and are typically composed of maximally entangled electrons with opposite spin. In order to study the spin and entanglement properties of these electrons, one must separate them spatially via a process known as Cooper pair splitting (CPS). Here we provide the first demonstration of CPS in a semiconductor two-dimensional electron gas (2DEG). By coupling two quantum dots to a superconductor-semiconductor hybrid region we achieve efficient Cooper pair splitting, and clearly distinguish it from other local and non-local processes. When the spin degeneracy of the dots is lifted, they can be operated as spin-filters to obtain information about the spin of the electrons forming the Cooper pair. Not only do we observe a near perfect splitting of Cooper pairs into opposite-spin electrons (i.e. conventional singlet pairing), but also into equal-spin electrons, thus achieving triplet correlations between the quantum dots. Importantly, the exceptionally large spin-orbit interaction in our 2DEGs results in a strong triplet component, comparable in amplitude to the singlet pairing. The demonstration of CPS in a scalable and flexible platform provides a credible route to study on-chip entanglement and topological superconductivity in the form of artificial Kitaev chains.

The work has been published in *Nature Communications*, 14, 4876 (2023).
†These authors contributed equally to this work.

5.1 Introduction

Coupling two normal leads to a superconductor can give rise to non-local transport processes directly involving both leads. Two opposite-spin electrons from a Cooper pair in the superconductor can be split into the leads via a process known as Cooper pair splitting (CPS). The dominant transport mechanism that gives rise to CPS is crossed Andreev reflection (CAR), whereby a higher order process allows two electrons to be injected simultaneously into the superconductor to form a Cooper pair. Additionally, a single electron can tunnel through the superconductor from one lead to the other through a process known as elastic co-tunnelling (ECT). The ability to control these processes has important implications for two distinct fields. Firstly, efficient CPS can be used to generate spatially separated entangled electrons, that can be used to perform a Bell test [78–83]. Secondly, in the context of topological superconductivity, it has been shown that CAR and ECT are crucial ingredients required to implement a Kitaev chain [5] using quantum dot-superconductor hybrids [33, 35].

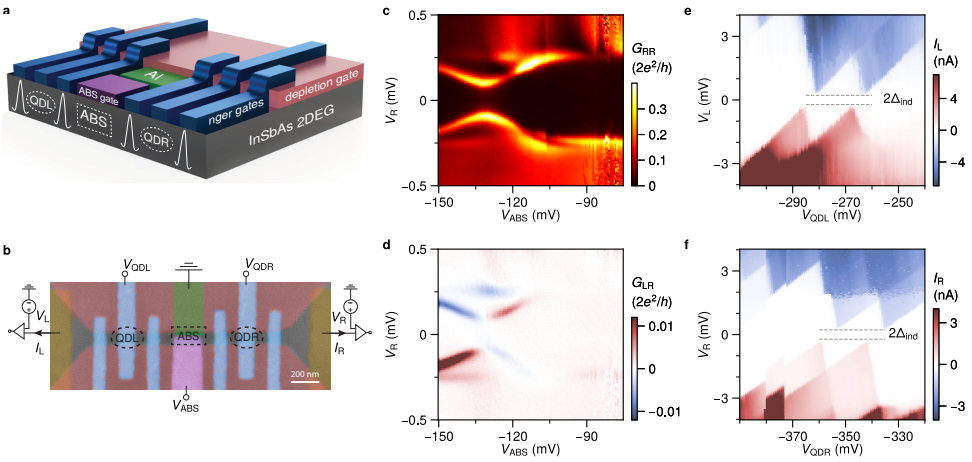

Figure 5.1: **Basic device characterization. (a)** A 3D illustration of the device. The two quantum dots (QDL and QDR), and the region hosting ABSs are indicated. For clarity, the gate-dielectric layers are not shown. **(b)** False-color scanning electron micrograph of Device 1, including a schematic of the circuit diagram for three-terminal measurements. Tunneling spectroscopy measurements showing **(c)** local conductance G_{RR} and **(d)** non-local conductance G_{LR} as a function of the ABS gate voltage V_{ABS} and right bias voltage V_R. Coulomb diamonds of the QDs are measured for **(e)** QDL and **(f)** QDR.

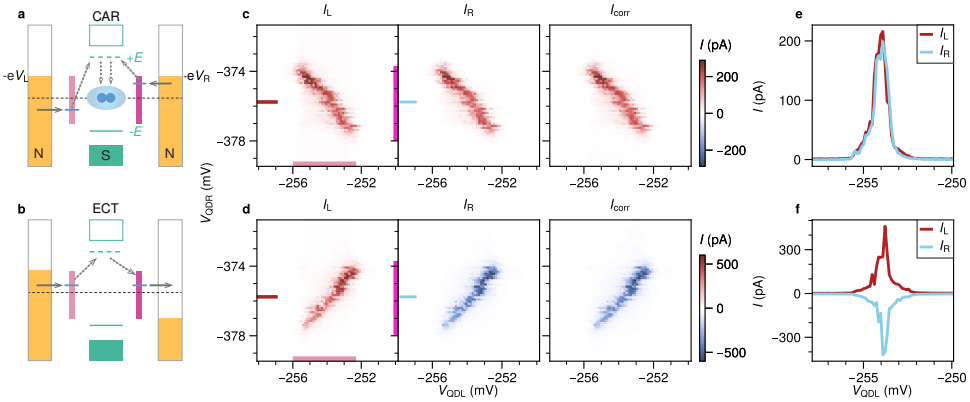

Figure 5.2: **Correlated CAR and ECT signals.** Diagrams of the transport cycles for **(a)** CAR and **(b)** ECT. Blue lines indicate the energies of the QD levels required for transport via the ABS at energy $\pm E$. Purple bars mark the energy window in which transport is allowed, corresponding to the marked regions in the measurement panels (**c** and **d**). **(c)** Charge stability measurement of QDL and QDR with $V_L = V_R = -120\,\mu V$ taken at $V_{ABS} = -245\,mV$. Equal currents with the same sign are observed at the left (I_L) and right (I_R) leads only when the QD energy levels are anti-aligned, as expected for CAR. **(d)** Repeated measurement, but with $V_L = -V_R = -120\,\mu V$. Equal currents with opposite sign are observed only when the QDs are aligned in energy, as expected for ECT. The correlated currents I_{corr} are calculated from I_L and I_R as described in the main text. Exemplary line traces at $V_{QDR} = -375\,mV$ for CAR and ECT are plotted in **(e)** and **(f)** respectively.

5.2 Results

5.2.1 Device and characterization

Devices are fabricated on an InSbAs 2DEG with epitaxial aluminum grown by molecular beam epitaxy. This material has been established to have a low effective mass, high g-factor and large spin-orbit coupling [29, 41]. Fig. Figure 5.1a,b illustrate the device structure together with the three-terminal measurement circuit. The two depletion gates (pink) define a quasi-1D channel of about 150 nm, contacted on each side with normal leads. The middle of the channel is proximitized via a 150 nm-wide aluminium strip (green), which is kept electrically grounded. Quantum dots on the left and right are created using the finger gates (blue) and the ABS energy is controlled by the central ABS gate (purple). The biases V_L and V_R applied to the left and right leads can be varied independently. The currents I_L and I_R in the left and right leads are measured simultaneously. We define a positive current as the flow of electron charge from the leads to the superconductor.

First, the two innermost finger gates are used to define tunneling barriers on either side of the hybrid region. Fig. Figure 5.1c,d show the measured local conductance $G_{RR} = \frac{dI_R}{dV_R}$ and non-local conductance $G_{LR} = \frac{dI_L}{dV_R}$ as a function of the ABS gate voltage V_{ABS}. The induced gap in the hybrid section is found to be

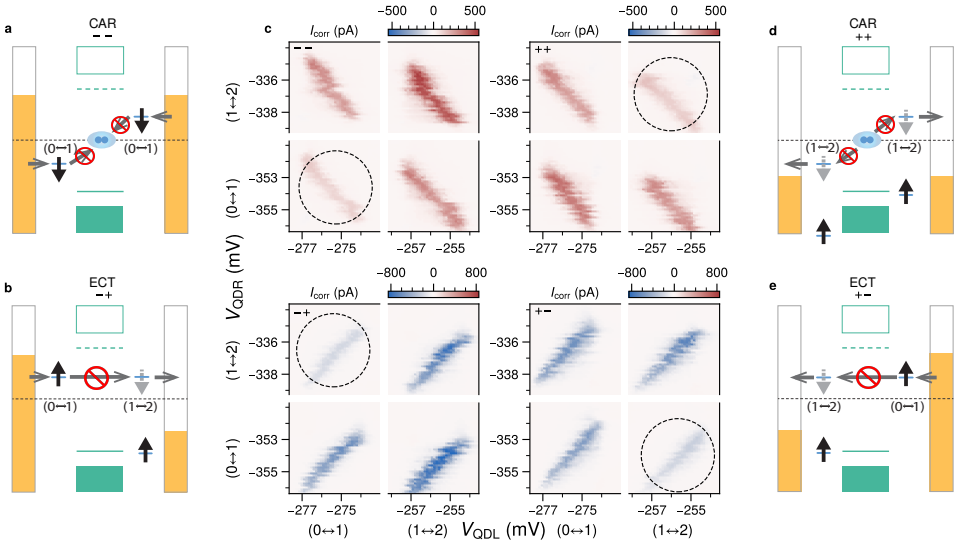

Figure 5.3: **Spin blockade at zero magnetic field.** Charge stability diagrams are obtained for all four bias polarity combinations, to measure either CAR ($V_L = V_R$) or ECT ($V_L = -V_R$). **(a),(b),(d)** and **(e)** show energy diagrams illustrating situations expected to lead to transport blockades. Arrows within the dots either represent an already occupied spin state (black), or a state available to be occupied by an incoming electron (grey). **(c)** The corresponding measurements of I_{corr} plotted against V_{QDL} and V_{QDR}, with applied biases $|V_L| = |V_R| = 120\,\mu V$ and $V_{ABS} = -220\,mV$. The used bias polarity for each set of measurements is noted in the top left corner. For each bias configuration a specific transition is suppressed (dashed circles) as a consequence of the blockade depicted alongside the measurement. Gate voltage ranges are interrupted to zoom-in on the relevant ECT and CAR features.

$\Delta_{ind} \approx 220\,\mu eV$. The correspondence between G_{RR} and G_{LR} shows the presence of an extended discrete ABS in the proximitized section. The observed sign-switching in the non-local signal is typical for an extended ABS probed in a three-terminal measurement [68, 84, 85]. Next, two quantum dots are created on either side of the proximitized section. Their electro-chemical potentials are controlled by applied voltages V_{QDL} and V_{QDR}. The charge stability diagrams of both QDs (Figure 5.1e,f) show Coulomb diamonds with clear even-odd spacing. The pair of Coulomb peaks show linear splitting as a function of magnetic field, indicative of a spin-degenerate single orbital level (Fig. S1). The superconducting gap Δ_{ind} is clearly visible at the charge degeneracy points, indicative of a weak coupling to the proximitized region [86, 87]. Charging energies of QDL and QDR are 1.9 meV and 1.4 meV respectively, much larger than the induced superconducting gap.

5.2.2 CAR and ECT

For CAR, an electron from each of the two leads is simultaneously transferred to the superconductor via an extended ABS to form a Cooper pair (Figure 5.2a). This should therefore result in positively correlated currents in the leads ($I_L = I_R$). For ECT (Figure 5.2b), an electron from the left or right lead tunnels to the opposite lead via the hybrid section, which should thus give rise to negatively correlated currents ($I_L = -I_R$). As we will show below, by controlling the QD levels and voltage biases, it is possible to distinguish currents arising from ECT and CAR. Such measurements are shown in Figure 5.2c,d. Here V_{QDL} and V_{QDR} are each tuned close to a selected charge degeneracy point and the currents I_L and I_R are simultaneously measured. The large charging energies of the dots ensure that each lead strongly prefers accepting or donating a single electron. We further ensure that the applied biases are lower in energy than any sub-gap states in the hybridized region, such that local transport is suppressed. To demonstrate CAR, we set $V_L = V_R = -120\,\mu V$ and sweep V_{QDL} and V_{QDR}. A finite current is observed only along a line with negative slope, for both I_L and I_R (Figure 5.2c). Furthermore, the currents are equal both in magnitude and sign (Figure 5.2e). Converting the gate voltages to electro-chemical potentials (μ_L, μ_R), we confirm that CAR mediated transport occurs when $\mu_L = -\mu_R$ (Fig. S4c). This is consistent with the requirement that the energies of the electrons forming the Cooper pair must be equal and opposite. To demonstrate ECT, we apply biases with opposite polarity ($V_L = -V_R = -120\,\mu V$). Unlike CAR, a finite current is observed only along a line with positive slope (Figure 5.2d). This is consistent with energy conservation during ECT, which demands that $\mu_L = \mu_R$. Furthermore, the currents are now equal in magnitude, but opposite in sign (Figure 5.2f). Note that when biasing only V_L or V_R and grounding the other lead, both ECT and CAR become visible in the charge stability diagram (Fig. S2).

Importantly, for both CAR and ECT we observe no notable current when the bias and energy conditions are not met, indicating that unwanted local processes are strongly suppressed. In combination with strongly correlated currents, this suggests a relatively large signal-to-noise ratio of the CPS process. To characterize this, we calculate the CPS efficiency and visibility (Fig. S4). Following[88, 89], we obtain a combined CPS efficiency above 90 %, on par with the highest previously reported values [88, 89]. Applying a larger bias that exceeds the sub-gap state energy (but is still below Δ_{ind}) results in additional local, non-correlated signals which only depend on a single QD (Fig. S3) and significantly reduce the CPS efficiency.

To systematically characterize the CAR and ECT measurements, we calculate the correlated current $I_{corr} \equiv \mathrm{sgn}(I_L I_R) \cdot \sqrt{|I_L||I_R|}$ (Figure 5.2c,d)[89]. It is non-zero only when I_L and I_R are both non-zero and thus highlights features mediated by ECT and CAR. Furthermore the sign of I_{corr} clearly distinguishes CAR (always

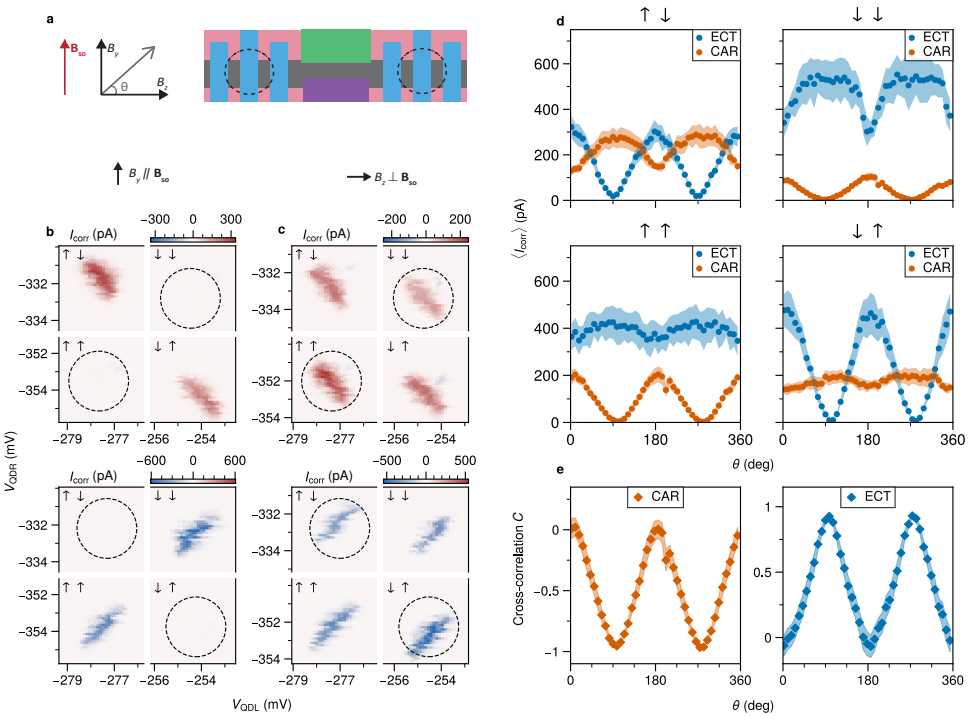

Figure 5.4: **CAR and ECT at finite magnetic field**. **(a)** A schematic showing the coordinate system of the applied magnetic field with respect to the device. **(b)** Measurement of I_{corr} for CAR (top) and ECT (bottom) with $\mathbf{B} \parallel B_y = 150\,\mathrm{mT}$ and $V_{ABS} = -220\,\mathrm{mV}$. Lower biases ($|V_L|, |V_R| = 70\,\mu\mathrm{V}$) are applied to keep the bias window below any sub-gap states, whose energies are pulled down by the finite magnetic field (Fig. S1). Equal-spin CAR and opposite-spin ECT are fully suppressed (circled). **(c)** Measurement of I_{corr} with $\mathbf{B} \parallel B_z = 150\,\mathrm{mT}$. The blockades in **(b)** have been clearly lifted. **(d)** Angle-dependence of $\langle I_{corr} \rangle$ for the different spin channels for a full rotation of the magnetic field in the y-z plane. The (−,+) and (+,+) bias configurations are used for ECT and CAR respectively. Each data point represents a single charge stability diagram for a specific spin channel. The data extraction procedure is described in Fig. S7. **(e)** The calculated spin cross-correlation (as defined in the text) of CAR and ECT, derived from (**d**).

positive) from ECT (always negative).

5.2.3 Zero field spin blockade

In the absence of a magnetic field, the orbital levels of the QDs are spin-degenerate. Therefore, if the dot has an even number of electrons, the first electron to occupy the next orbital (a transition denoted as $0 \leftrightarrow 1$) can be either spin-up or spin-down. However, to add the second electron ($1 \leftrightarrow 2$), the Pauli exclusion principle requires it to have an opposite spin. The effect of this spin-filling rule leads to a blockade of transport, which depends on the nature of the underlying process.

We first focus on ECT in the (−,+) bias configuration, denoting that a negative bias is applied to the left lead and a positive bias is applied to the right lead (Figure 5.3b). When the QDs are tuned to the (0 ↔ 1, 1 ↔ 2) transition, a situation can arise where the left QD is occupied with e.g. a spin-up electron (coming from the left lead), whereas the right QD can only accept a spin-down electron (since the spin-up state has already been occupied). At this point transport from left to right is blocked, analogous to the well-known Pauli blockade in double quantum dots [90]. This spin blockade is clearly seen when the QDs are tuned over successive charge transitions. In Figure 5.3c we see that the ECT current is suppressed for the (0 ↔ 1, 1 ↔ 2) transition. Reversing the bias polarities to (+,−), a similar blockade is observed for the (1 ↔ 2, 0 ↔ 1) transition, as expected (see Figure 5.3e).

In the (−,−) configuration, only CAR mediated transport can occur and we find a suppression in CAR current for the (0 ↔ 1, 0 ↔ 1) transition. This is a direct consequence of the Cooper pairs in an s-wave superconductor having a singlet pairing. Thus, for transport to occur, each QD must donate an electron of *opposite* spin in order to create a singlet Cooper pair in the superconductor. Transport is therefore blocked when both dots are occupied by electrons with the same spin (Figure 5.3a). Finally, in the (+,+) configuration a blockade is expected for the (1 ↔ 2, 1 ↔ 2) transition (Figure 5.3d), as observed in the measurements. Qualitatively similar measurements of spin blockade for CAR and ECT are presented for another device (Fig. S8). We note that a finite amount of current remains for each blockaded transition, indicating the presence of a spin-relaxation mechanism in our system. The hyperfine interaction is one such mechanism that can lift the Pauli blockade [91, 92]. We confirm this by applying a magnetic field to suppress the spin-mixing due to the hyperfine interaction, and find that 35 mT is sufficient to fully suppress the remaining current (Fig. S5).

5.2.4 Singlet and triplet ECT/CAR

The spin degeneracy of the QD levels is lifted by applying a magnetic field, allowing us to operate them as spin-filters (Fig. S1). When the Zeeman splitting exceeds $|eV_L|, |eV_R|$, only spin-up (↑) electrons are involved in transport at a (0 ↔ 1) transition and only spin-down (↓) at a (1 ↔ 2) transition. In the absence of spin-orbit coupling, CAR is only expected to occur when both QDs are tuned to host electrons with opposite spin. The opposite applies to ECT, where a current is only expected when the QDs are tuned to receive electrons with equal spin.

As shown in Figure 5.4b, when an in-plane field of 150 mT is applied along B_y (i.e. perpendicular to the channel), CAR current is only present in the quadrants where the electrons have opposite spins (↑↓ and ↓↑) and completely suppressed for the equal-spin (↑↑ and ↓↓) configuration. Similarly, no current is detected for opposite-spin ECT, while transport is allowed for equal-spin ECT. This spin-

dependent transport indicates that the direction of the spin-orbit field $\mathbf{B}_{SO}$ is along B_y, making spin a good quantum number. This is also consistent with the expected Rashba spin-orbit interaction in a quasi-1D channel with momentum along the z-direction and electric field perpendicular to the 2DEG plane. Applying the magnetic field perpendicular to $\mathbf{B}_{SO}$ (i.e. along B_z), a spin-up electron may acquire a finite spin-down component, due to the spin-orbit interaction. The consequence of this can be seen in Figure 5.4c, where we now observe sizeable currents for equal-spin CAR and opposite-spin ECT. The full evolution of the spin-specific ECT and CAR currents can be obtained by performing an in-plane rotation of the magnetic field (Figure 5.4d). The averaged amplitudes of equal-spin CAR and opposite-spin ECT currents $\langle I_{corr} \rangle$ are found to oscillate smoothly between full suppression at $\theta \approx 90^\circ$ and 270° ($\mathbf{B} \parallel \mathbf{B}_{SO}$), and their maximum strength at $\theta \approx 0^\circ$ and 180° ($\mathbf{B} \perp \mathbf{B}_{SO}$). This result does not depend on a specific choice of orbitals in the QDs (Fig. S6).

The ability to accurately resolve the spin of the electrons in CPS is particularly relevant in the context of entanglement witnessing. An important metric capturing this, is the spin cross-correlation [80, 81]. As described in [93], we calculate the spin cross-correlation from the measured currents as:

$$C = \frac{(I^{\uparrow\uparrow} + I^{\downarrow\downarrow} - I^{\uparrow\downarrow} - I^{\downarrow\uparrow})}{(I^{\uparrow\uparrow} + I^{\downarrow\downarrow} + I^{\uparrow\downarrow} + I^{\downarrow\uparrow})} \tag{5.1}$$

and plot it for both CAR and ECT as a function of θ (Figure 5.4e). I^{ij} corresponds to the average correlated current $\langle I_{corr} \rangle$ associated with each spin configuration, where $i, j \in \{\uparrow, \downarrow\}$. $C = \pm 1$ when there is a perfect correlation or anti-correlation between the spins of electrons entering the QDs. In contrast, $C = 0$ when the probabilities of equal-spin and opposite-spin transport become equal. When $\mathbf{B} \parallel \mathbf{B}_{SO}$ we obtain a value of $C = -0.96$ for CAR, demonstrating a nearly perfect singlet pairing between the QDs. Similarly, for ECT $C = +0.93$ is obtained. When $\mathbf{B} \perp \mathbf{B}_{SO}$, C reaches close to 0 for both CAR and ECT, stressing that the triplet component can be tuned to be of similar magnitude to the conventional singlet pairing.

5.3 Conclusion

In conclusion, we have used quantum dot-superconductor hybrids to demonstrate highly efficient Cooper pair splitting in a two-dimensional semiconductor platform. Using spin-polarized quantum dots, we performed spin-selective measurements of ECT and CAR and showed that the strong spin-orbit interaction in ternary 2DEGs results in comparable strengths of singlet and triplet correlations between the quantum dots. Finally, through magnetic field rotations, we showed that it is possible to obtain equal amplitudes of ECT and CAR, establishing 2DEGs as an ideal platform to study Majorana bound states in artificial Kitaev chains.

5.4 Discussion

The demonstration of singlet and triplet correlations with Cooper pair splitters in 2DEGs paves the way for more advanced experiments to study entanglement and topological superconductivity. An interesting open question relates to the underlying mechanism that allows for strong triplet CAR in these devices. One possibility is for two equal-spin electrons to form a normal s-wave Cooper pair, due to spin precession in the tunnel barriers. Another path is that an induced p-wave superconducting pairing arises in the hybrid section, such that two equal-spin electrons form a Cooper pair. In order to distinguish these possibilities, we propose to create quasi-1D channels that are bent (rather than straight), resulting in different spin-orbit directions in each arm of the Cooper pair splitter[80, 94]. Such devices are easily implemented in 2DEGs where any arbitrary shape of the channel can be realized simply by altering the design of the depletion gates. Given the high fidelity spin correlation we have demonstrated here, such devices could also be used to detect entanglement by performing a Bell test with electrons from a Cooper pair [80].

Finally, the recent realization of a minimal Kitaev chain [50] opens up several possibilities to systematically study Majorana bound states (MBSs). In this regard the 2DEG platform is again particularly suitable. It readily allows for extending these measurements to multi-site QD chains, whereby the flexibility of the 2DEG would allow for the simultaneous measurement of density of states at the edges and in the bulk. Furthermore, one could use these chains to perform tests of non-Abelian exchange statistics via braiding experiments [36, 95], which necessarily require a 2D platform.

Data availability and Code Availability Raw data and analysis scripts for all presented figures are available at https://doi.org/10.5281/zenodo.7311374.

5.5 Supplementary information

5.5.1 Fabrication

Device 1 (main text) and Device 2 (supplementary) were fabricated using techniques described in detail in [96]. A narrow aluminum strip is defined in an InSbAs-Al chip by wet etching, followed by the deposition of two normal Ti/Pd contacts. After deposition of 20 nm AlOx via atomic layer deposition (ALD), the two depletion gates are evaporated. Following a second ALD (20 nm AlOx) Ti/Au gates are evaporated in order to define the QDs and tune the ABS energy.

5.5.2 Measurements

All measurements are performed in a dilution refrigerator with a base temperature of 20 mK. Magnetic fields are applied using a 3D vector magnet. The alignment of the magnetic field with respect to the device is expected to be accurate within $\pm 5^{\circ}$. Transport measurements are performed in DC using a three-terminal set-up, where the aluminum is electrically grounded (Figure 5.1b). Current amplifier offsets are determined by the average measured current when both dots are in Coulomb blockade. CAR and ECT processes can be observed over a wide range of V_{ABS} voltages. Once a V_{ABS} setting was found with both strong CAR and ECT currents, it was kept at a constant value throughout the rest of the measurements. Further care was taken to implement the same orbitals in both QDs for all presented measurements in the main text. The mismatch between exact V_{QDR} and V_{QDL} values at which ECT and CAR are observed is due to gate instabilities, causing a drift of charge degeneracy points over a period of time. Therefore, the field rotation measurement in Figure 5.4e was performed multiple times. No quantitative difference was observed between measurements. Presented data was selected due to high stability of the QDs over the course of the measurements.

Overall, we have measured four fully functional devices at the time of writing this manuscript, all of which have produced highly efficient CAR and ECT mediated by extended ABSs. For three of these devices we have performed magnetic field rotations and observed angle-dependent oscillations of ECT and CAR currents.

5.5.3 Supplementary Figures S1 to S10

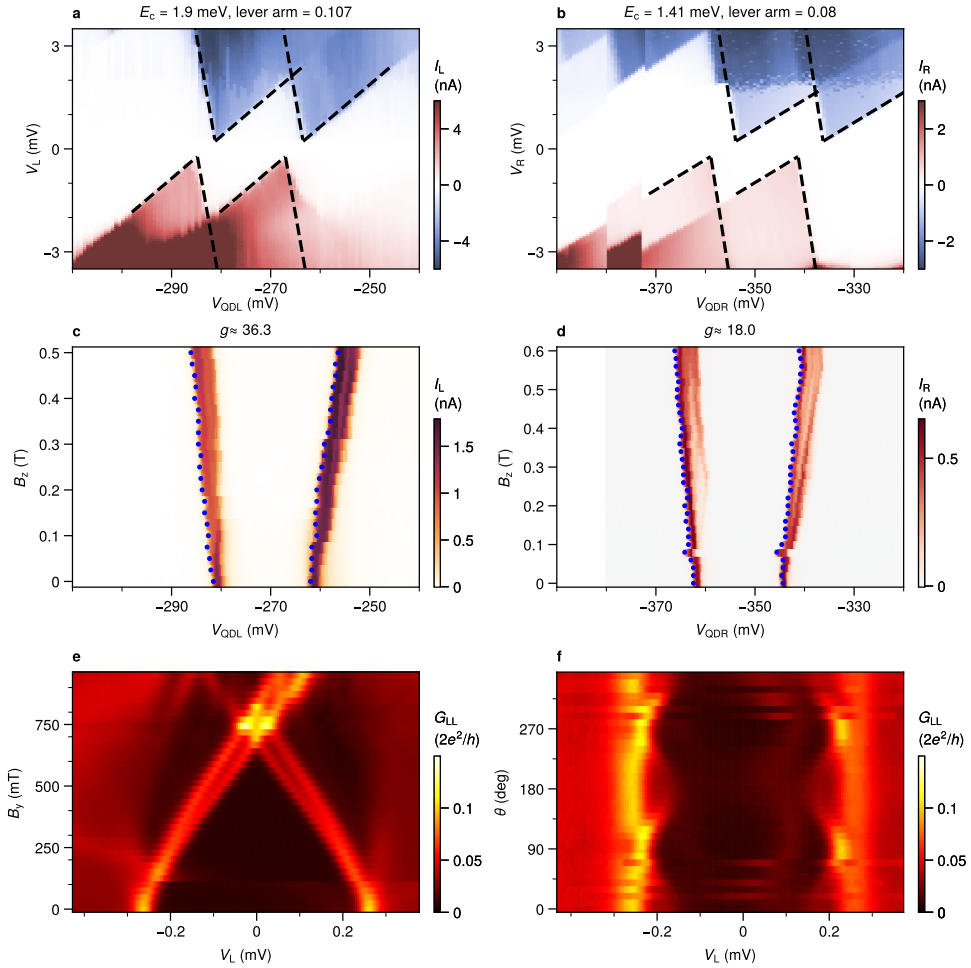

Figure 5.S1: **Quantum dot and ABS characterization.** Extraction of charging energy E_c and lever arm for (**a**) QDL and (**b**) QDR from Coulomb diamonds shown in Fig 1 of the main text. Evolution of Coulomb peaks with B_z for (**c**) QDL and (**d**) QDR shows Zeeman splitting causing the separation between the resonances to increase. Bias voltages are $(V_L, V_R) = (-450\,\mu V, 0)$ for the left measurement, and $(0, -350\,\mu V)$ for the right measurement. g-factors of -36 and -18 are derived for the QDL and QDR respectively. **(e)** Measured local conductance G_{LL} of the hybrid section with increasing magnetic field $B \parallel B_y$ at $V_{ABS} = -245$ mV. **(f)** Field rotation in the y-z plane with a fiedld magnitude of 100 mT, showing a slight anisotropy of the ABS energy.

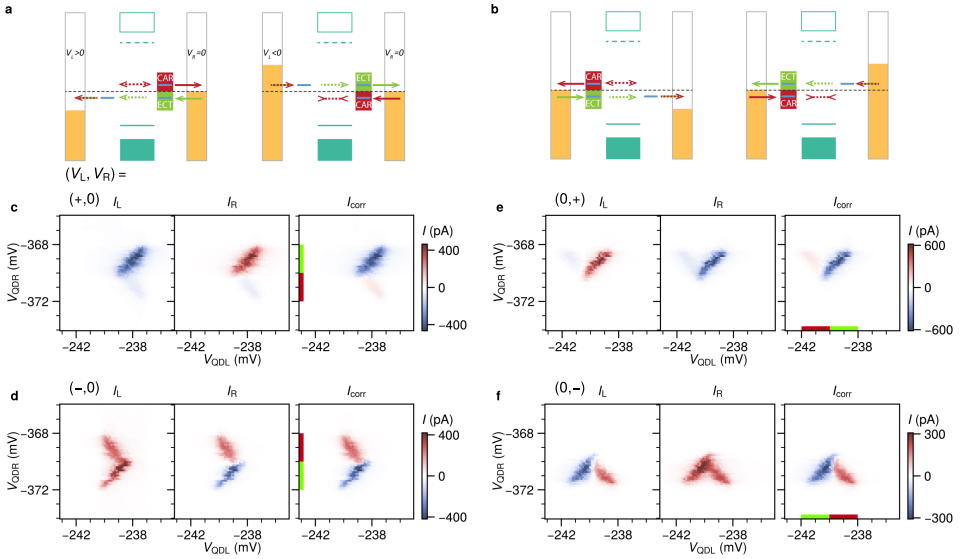

Figure 5.S2: **Simultaneous measurement of ECT and CAR**. Energy diagrams for the expected transport when biasing only the **(a)** left or **(b)** right side of the device. **(c)-(f)** Corresponding measurements with the bias polarities labelled in the top left corners. Two distinct features with opposite slope appear in each charge stability diagram. This is because both ECT and CAR can now occur, depending on the position of the QD levels with respect to the grounded side. Red (CAR) and green (ECT) bars indicate the corresponding gate voltage ranges in which each process is allowed.

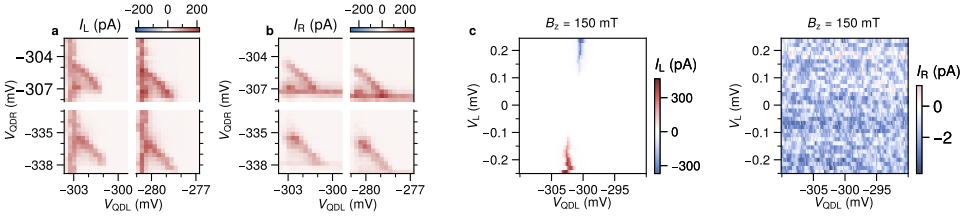

Figure 5.S3: **Filtering local transport processes.** A key requirement for isolating CAR and ECT is the ability to filter out local processes. For the measurements presented in the main text it was ensured that the applied biases remained below the energy of any subgap states. With applied biases of -120 µV on both sides and an external magnetic field $B_z = 150$ mT, additional currents appear in **(a)** I_L and **(b)** I_R on top of the currents arising through CAR. Fixing V_{QDR} at -320 mV (i.e., putting the right dot off-resonance), I_L and I_R are measured as a function of the left bias V_L and left plunger gate V_{QDL}. **(c)** Current arising through local processes appears once the applied bias exceeds the ABS energy. No current is detected in I_R.

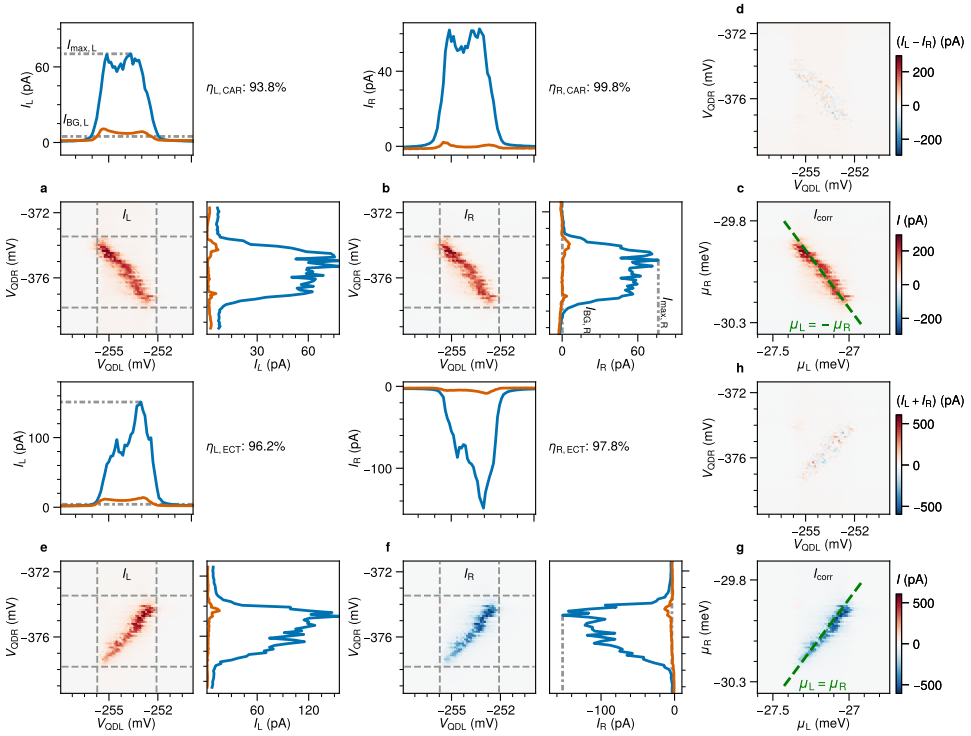

Figure 5.S4: **Cooper pair splitting efficiency.** Analysis of the data presented in Fig. 2. **(a,b)** Measured currents I_L and I_R arising from CAR. The top panel shows I_L averaged over the V_{QDR} range indicated by the horizontal grey lines (blue) and the background trace averaged outside the horizontal grey lines (orange). The right panel shows I_L averaged over the V_{QDL} range indicated by the vertical grey lines and the background trace averaged outside the vertical grey lines. The efficiency of each junction is defined as $\eta_j = 1 - \frac{I_{BG,j}}{I_{max,j}}$ where the $I_{BG,j}$ is the average value of the background trace and $I_{max,j}$ is the maximum of the averaged I_j. We extract an η of about 94% for the left junction and 99% for the right junction. Taking the product this gives a combined efficiency of $\eta_L \eta_R$ of about 93%. Using the lever arms extracted from the Coulomb diamonds (Fig. S1), the correlated current I_{corr} is plotted as a function of μ_L and μ_R in **(c)**. The dashed line corresponds to $\mu_L = -\mu_R$, confirming that transport occurs when the dot levels are anti-aligned. Calculating $I_L - I_R$ shows very small remaining current, verifying $I_L = I_R$ **(d)**. **(e,f)** Similar analysis of I_L, I_R and averaged currents for ECT. The combined efficiency is again found to be about 93%. **(g)** I_{corr} in μ_L- μ_R space, together with the line where $\mu_L = \mu_R$, showing that transport takes place when the QD levels are aligned. **(h)** Plotting I_L + I_R shows again that little signal remains, highlighting that $I_L = -I_R$ for ECT.

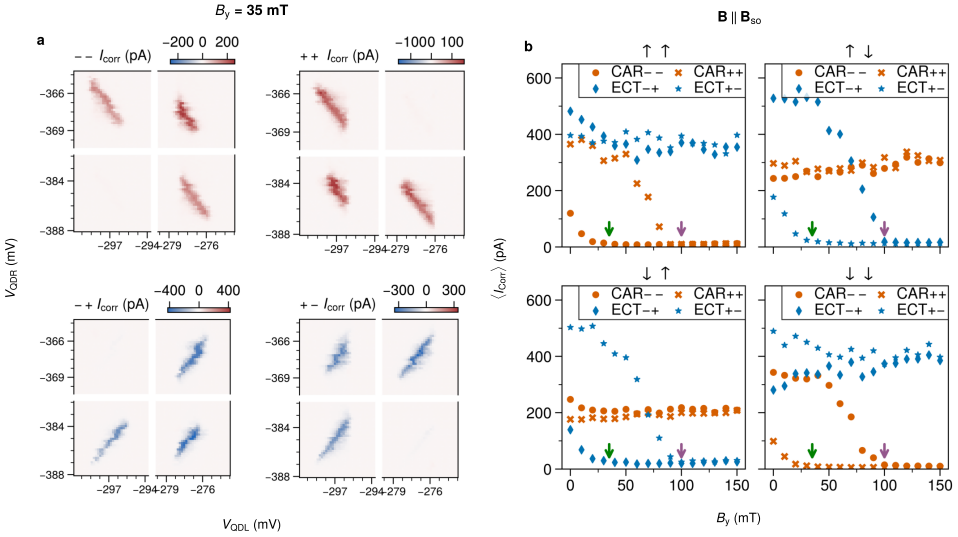

Figure 5.S5: **Field evolution of ECT and CAR. (a)** The charge stability diagrams at B_y = 35 mT, of the same resonances used in the main text, show that the weakened transitions in each bias configuration (circled in Fig. 2c) are now completely blocked. This is interpreted as a result of the magnetic field overcoming the hyperfine interaction in the QDs. **(b)** Spin-filtered measurements of $\langle I_{corr} \rangle$ for ECT and CAR as a function of magnetic field $B_y \parallel \mathbf{B}_{SO}$, for each bias configuration. Two transitions are present in each quadrant. Above roughly 35 mT (green arrows) the Pauli-blockaded process in each quadrant becomes fully suppressed. Above 100 mT (purple arrows) the Zeeman splitting exceeds the applied biases (|100 μV|) such that only the spin-preserving processes remain (i.e. opposite-spin CAR and equal-spin ECT).

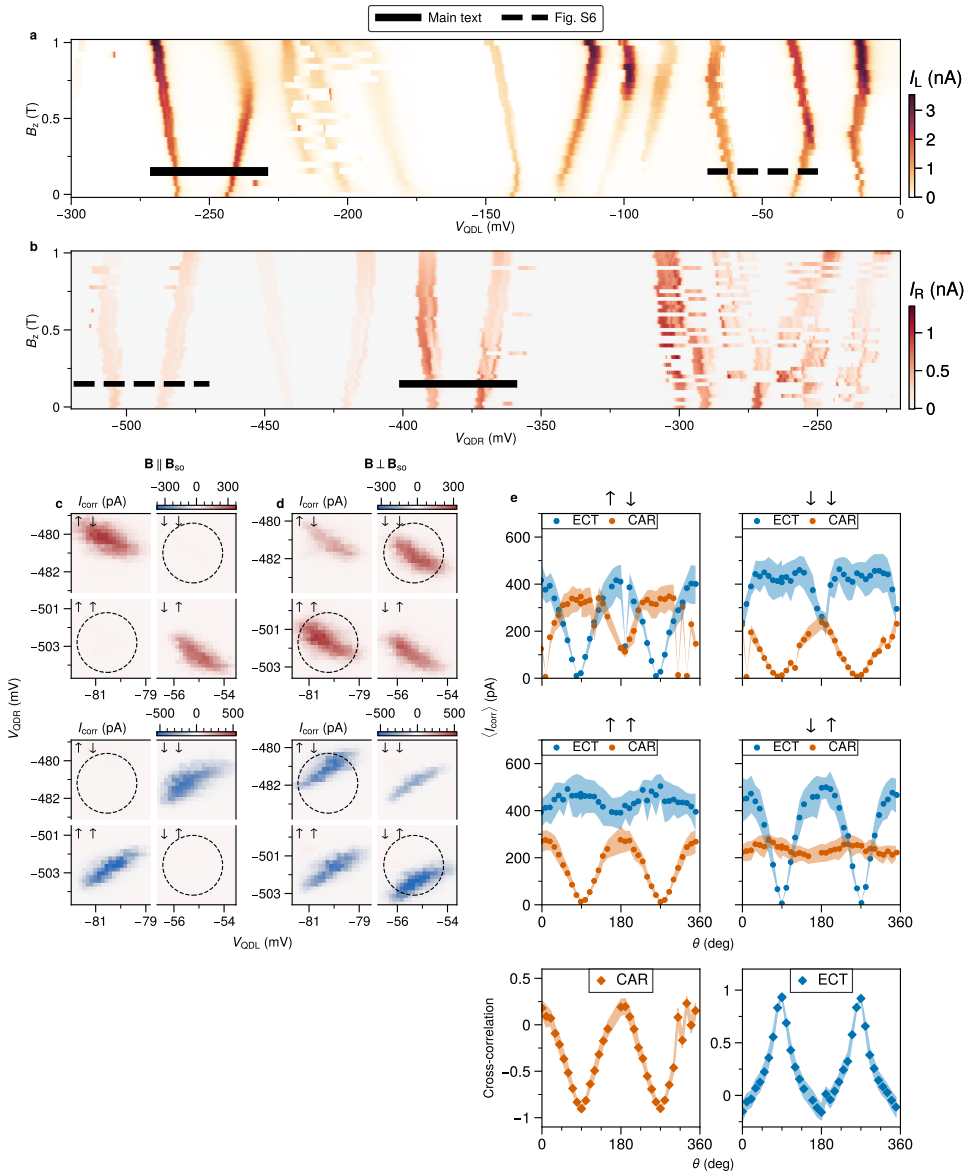

Figure 5.S6: **Field angle dependence with another pair of QD resonances. (a,b)** Field evolution of Coulomb resonances in the QDs over an extended range of V_{QDL} and V_{QDR}. The effect of Zeeman splitting is observed for multiple orbitals in each QD. Solid black lines indicate the orbitals used in the main text, while the dashed lines indicate different orbitals used for data presented here. **(c,d)** Repetition of measurements presented in Fig. 4(c,d) for the second pair of resonances. Unconventional processes (equal-spin CAR and opposite-spin ECT) are fully suppressed at $B \parallel B_{SO}$ and recovered at $B \perp B_{SO}$. A full field rotation **(e)** yields similar behaviours of $\langle I_{corr} \rangle$ and cross-correlation to the dependence shown in Fig. 4f.

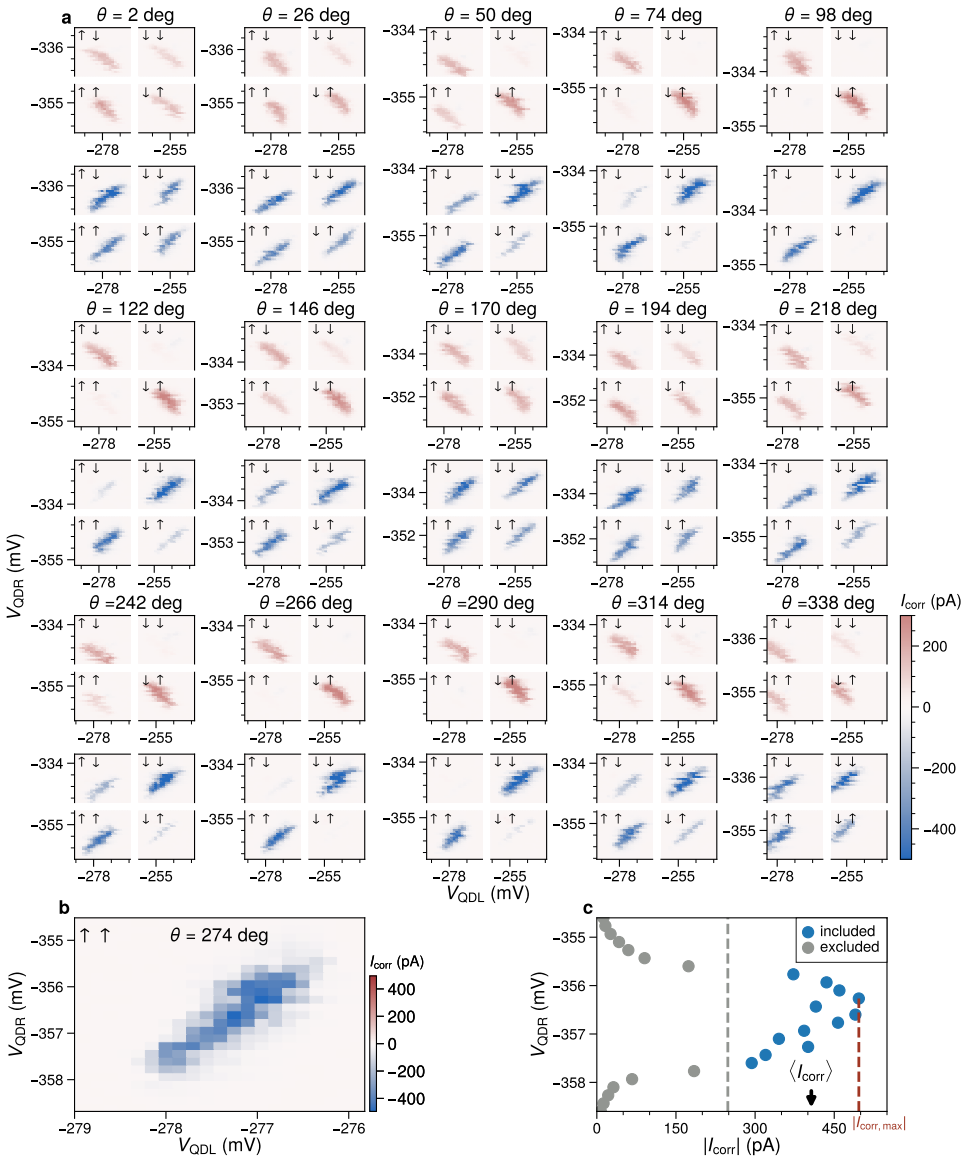

Figure 5.S7: **Raw data from Fig 4f and data extraction. (a)** Selection of raw data used for extracting the field angle dependence of CAR and ECT rates presented in Fig. 4f. For each angle the four quadrants with different spin configurations of I_{corr} are plotted for CAR (top panels) and ECT (bottom panels). A single quadrant is converted to a single data point to quantify the spin-selective rate of CAR and ECT at a specific angle of the magnetic field. The data extraction process is detailed in panel **(c)** for the measurement of ↑↑-ECT at $\theta = 274^{\circ}$ (plotted again in **(b)**). The maximum value of $|I_{\mathrm{corr}}|$ for each horizontal line-cut is extracted and plotted as a function of V_{QDR}. To exclude data at the edge of the bias window, a threshold is set at half of the maximally recorded $|I_{\mathrm{corr,max}}|$. The included values are labeled in blue, from which the average $\langle I_{\mathrm{corr}} \rangle$ and standard deviation is derived.

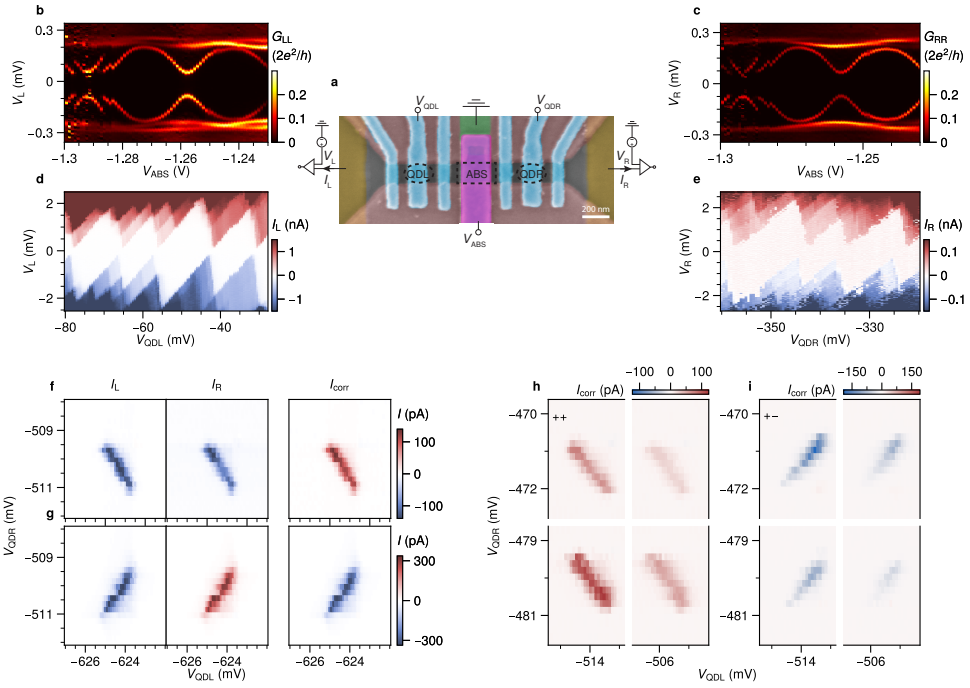

Figure 5.S8: **Measurements on additional device (Device 2). (a)** False-color scanning electron micrograph of Device 2, with the circuit diagram used for three-terminal measurements. Scale bar is 200 nm. The distance between the centers of the QDs is about 800 nm (in contrast to 600 nm for Device 1 presented in the main text). Tunneling spectroscopy measurements of the **(b)** local conductance G_{LL} and **(c)** G_{RR} as a function of V_{ABS} show correlated states, indicating the presence of an extended ABSs. Measured Coulomb diamonds for **(d)** QDL and **(e)** QDR. The extracted charging energy is about 1.2 meV for both dots. **(f)**,**(g)** Similar to Fig. 2, measured left current I_L, right current I_R and the calculated correlated current I_{corr}, for CAR ($V_L = V_R = 100\,\mu V$) and ECT ($V_L = 100\,\mu V$ and $V_R = -100\,\mu V$). Measurements over successive charge transitions reveal the expected spin blockade for **(h)** CAR (+,+) and **(i)** ECT (+,−) at zero magnetic field.

6

A two-site Kitaev chain in a two-dimensional electron gas

Sebastiaan L. D. ten Haaf†, **Qingzhen Wang**†, A. Mert Bozkurt, Chun-Xiao Liu, Ivan Kulesh, Philip Kim, Di Xiao, Candice Thomas, Michael J. Manfra Tom Dvir, Michael Wimmer and Srijit Goswami

Artificial Kitaev chains can be used to engineer Majorana bound states (MBSs) in superconductor-semiconductor hybrids [33, 35, 50, 97]. In this work, we realize a two-site Kitaev chain in a two-dimensional electron gas by coupling two quantum dots through a region proximitized by a superconductor. We demonstrate systematic control over inter-dot couplings through in-plane rotations of the magnetic field and via electrostatic gating of the proximitized region. This allows us to tune the system to sweet spots in parameter space, where robust correlated zero bias conductance peaks are observed in tunnelling spectroscopy. To study the extent of hybridization between localized MBSs, we probe the evolution of the energy spectrum with magnetic field and estimate the Majorana polarization, an important metric for Majorana-based qubits [98, 99]. The implementation of a Kitaev chain on a scalable and flexible 2D platform provides a realistic path towards more advanced experiments that require manipulation and readout of multiple MBSs.

This work has been published in *Nature* **630**, 329–334 (2024).
†These authors contributed equally to this work.

6.1 Introduction

Superconductor-semiconductor hybrid systems have been intensively investigated as a potential platform to engineer topologically protected Majorana bound states (MBSs). In particular, significant efforts have been dedicated to studying one-dimensional systems coupled to s-wave superconductors [7, 51, 52]. However, uncontrolled microscopic variations in hybrid devices have complicated the study of MBSs [46, 65, 100]. A potential way to mitigate the effects of disorder, is to create a Kitaev chain [5] using an array of quantum dots (QDs) with controllable couplings [33, 35, 97]. In fact, a chain consisting of only two QDs, while not topologically protected, is sufficient to create localized MBSs [33]. These so-called "poor man's Majoranas" have recently been realized in nanowires [50], which has led to proposals [38, 99, 101, 102] to study non-Abelian statistics by fusing or braiding MBSs in multiple two-site chains. However, in order to perform these studies, and move towards a Majorana-based qubit with integrated readout and control, it is vital to have a scalable and flexible 2D architecture.

In this work we realize a two-site Kitaev chain by coupling two spin-polarized QDs in an InSbAs two-dimensional electron gas (2DEG). By tuning the couplings between the QDs to so-called "sweet spots", we demonstrate correlated zero-bias conductance peaks (ZBPs) that are resilient to local perturbations. In addition to electrostatic control, we show that the planar 2DEG geometry allows one to reach such sweet spots through an in-plane rotation of the magnetic field. An important prerequisite to produce localized MBSs, is that the Zeeman splitting in the QDs is sufficiently large [98]. Surprisingly, however, we find that several features used to identify "sweet spots" (such as correlated ZBPs) actually persist down to zero magnetic field. We show that the evolution of the energy spectrum with magnetic field provides complementary information, which allows us to estimate the Majorana polarization, a metric quantifying the extent of hybridization between MBSs [98, 99, 103].

6.2 Results

6.2.1 Model with strongly coupled dots

The Kitaev model [5] can be implemented by coupling spin-polarized QDs via Andreev bound states (ABSs) in a semiconductor-superconductor hybrid [50]. Coupling between the QDs is mediated by two types of coherent tunneling processes, as illustrated in Fig. 1b. A hopping interaction arises through elastic co-tunnelling (ECT) and a pairing interaction arises via the creation or breaking of a Cooper pair in the superconductor through crossed Andreev reflection (CAR). To emulate a Kitaev chain, the relative amplitudes of these processes must be controlled [30, 31, 89]. Furthermore, large inter-dot couplings are desired in order to isolate zero-energy

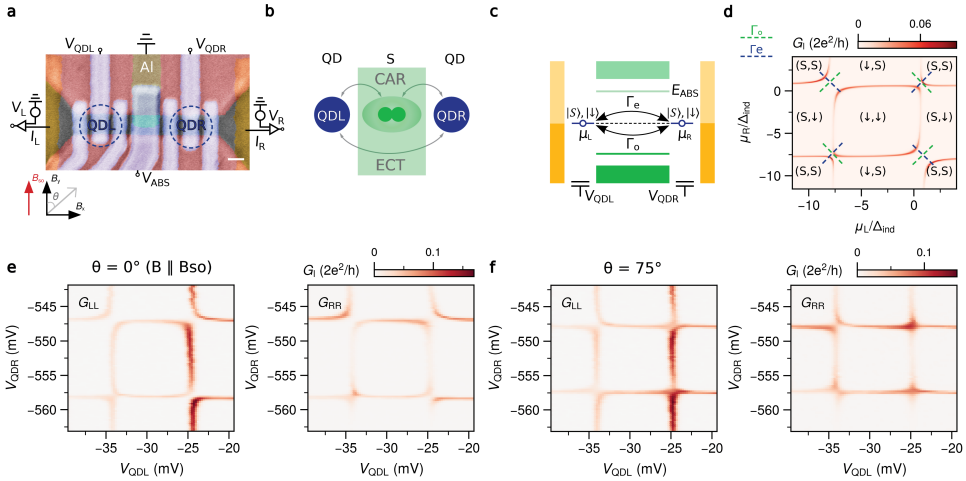

Figure 6.1: **Device, model and CSDs a.** False-colored scanning electron micrograph of device A. Inset axis shows coordinates of the external magnetic field and the expected spin-orbit field direction w.r.t. the device orientation. The gate-defined QDs (QDL and QDR) are indicated. Scale bar is 100 nm. **b.** Sub-gap transport processes between the QDs and the superconductor. ECT exchanges an electron between the QDs, while CAR allows for pairwise exchange of two electrons with the superconductor (SC). **c.** Energy level diagram showing two spin-polarized YSR-states in two QDs that are coupled through a hybrid section. An Andreev bound state (at energy E_{ABS}) mediates two types of virtual tunnel couplings between the QDs, denoted by Γ_{e} and Γ_{o}. **d.** Numerically calculated CSD of two coupled QDs, in the absence of spin-orbit coupling. Dashed lines indicate which states are expected to be hybridized through each type of coupling. **e.** Measured CSD across two charge degeneracy points in QDL and QDR with $\theta = 0^{\circ}$ ($B \parallel B_{\mathrm{SO}}$), corresponding to numerical conductance in (d). **f.** Measured CSD with $\theta = 75^{\circ}$. Data in (e) and (f) are taken at $V_{\mathrm{ABS}} = -624\,\mathrm{mV}$ and $B = 100\,\mathrm{mT}$.

MBSs from higher-energy excitations [33]. This can be achieved by increasing tunnelling rates between the QDs and the proximitized region, additionally inducing superconducting correlations in the QDs [26, 27]. In this regime the QDs can be described as Yu-Shiba-Rusinov (YSR) states [23–25, 104–106].

An energy level diagram of the system is shown in Fig. 1c, where, at finite magnetic field, the ground state of each proximitized QD is either a doublet state $|\downarrow\rangle$ or a singlet state $|\mathrm{S}\rangle$. The electro-chemical potential of the QDs are denoted μ_{L} and μ_{R}. We consider the combined state of the QDs $|\sigma_{\mathrm{L}},\sigma_{\mathrm{R}}\rangle$, where $\sigma_{\mathrm{L}},\sigma_{\mathrm{R}} \in (|\mathrm{S}\rangle, |\downarrow\rangle)$. In this description, ECT and CAR processes give rise to two types of effective couplings. States with total odd-parity ($|\mathrm{S},\downarrow\rangle$ and $|\downarrow,\mathrm{S}\rangle$) have the same total spin ($\frac{1}{2}$) and therefore couple through a spin-conserving term Γ_{o}. States with total even-parity ($|\mathrm{S},\mathrm{S}\rangle$ and $|\downarrow,\downarrow\rangle$) have different total spin (0 or 1) and couple through a spin non-conserving term Γ_{e}. Similar to a system with non-proximitized QDs [33, 35], MBSs should arise when these couplings are equal (Γ_{o}=Γ_{e}) [27], as further described

in Methods. Fig. 1d shows the numerically obtained conductance G, considering the local transport, as a function of μ_L and μ_R (details of the model can be found in Methods). This charge stability diagram (CSD) reveals avoided crossings at the charge degeneracy points, indicative of strong inter-dot coupling. In the absence of spin-orbit interaction only the spin-conserving coupling Γ_o is relevant, thus strongly hybridizing the odd-parity states. Horizontal and vertical conductance features are visible between avoided crossings as a result of local Andreev reflection, typical for YSR-states.

6.2.2 Device description

A scanning electron micrograph of a typical device (device A) is shown in Fig. 1a. Gate-defined QDs are created on the left and right of a region proximitized by aluminium (green). The QDs are strongly coupled to the superconductor, resulting in the formation of sub-gap YSR states (detailed in Fig. ED1). Biases applied to the left and right leads (V_L and V_R) can be varied and the currents in the left and right leads (I_L and I_R) can be measured simultaneously. Using standard lock-in techniques, we measure local conductances G_{LL} ($\frac{dI_L}{dV_L}$) and G_{RR} ($\frac{dI_R}{dV_R}$), denoted G_l, and non-local conductances G_{LR} ($\frac{dI_L}{dV_R}$) and G_{RL} ($\frac{dI_R}{dV_L}$), denoted G_{nl}. We report on two similar devices. Device A was used for measurements in Fig. 1, Fig. 3 and Fig. 4. Device B (image shown in S2a) was used to obtain the measurements in Fig. 2. All measurements are performed in a dilution refrigerator, with a base temperature of 20 mK.

By applying a magnetic field along the spin-orbit field, the effect of the spin-orbit interaction is suppressed (see Fig. ED2), as previously observed in similar devices [107]. We measure G_l, as V_{QDL} and V_{QDR} are swept across two charge degeneracy points in each QD, resulting in the CSDs shown in Fig. 1e. Similar to the simulations (Fig. 1d), we find avoided crossings that indicate a strong coupling between odd parity states, i.e., $\Gamma_o > \Gamma_e$. Next, we rotate the external magnetic field away from the spin-orbit field, allowing spin non-conserving processes to occur. This is reflected in the avoided crossings in the CSDs (Fig. 1f), where we indeed see that even-parity states can now hybridize, indicating a sizeable Γ_e. In particular, the top left and bottom left avoided crossings have changed direction, indicating an even-parity ground state at these charge degeneracy points. The evolution from Fig. 1e to Fig. 1f suggests that the field angle can be used to tune the system into the sweet spot ($\Gamma_o = \Gamma_e$) where MBSs emerge.

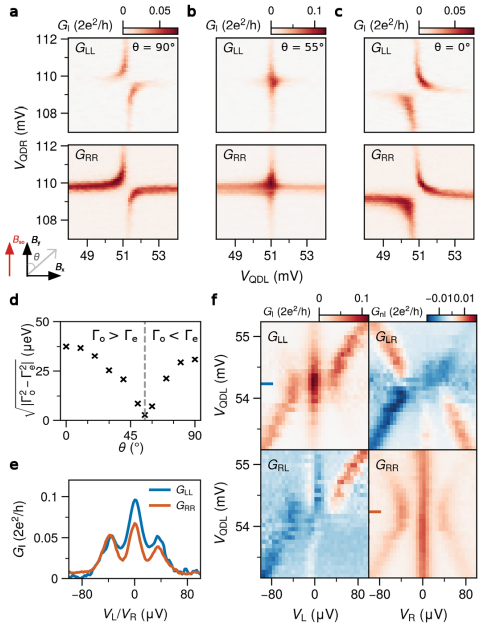

Figure 6.2: **Tuning Γ_e and Γ_o with magnetic field angle.** Measurements obtained for device B, characterized in Fig. ED2. **a.** CSD showing a diagonal avoided crossing ($\Gamma_e > \Gamma_o$), obtained with $B \perp B_{SO}$. **c.** Rotating the field such that $B \parallel B_{SO}$, the avoided crossing changes direction ($\Gamma_e \approx < \Gamma_o$). **b.** At 55° the the avoided crossing disappears ($\Gamma_e = \Gamma_o$). **d.** Extraction of $\sqrt{|\Gamma_o^2 - \Gamma_e^2|}$ from CSDs measured at various magnetic field angles. **e.** G_l measured at the centre of the CSD in (b), showing correlated zero-bias peaks. **f.** G_l and G_{nl} measured upon detuning V_{QDL}, while keeping V_{QDR} on resonance. Correlated zero-bias peaks persist across a large voltage range. Raw data and the extraction procedure is presented in Fig. ED3. Measurements are taken at B =80 mT.

6.2.3 Tuning to the Majorana sweet spot

We demonstrate this control in Fig. 2. Fig. 2a shows a CSD obtained with $B \perp B_{SO}$, around the charge transition corresponding to the lower left corner of Fig. 1d. The diagonal avoided crossing here indicates that $\Gamma_e > \Gamma_o$. Rotating the field to align with B_{SO} results in an anti-diagonal avoided crossing, as now $\Gamma_o > \Gamma_e$ (Fig. 2c). The separation between the branches of the avoided crossing is proportional to $\sqrt{|\Gamma_o^2 - \Gamma_e^2|}$ (detailed in Methods), which can be used to quantify the relative strength of the couplings. Measuring this quantity for several angles (Fig. 2d) shows a smooth evolution of the coupling strength as a function of the field angle. Importantly, at an intermediate angle the avoided crossing disappears (Fig. 2b), indicating $\Gamma_e = \Gamma_o$. Under these conditions, the odd and even parity ground states are degenerate at the charge degeneracy point, i.e., $\delta\mu_L = \delta\mu_R = 0$, leading to localized MBSs on each QD [27]. We refer to this point in parameter space as the Majorana sweet spot. At the sweet spot, simultaneous tunneling spectroscopy on the left and right QD

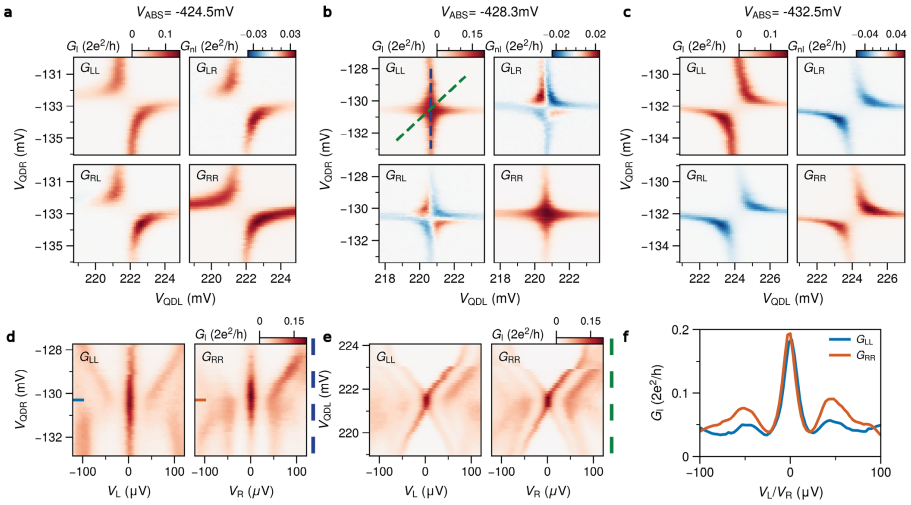

Figure 6.3: **Electrostatically tuning to the Majorana sweet spot. a.**, **b.** and **c.** show CSDs taken at three different applied voltages V_{ABS}, in device A. The system is smoothly tuned from the $\Gamma_o > \Gamma_e$ regime in (a) to the $\Gamma_o < \Gamma_e$ regime in (c). In between, the $\Gamma_o = \Gamma_e$ condition is satisfied (b). A more extensive range is highlighted in Fig. ED6. **d.** Tunneling spectroscopy measurements at the sweet spot. V_{QDR} is tuned along the blue path shown in (b), while QDL is kept on resonance. **e.** Tunneling spectroscopy as V_{QDL} and V_{QDR} are tuned simultaneously along the green path shown in (b). **f.** Line-trace from (d) with V_{QDL} and V_{QDR} tuned to the sweet spot in (b) (corresponding to $\delta\mu_L = \delta\mu_R = 0$). Data is taken with $B = 150\,\mathrm{mT}$.

demonstrates correlated ZBPs (Fig. 2e). Higher energy excitations are visible at $\pm\,40\,\mu$V, providing an estimate of the effective couplings at the sweet spot to be $\Gamma_e = \Gamma_o \approx 20\,\mu$eV. These ZBPs are expected to persist when only a single QD is perturbed, as they result from MBSs localized on each of the QDs. To confirm this, we measure G_l and G_{nl} upon detuning V_{QDL}, while keeping V_{QDR} constant (Fig. 2f). The ZBPs indeed persist in G_l, while higher energy excitations are observed to disperse when QDL is detuned. Further, in G_{nl} only the higher energy excitations are visible while the ZBPs themselves do not appear, a signature of the localized nature of these zero-energy states. These observations are consistent with experiments on nanowires [50] and theoretical predictions [33].

The above procedure for tuning to the sweet spot is guaranteed to work if one starts with a field angle where $\Gamma_e > \Gamma_o$, since Γ_e can always be decreased by rotating the field towards B_{SO}. If a field rotation reveals that such an angle cannot be found, one can reach the sweet spot via electrostatic control over the hybrid section [50], since Γ_e and Γ_o are affected by the charge and energy of the Andreev bound states [30, 31]. In our devices the Andreev bound state energies are controlled

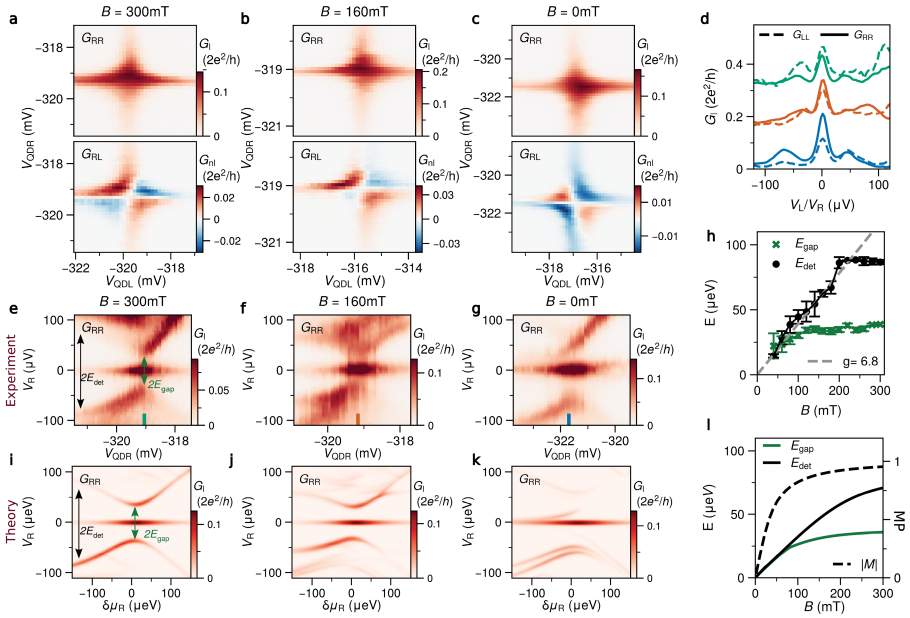

Figure 6.4: **Majorana sweet spots in varying magnetic field. a.**, **b.** and **c.** CSDs at "Majorana sweet spots" measured at applied fields of 300 mT, 160 mT and 0 mT respectively. At each field, V_{ABS} is adjusted to tune to the "sweet spot", following the procedure from Fig. 3. **d.** G_{RR} (solid) and G_{LL} (dashed) line-cuts at the centre of each CSD, from indicated positions in (e-g), highlighting the presence of correlated ZBPs. Offsets of 0.15 and 0.3 are applied for 160 mT and 300 mT respectively. **e.-g.** Measured G_{RR} upon detuning QDR, while keeping QDL on resonance. Data is saturated for visibility of the excited states. Energies of interest (E_{gap} and E_{det}) are highlighted in (e). **h.** Extraction of the energies E_{gap} and E_{det} from measurements between 300 mT and 0 mT (full dataset in Fig. ED9). Dashed line shows a linear fit of E_{det}, providing an estimate for the g-factor of QDL. **i.-k.** Numerically calculated conductance, for qualitative comparison with (e-g). **l.** Numerically extracted evolution of E_{gap} and E_{det} (solid) and corresponding Majorana polarization $|M|$ (dashed) as a function of the magnetic field.

via the voltage V_{ABS}, applied to the gate above the proximitized region. With the magnetic field directed away from the spin-orbit field (as in Fig. 1f), we study the evolution of the CSDs with V_{ABS}. Fig. 3a shows a diagonal avoided crossing, signifying here that $\Gamma_o > \Gamma_e$. By tuning V_{ABS}, the avoided crossing changes direction, indicating $\Gamma_e > \Gamma_o$ (Fig. 3c). At an intermediate V_{ABS} the avoided crossing disappears (Fig. 3b), satisfying the sweet spot condition ($\Gamma_e = \Gamma_o$). Similar to Fig. 2, we now detune V_{QDR} along the blue dashed line in Fig. 3b and measure G_I, again finding correlated, persisting ZBPs (Fig. 3d). Line-cuts from Fig. 3d are shown in Fig. 3, giving an estimate of $\Gamma_e = \Gamma_o = 25\,\mu$eV. When both QDs are detuned simultaneously, along the green dashed line in Fig. 3b, the correlated ZBPs disperse quadratically (Fig. 3e). This is expected for a two-site Kitaev chain, where the ZBPs are only

protected from local perturbations [33]. An extended dataset and a comparison with numerical results is shown in Fig. ED5.

In addition to G_{I}, the non-local measurements in Fig. 3a-c can provide further information about underlying transport mechanisms. For example, it has been shown that for CAR, local and non-local signals have the same sign, while for ECT their sign should be opposite [89]. Since charge is ill-defined for YSR-states, there is no one-to-one correspondence between the dominant inter-dot coupling (i.e., Γ_e, Γ_o) and the dominant underlying transport mechanism (i.e., CAR, ECT). Nevertheless we find a qualitatively similar behavior, whereby for $\Gamma_o > \Gamma_e$ the non-local conductance is positive, whereas for $\Gamma_e > \Gamma_o$ it is negative. We show that this is indeed expected (see Fig. ED7), and that the sign of G_{L} is dictated by the positions of the QDs w.r.t. their charge degeneracy.

6.2.4 Majorana polarization

The ideal Kitaev chain is based on a spinless model. Thus, emulating this system with spinful QDs, as presented here, requires the Zeeman energies of the QDs to be sufficiently large compared to the effective coupling between the QDs [27, 33, 35, 97, 99]. In addition, MBSs on either QD should be isolated from each other. A parameter capturing these factors is the so-called Majorana polarization (MP) [103], which has recently been investigated theoretically in the context of Kitaev chains [98]. The MP is a metric (denoted $|M|$) that quantifies the extent to which localized MBSs hybridize, and is relevant for experiments that require controlled manipulation of multiple MBSs, such as braiding [99, 102] and parity-based qubits [33, 101, 108, 109]. The MP ranges from 0 (lowest polarization) to 1 (highest polarization), and in experiments it is desirable to have a high value of MP. It was shown that both “low" and “high" MP can result in similar transport signatures [98], raising an important question about how one could experimentally distinguish between these regimes.

In order to investigate this, we track the evolution of the system from 300 mT to 0 mT (along B_z). At each field, we find similar crossings in the CSDs (Fig. 4a-c). Simultaneous tunneling spectroscopy of the QDs at these crossing points reveal correlated ZBPs, down to zero magnetic field (Fig. 4d). Furthermore, the behavior of non-local conductance around the centre of each crossing [98] also shows no discernible differences as the field is reduced. At first instance, these observations are surprising, since MBSs require time reversal symmetry to be broken. However, we note that the combination of time-reversal symmetry and Coulomb interactions can result in robust zero energy modes associated with Kramers pairs of Majorana zero modes, as discussed in [32]. While further investigation is needed to confirm this interpretation, we can conclude that experimentally it is difficult to extract information about the MP from such measurements.

On the other hand, we find that the dispersion of higher energy excitations in tunnelling spectroscopy has a distinctly different behavior at each magnetic field, and allows us to obtain information about the MP. While the ZBPs themselves persist upon detuning QDR for all values of B, the excited states show a markedly different behavior (Fig. 4e–g). For example, at large detuning of QDR, excited states are visible at $\pm 100\,\mu$V in Fig. 4e, while reaching only $\pm\ 60\,\mu$V in Fig. 4f. We denote this energy difference between the first excited states and the ZBPs as E_{gap} at the sweet spot and as E_{det} at large negative detuning, and extract these energies over an extensive range in B (Fig. 4h). Both E_{det} and E_{gap} are found to increase monotonically with increasing magnetic field. For these sets of measurements, E_{gap} starts to saturate at $30\,\mu$V at higher fields, while E_{det} increases linearly until saturating at $80\,\mu$V. The latter can be expected, since the excitation energy of the hybrid system approaches the excitation energy, i.e., the Zeeman energy of an isolated QD, when either of the QDs is detuned.

We compare these measurements with numerical simulations of the system with input from experimental parameters, and find that indeed E_{det} provides a lower bound estimate of E_{z} of the QDs (Fig. ED8). This allows to approximate a g-factor from Fig. 4h. Using this, the simulated spectra demonstrate a qualitatively similar behavior in the dispersion of the excited states (Fig. 4i-k). Furthermore, we find that the evolution of both E_{gap} and E_{det} compare well to the experimental results (Fig. 4l).

These results allow us to numerically estimate the Majorana polarization for the system, as a function of magnetic field (Fig. 4l). We find that as B increases, the MP increases quickly from 0 and then starts to approach 1 around 100 mT, where E_{gap} begins to saturate. The comparison here yields $|M| \approx 0.96$ at around $B = 300\,\mathrm{mT}$. A similar analysis is performed for measurements using the sweet spot shown in Fig. 3, where E_{gap} reaches $50\,\mu$V, from which we extract a lower MP estimate of $|M| \approx 0.9$ (Fig. ED10). Whether these estimates can be considered a “high" MP is dependent on the operations one intends to perform. For example, specific braiding protocols have been shown to be reliable for $|M| = 0.98$ [99]. It should be noted that these experiments do not constitute a direct measurement of the MP. One way to achieve this would be to introduce an additional QD on either side with a tunneling coupling to either MBS [110–112]. Regardless, the presented measurements show that the evolution of the system from zero magnetic field to high magnetic field can be well understood within the framework of the Kitaev model.

6.3 Conclusion

In summary, we have implemented a two-site Kitaev chain in a two-dimensional electron gas by coupling QDs through ABSs in a superconductor-semiconductor

hybrid region. We demonstrate a smooth control over the inter-dot couplings, both by rotations of the magnetic field and by tuning the energy of Andreev bound states in the hybrid section. At specific points in the parameter space, zero energy excitations arise that are stable against local perturbations of either QD. We show that these “sweet spots" (accompanied by correlated ZBPs) appear in the system even at zero Zeeman energy, and are by themselves insufficient to gain information about the polarization of MBSs. Rather, we find that the magnetic field dependence of the energy spectrum allows us to distinguish between high and low polarization regimes. Our work demonstrates that artificial Kitaev chains can now be realized on a scalable and flexible platform, and that 2DEGs are poised to perform Majorana-based experiments that were previously inaccessible.

Data availability and Code Availability Raw data and analysis scripts for all presented figures are available at
https://doi.org/10.5281/zenodo.10077539.

6.4 Methods

6.4.1 Device fabrication and yield

All devices were fabricated using techniques described in detail in [96]. A narrow aluminum strip is defined in an InSbAs-Al chip by wet etching, followed by the deposition of two normal Ti/Pd contacts. After deposition of 20 nm AlOx via atomic layer deposition (ALD), two Ti/Pd depletion gates are evaporated. Following a second ALD layer (20 nm AlOx), seven Ti/Pd finger gates are evaporated in order to define the QDs and tune the ABSs energy. The two depletion gates define a quasi-1D channel with a width of about 160 nm, contacted on each side by a normal lead. The aluminium strip induces superconductivity in the middle section of each device, with an induced gap on the order of 200 μeV. The presence of extended ABSs is confirmed through tunnelling spectroscopy. ABSs are found to be present over a large range of V_{ABS}, the voltage applied to the gate covering the hybrid region. Finger gates on the left and right of the aluminium define QDs with charging energies above 1 mV (Fig. ED1 a,b).

Two devices were used to obtain the data presented in the main text (device A and device B). Both showed strong hybridization between the QDs, as presented here. Device A was used to study the field evolution of Majorana sweet spots and to obtain the measurements presented in Fig. 1, Fig. 3 and Fig. 4. Device B was used to demonstrate the role of spin-orbit coupling on the interdot interactions, and the control over interactions through magnetic field as presented in Fig. 2. Regarding device yield, up till now we have measured 12 devices for the purpose of studying hybridized QDs. Of these, we could tune 8 devices to regimes with strongly coupled QDs that showed the tunability displayed in Fig. 3. Of the non-functional devices, 2 failed due to trivial reasons (e.g. losing electronic connection due to missing bondwires after cooling). The remaining 2 devices failed at the stage of forming the 1-D channel, where we found some optimization was needed to discover the optimal separation between the top and bottom depletion gate.

6.4.2 Transport measurements and data processing

Measurements were performed in a dilution refrigerator with a base temperature of 20 mK. Transport measurements are performed in AC and DC using a three-terminal set-up, where the aluminum is electrically grounded. Each Ohmic lead is connected to a current-to-voltage converter and biased through a digital-to-analogue converter that applies both DC and AC biases. Offsets of the applied voltage-bias on each side are corrected via independently calibrating the Coulomb peaks in the QDs on each side. The voltage outputs of the current meters are recorded with two digital multimeters and two lock-in amplifiers. When applying a DC voltage to the left Ohmic (V_{L}) the right lead (V_{R}) is kept grounded and vice versa. AC excitations are applied on each side with amplitudes around 5 μV RMS

and frequencies of 19 Hz (left) and 29 Hz (right). In this way, we measure the full conductance matrix G by first measuring the response of I_L and I_R to V_L and then to V_R. We account for the voltage-divider effect by correcting the conductances using known fridge line resistances (3.6 kΩ in device A, 3.3 kΩ in device B), as detailed in [77]. This correction was done for all presented spectroscopy data, except for the data shown in Fig 3d-f. Magnetic fields were applied using a 3D vector magnet. The alignment of the magnetic field of device A is expected to be accurate within ±10° and calibrated through performing tunneling spectroscopy of the hybrid section as a function of field angle. The alignment of device B is expected to be accurate within ±5°.

Due to device instabilities or charge jumps, electrostatics of the QDs experience small drifts over the course of the measurements. Investigated orbitals were tracked while collecting the presented datasets. For each tunnelling spectroscopy measurements at a sweet spot, where V_{QDL} and/or V_{QDR} were detuned, a CSD was obtained directly before and directly after to ensure that no drifts occurred during such a measurement. If such a drift occurred, the measurement was discarded and repeated. Such drifts are the cause of small discrepancies in gate voltages between highlighted paths in Fig. 3b and the measurements shown in Fig. 3d,e. The highlighted paths represents the corrected path taken w.r.t. the CSD shown in Fig. 3b, based on the CSDs obtained before and after the measurements.

6.4.3 Extracting QD parameters

In order to compare energy scales between experiments and numerical calculations, the gate voltages V_{QDL} and V_{QDR} are converted to electro-chemical potential energies μ_{L} and μ_{R}. For this purpose we extract the dimensionless lever arms α. When forming sub-gap YSR states in the QDs, the effective lever arm of each QD around a zero-bias charge degeneracy can differ from the lever arm of the uncoupled QD, depending e.g. on hybridization with the hybrid region (Fig. ED4), extensively addressed in [26]. For analysis we therefore estimate both the normal-state lever arm (denoted α_{N}) and the lever arm of the sub-gap YSR-states (denoted α_{YSR}), at the specific V_{ABS} regimes of interest. Device B was operated in a regime without significant difference between α_{N} and α_{YSR}, such that the analysis in Fig. 2d uses the lever arms extracted in Fig. ED2. With the orbitals in Fig. 4, sweet spots were investigated at magnetic field values between 0 mT and 300 mT, where the energy of excited states E_{det} was extracted at a fixed detuning of V_{QDR}. A g-factor is extracted from this data, by a linear fit of E_{det} up to 180mT (before saturation). For this dataset α_{YSR} was only obtained at 0 mT (Fig. ED1), such that any change in α_{YSR} as a function of magnetic field can not be accounted for in the analysis in Fig. 4l and Fig. 4. When extracting E_{det} at constant detuning of V_{QDR} at each field, μ_{R} may not be constant but rather is expected to decrease (Fig. ED4). We note that the lack of

this correction may lead to slightly underestimating the g-factor in Fig. 4h, which in turn will lead to a lowered estimation of the Majorana polarization. For the extractions of E_{det} and E_{gap}, G_{LL} and G_{RR} line-traces are obtained at the sweet spot and at a detuning of V_{QDR} of -2mV, corresponding to a detuning of $\mu_{\mathrm{R}} \approx 100\,\mu$eV. From each line-trace, the separation between the ZBPs and the first higher energy excitation is extracted by fitting Gaussian peaks symmetrically around zero-bias. Error-bars are given by the uncertainty in these fits.

6.4.4 Numerical transport calculations

For all presented numerical results, a description of the system incorporating both the two QDs and the middle hybrid section was used, recently introduced in [98]. We employ the same model and highlight key points and used numerical parameter below. The model considers tunneling between two normal QDs (L,R) and a central QD (M), which is in proximity to a superconductor. Each site j has electrochemical potential energy μ_j. A spin-conserving hopping t allows transport between the outer QDs and central QD. The effect of spin-orbit interactions is included through a spin-flip hopping term t_{SO} between the outer QDs and central QD. The presence of the SC is included by attributing a superconducting pairing term Δ_i in each QD. To match the experimental geometry, $\Delta_{\mathrm{L,R}}, < \Delta_{\mathrm{M}}$ Lastly, the left and right sites are assigned a large on-site charging energy U and a Zeeman splitting E_z between the $|\downarrow\rangle$ and $|\uparrow\rangle$ occupation. The Hamiltonian is constructed as follows:

$$
\begin{aligned}
H = &\sum_{j,\sigma} \mu_j n_{j\sigma} + \sum_j U_j n_{j\uparrow} n_{j\downarrow} + \sum_j E_{Zj}(n_{j\downarrow} - n_{j\uparrow}) \\
&+ \sum_{j\neq \mathrm{M},\sigma} [t_j d^\dagger_{j\sigma} d_{C\sigma} + h.c.] \\
&+ \sum_{j\neq \mathrm{M}} [t^{\mathrm{SO}}_j d^\dagger_{j\downarrow} d_{C\uparrow} - t^{\mathrm{SO}}_j d^\dagger_{j\uparrow} d_{C\downarrow} + h.c.] \\
&+ \sum_j [\Delta_{\mathrm{j}} d^\dagger_{j\uparrow} d^\dagger_{j\downarrow} + h.c.]
\end{aligned}
$$

where $d_{j\sigma}, d^\dagger_{j\sigma}$ and $n_{j\sigma}$ are the annihilation, creation, and number operators respectively for each site. The sum j runs over the sites (L,M,R) and σ over the spin degree of freedom $(\uparrow,\downarrow)$. For simplicity, a left and right symmetry is assumed, such that a Majorana sweet spot lies along $\mu_{\mathrm{L}} = \mu_{\mathrm{R}}$. Sweet spots are obtained by scanning the parameter space spanned by $\mu_{\mathrm{L}} = \mu_{\mathrm{R}}$ and μ_{M} and finding degeneracies between lowest odd and even eigenstates. All transport calculations are obtained using the rate equation detailed in [98]. Similar to [98], we calculate the quantity of Majorana polarization (MP) (originally introduced in [103]). This quantity, denoted M_j, is

defined per site j as:

$$M_j = \frac{\sum_\sigma (w_\sigma^2 - z_\sigma^2)}{\sum_\sigma (w_\sigma^2 + z_\sigma^2)}$$
$$w_\sigma = \langle O|(d_{j\sigma} + d_{j\sigma}^\dagger)|E\rangle$$
$$z_\sigma = \langle O|(d_{j\sigma} - d_{j\sigma}^\dagger)|E\rangle$$

where $|O\rangle$ and $|E\rangle$ are the lowest-energy odd and even states respectively. Due to symmetrically chosen parameters $|M_\mathrm{L}| = |M_\mathrm{R}| = |M|$, such that a single MP value can be extracted for a specific set of parameters. To provide an experimental observable that reflects a high or low $|M|$, we investigate the behavior of two transition energies, denoted in the main text as E_gap and E_det. Numerically these are obtained from the Hamiltonian as the energy difference between the lowest even state and the second-lowest odd state, at specific values of μ_L and μ_R. E_gap is obtained with μ_L and μ_R set to corresponding to their sweet spot value. E_det is obtained with μ_R detuned by $\approx \Delta_\mathrm{M}$. In the absence of the Zeeman term, both E_gap and E_det are zero by definition, due to the degeneracy of the odd states in the presence of time reversal symmetry. The dependence of M, E_gap and E_det on E_z is demonstrated in Fig. ED10.

In order to compare to experiments, parameters are selected to match realistic values. We set $\Delta_\mathrm{M} = 100\,\mu\mathrm{eV}$ and $\Delta_\mathrm{L,R} = 0.5\Delta_\mathrm{M}$. The charging energy U is fixed in both dots to be $10\Delta_\mathrm{M}$, except for Fig. 1d where a value of $7\Delta_\mathrm{M}$ is used to better highlight the behavior of all four avoided crossings in the large CSD. For the analysis in Fig. 4, tunneling terms t and t_SO are fine-tuned such that at large E_z the sweet spot gap of $30\,\mu\mathrm{eV}$ is obtained, to match the experimental result. This gives $t_\mathrm{SO} = 0.4t = 0.7\Delta_\mathrm{M}$. Similarly, to compare to the experimental results in Fig. ED5 and Fig. ED10, t and t_SO are fine-tuned to obtain a sweet spot gap of $50\,\mu\mathrm{eV}$ at large E_z. This results in $t_\mathrm{SO} = 0.4t = 0.85\Delta_\mathrm{M}$.

6.4.5 Effective model in the strong coupling regime

The above description is used for all presented calculations. To provide an intuitive understanding of these results, we invoke a description of the system through an effective model, introduced in detail in [27]. Here we provide a brief summary of the relevant findings. When the energy E_ABS of the sub-gap state in the middle site is large compared to tunnel couplings between the QDs, the middle site can be integrated out. This leaves a description of the system including only effective couplings between YSR states in the left and right QD sites. Additionally, it is assumed that E_z is sufficiently large such that only the $|\downarrow|$ occupation of each QD

partakes in transport. In this description, a Hamiltonian can be constructed in a singlet-doublet basis. The ground state of each QD is either the $|\downarrow\rangle$ doublet or a singlet $|S\rangle$ of the form $|S\rangle = u_{\mathrm{L,R}}|0\rangle - v_{\mathrm{L,R}}|\downarrow\uparrow\rangle$. Here the u,v components depend on the chemical potential energies μ_{L} and μ_{R} of the left and right dot: ($u^2_{\mathrm{L,R}} = 1 - v^2_{\mathrm{L,R}} = \frac{1}{2} + \frac{\mu_{L,R}+U}{\sqrt{U^2+E^2_{\mathrm{ABS}}}}$). The effective Hamiltonian is obtained:

$$H^{\mathrm{eff}}_{\mathrm{coupling}} = \sum_{\sigma,\eta=\uparrow,\downarrow} (t_{\sigma\eta} c^{\dagger}_{L\sigma} c_{R\eta} + \Delta_{\sigma\eta} c^{\dagger}_{L\sigma} c^{\dagger}_{R\eta}) + h.c., \tag{6.1}$$

where $c_{\mathrm{L,R}}$ and $c^{\dagger}_{\mathrm{L,R}}$ are annihilation and creation operators for the left and right sites. Further, $t_{\sigma\eta}$ specifies the amplitude of an electron with spin σ from left site tunneling to occupy a state with spin η in the right side, or vice versa. $\Delta_{\sigma\mu}$ specifies the amplitude of the creating or breaking of a Cooper pair through electrons with spins σ and η in the left and right QDs ($\sigma,\eta \in [\uparrow,\downarrow]$). Due to the spin-orbit interaction two equal-spin electrons can also be coupled via the Δ-term. Importantly, this description is equivalent to the weakly coupled model discussed in [33], when changing from a charge occupation basis to a YSR-state basis. Now, two types of coupling arise between the total even-parity states (denoted Γ_{E}) and between total-odd parity states (Γ_{O}). Each are combination of ECT and CAR amplitudes:

$$\begin{aligned}
\Gamma_{\mathrm{E}} &= \langle SS|H^{\mathrm{eff}}_{\mathrm{coupling}}|\downarrow\downarrow\rangle &&= -\Delta_{\uparrow\uparrow} v_L v_R + \Delta_{\downarrow\downarrow} u_L u_R + t_{\uparrow\downarrow} v_L u_R - t_{\downarrow\uparrow} u_L v_R, \\
\Gamma_{\mathrm{O}} &= \langle S\downarrow|H^{\mathrm{eff}}_{\mathrm{coupling}}|\downarrow S\rangle &&= -t_{\uparrow\uparrow} v_L v_R + t_{\downarrow\downarrow} u_L u_R + \Delta_{\uparrow\downarrow} v_L u_R - \Delta_{\downarrow\uparrow} u_L v_R,
\end{aligned}$$

The coupling Γ_{O} results in bonding and anti-bonding states of the form $u|\mathrm{S},\downarrow\rangle \pm v|\downarrow,\mathrm{S}\rangle$. Γ_{E} forms bonding and anti-bonding states of the form $\alpha|\mathrm{S},\mathrm{S}\rangle \pm \beta|\downarrow,\downarrow\rangle$. When $\Gamma_{\mathrm{E}} = \Gamma_{\mathrm{O}}$ the even and odd ground states become degenerate at $\mu_{\mathrm{L}} = \mu_{\mathrm{R}}$, equivalent to the $t = \Delta$ condition in the "poor Man's Majorana" description [33]. In Fig. 2d, we extract the distance between the branches of the avoided crossing in the experimentally obtained CSDs, after converting the gate voltages to the YSR energies of each QD. In the effective description this distance corresponds to analysing where the line $\mu_L = \mu_R$ or $\mu_L = -\mu_R$ intersects a degeneracy between the even and odd ground state energies. This gives two points, separated by $\sqrt{8|\Gamma^2_{\mathrm{O}} - \Gamma^2_{\mathrm{E}}|}$.

6.4.6 Extended data figures and tables

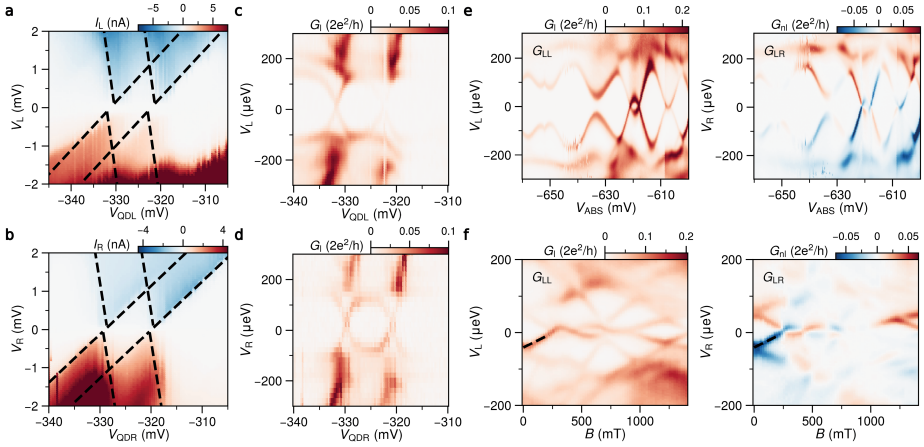

Figure ED1: **Characterization of QDs and ABS spectroscopy for device A. (a-b)** Coulomb diamond measurements of the left and right QDs, in the regime used for measurements presented in Fig. 4.. Charging energies are estimated to be 1.1 meV in each QD. The lever arm of the left and right dot is estimated to be $\alpha \approx 0.11$. **(c-d)** Close-ups of figures (a) and (b). Due to a large tunnel coupling between the QDs and the hybrid section, YSR-states form in the sub-gap spectrum of the QDs. The spectroscopy around the charge degeneracy points in (a-b) reveal clear sup-gap features within the Coulomb diamonds, whose dependence on V_{QDL} and V_{QDR} is typical for YSR-states. **(e)** Crossed Andreev reflection and elastic co-tunneling require the presence of extended ABSs. Local G_{l} and non-local conductance G_{nl} of the hybrid region are measured via tunnelling spectroscopy and their identical energy dependence as a function of V_{ABS} highlights that ABSs extend across the entire hybrid section. Comparable behavior was observed in a wide V_{ABS} range from 0 to -1 V. The measurement presented in Fig. 1 is taken at the V_{ABS} with the eye-shaped crossing. **(f)** ABS spectroscopy as a function external magnetic field at $V_{\mathrm{ABS}} = -623$ mV. The effect of splitting of the doublet state can be observed at low fields. A g-factor of 5.5 is extracted by linear fitting of the lowest sub-gap states (dashed line) in Figure ED1f.

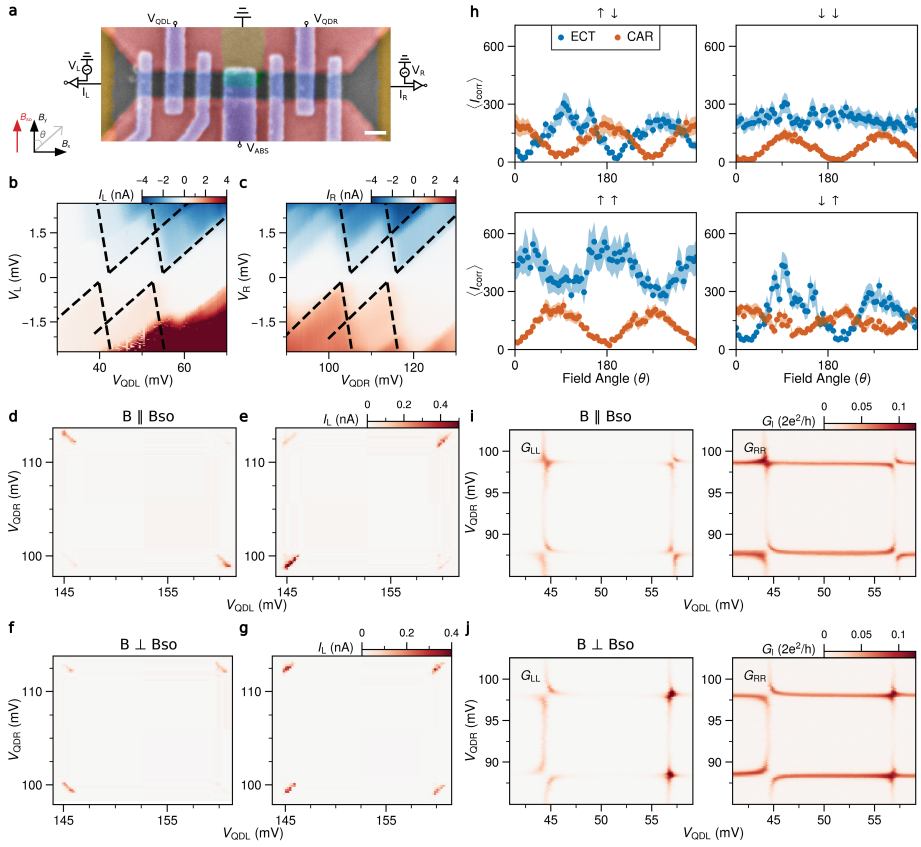

Figure ED2: **Characterization of device B. (a)** Scanning electron micro-graph of device B, used to obtain the measurements presented in Fig. 2. Scale bar shown is 100 nm. **(b-c)** Coulomb diamond measurements of the left and right QDs. Charging energies are extracted to be 1.4 meV. The lever arm α_N is extracted to be about 0.11 for each QD. This lever arm is used for the extraction in Fig. 2d. (**d-e**) To validate the direction of B_{SO} and to show the connection between interactions in strongly coupled QDs and underlying ECT and CAR processes, we first measure ECT and CAR currents in the weakly coupled dots, as detailed in [107]. With $B \perp B_{SO}$, measurements of CAR (d) and ECT (e) show the typical blockades for same-spin and opposite-spin charge configurations respectively. In (**f-g**), with $B \parallel B_{SO}$, the spin non-conserving ECT and CAR processes are observed to be revived. **(h)** Measuring CAR and ECT rates as a function of magnetic field angle θ shows the currents for the spin non-conserving processes are indeed smoothly controlled and become suppressed when $\theta = 0$. This supports the interpretation that $B \parallel B_{SO}$ when B is perpendicular to the 1-D channel. **(i-j)** Next, the QDs are operated with higher tunnelling rates between the QDs and the SC, to enable strong couplings. Similar to Fig. 1e-f, CSDs are obtained in the strongly interacting regime, taken with the verified $B \parallel B_{SO}$ and $B \perp B_{SO}$ respectively.

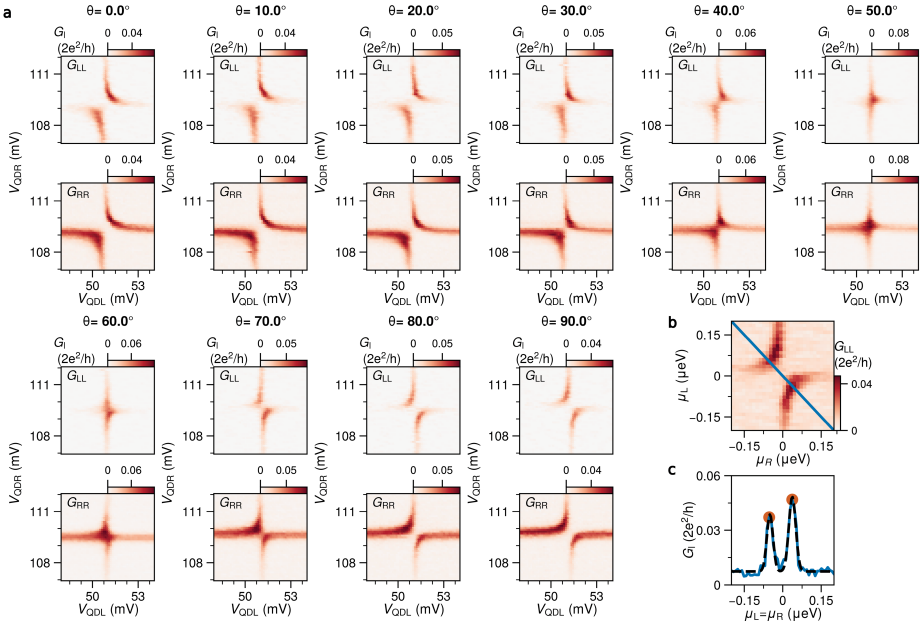

Figure ED3: **Extended dataset of Figure 2**. **(a)** CSDs measured at various magnetic field angles θ between 0° and 90°, used to extract the data shown in Fig. 2d. **(b)** Example of the extraction process. For each obtained CSD, V_{QDL} and V_{QDR} are converted to energies μ_{L} and μ_{R} using lever arms obtained in Fig. S2. Next, the conductance is extracted along a $\mu_{\mathrm{L}} = -\mu_{\mathrm{R}}$ or $\mu_{\mathrm{L}} = \mu_{\mathrm{R}}$ line. **(c)** Two Gaussian peaks are fitted to extract the separation between the two avoided crossings, from which the quantity $\sqrt{|\Gamma_{\mathrm{o}} - \Gamma_{\mathrm{e}}|}$ is obtained (plotted in Fig. 2d).

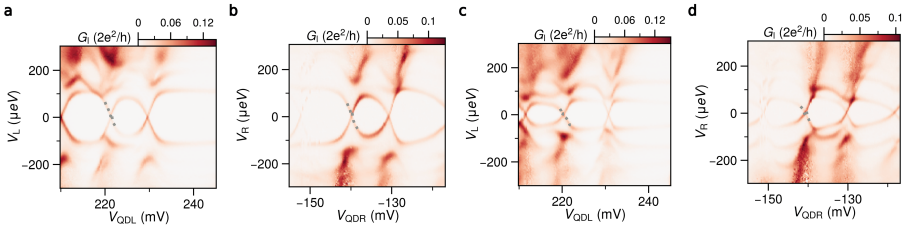

Figure ED4: **Characterisation of YSR-states in QDs of Figure 3.** To complement the data in Fig. 3, Fig S5 and Fig. S10, we measure the sub-gap states in QDL and QDR (see Fig S1). Using this, we obtain the lever arms of V_{QDL} and V_{QDR} on the YSR-state energies (denoted α_{YSR}) (see Methods). **(a-b)** Sub-gap spectroscopy of QDL and QDR at B_z=0 mT. From the slopes of the states upon crossing $V_{\mathrm{L}}, V_{\mathrm{R}} = 0$, we estimate $\alpha_{\mathrm{YSR}} \approx 0.045$. Applying an external magnetic field lowers the energy of ABSs in the hybrid region, as a result of Zeeman splitting, This in turn will affect the YSR-spectrum of the QDs, due to increased hybridization between the QDs and the ABS. **(c-d)** Measuring sub-gap spectroscopy of QDL and QDR at B_z=225 mT for the same settings as in (a-b) shows indeed the effective lever arm here decreases to $\alpha_{\mathrm{YSR}} \approx 0.028$.

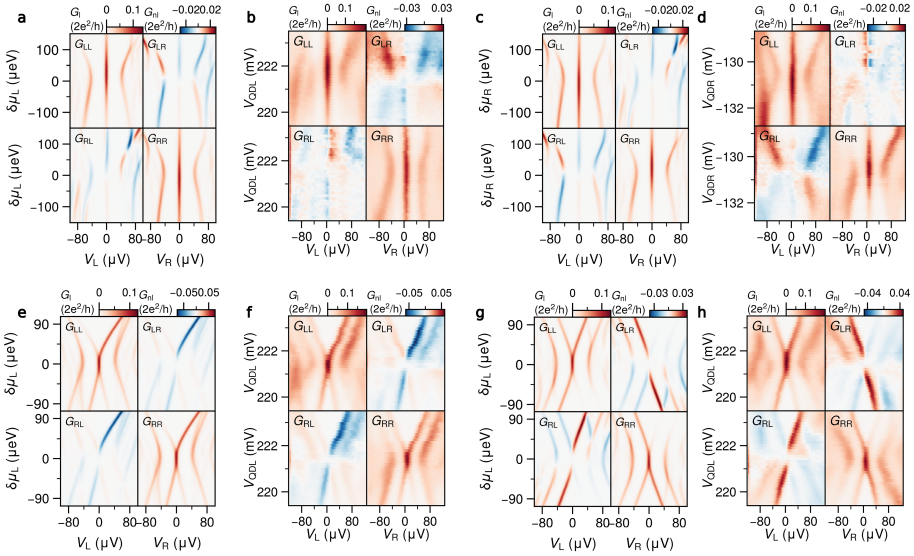

Figure ED5: **Full conductance spectra at the sweet spot upon detuning V_{QDL} and V_{QDR}.** A comparison between numerically calculated conductance and measured conductance in support of Figure 3, measured at $B = 225\,\mathrm{mT}$. Presented results show the evolution of G_{l} and G_{nl} for four different cases: **(a-b)** detuning V_{QDL}, **(c-d)** detuning V_{QDR}, **(e-f)** detuning both V_{QDL} and V_{QDR} simultaneously along a diagonal path and **(g-h)** detuning both anti-diagonally. For each case, we find the behavior of both G_{l} and G_{nl} is well described by the numerical results.

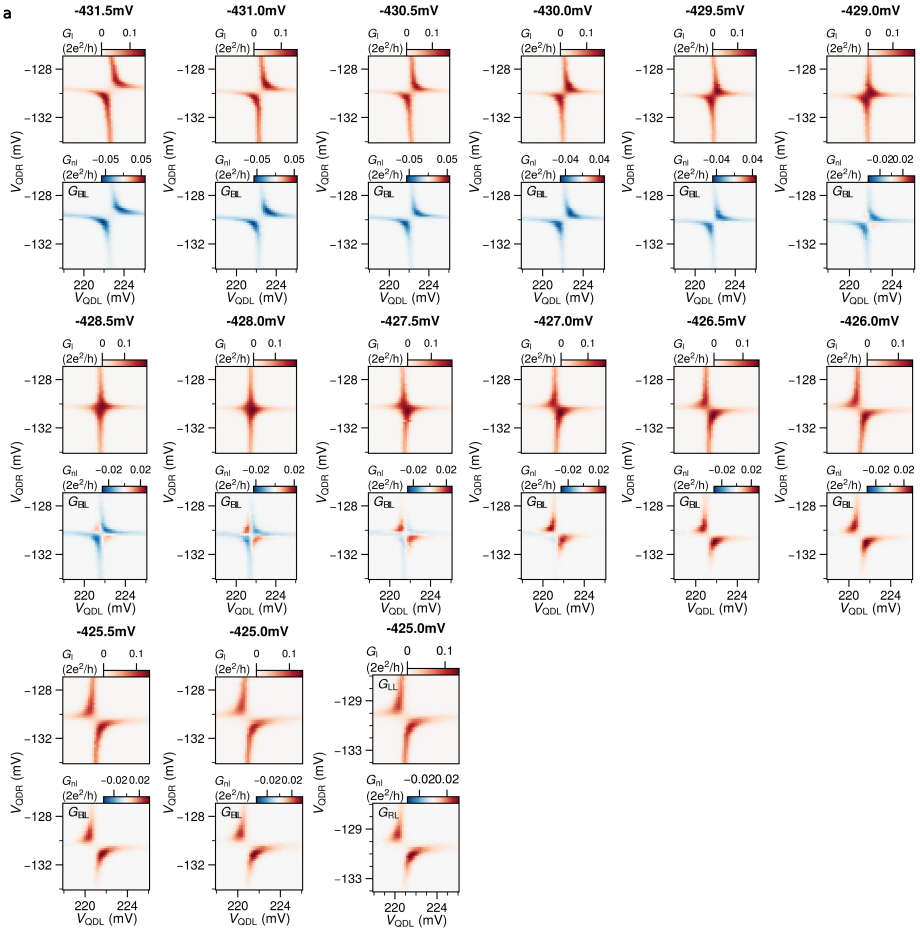

Figure ED6: **Extended dataset for Figure 3. (a)** Sets of CSDs obtained while varying V_{ABS} in the range presented in Fig 3. The range of V_{QDL} and V_{QDR} is constant for each measurement. The slight drift of the avoided crossing upon varying V_{ABS} is owed to cross-capacitance between V_{ABS} and the potential of the QDs.

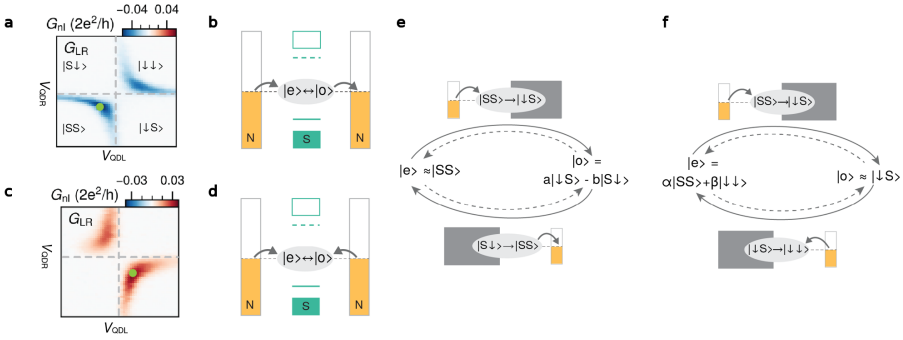

Figure ED7: **Energy diagrams detailing non-local transport.** In CSDs presented in Fig. 3, a clear sign change is observed when changing from the $\Gamma_O > \Gamma_E$ regime to the $\Gamma_O < \Gamma_E$ regime. This can be understood by considering the possible transport cycles that underlie the measured non-local conductance. **(a)** When $\Gamma_O > \Gamma_E$, G_{nl} is observed to be negative in the measured CSDs (see Fig. 3c). **(c)** When $\Gamma_O < \Gamma_E$, the same measurements yield a positive G_{nl} (see Fig. 3a). Horizontal and vertical dashed lines indicate $\mu_R = 0$ and $\mu_L = 0$ respectively. The state of the uncoupled system is labelled in each quadrant. **(b,d)** In such CSD measurements, zero-bias transport can take place when the odd and even ground states are degenerate. For non-local transport to occur, the system can accept a hole/electron from one lead, and relax non-locally to its original state by either (b) donating a hole/electron to the opposite lead, giving rise to negative G_{nl}, or (d) accept a hole/electron from the opposite lead, giving rise to positive G_{nl}. The preferred path is dictated by the quadrant in μ_L, μ_R space where the odd-even degeneracy occurs. **(e)** When μ_L, $\mu_R > 0$ or μ_L,$\mu_R < 0$, the former path is expected to dominate and the resulting G_{nl} will be negative. **(f)** When $\mu_L > 0$ and $\mu_R < 0$ or vice versa, the latter path is expected to dominate and resulting G_{nl} will be positive.

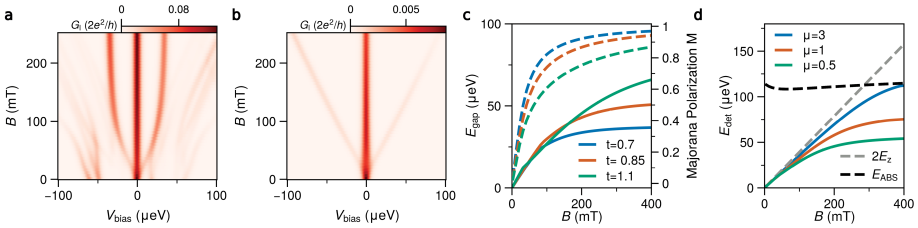

Figure ED8: **Numerical analysis of E_{gap} and E_{det}** Numerical calculations supporting the results presented in Figure 4. Through the procedure detailed in SI-Methods, Majorana sweet spots are obtained and analysed for fields between 0 mT and 300 mT. **(a)** Field evolution of G_{RR} line-traces at each sweet spot, showing the excitations above the ZBPs gradually increasing in energy and then saturating at $\pm 30\,\mu$eV. **(b)** Field evolution of G_{RR} line-traces when QDR detuned by $3\Delta_{\text{ind}}$, showing the excited states increase linearly in energy. From calculations in (a) and (b), E_{gap} and E_{det} are obtained, given by the energy between the lowest even-parity state and second-lowest odd-parity state. **(c)** Extraction of E_{gap} (solid) and the Majorana polarization (dashed), for different values of the tunneling parameter t. In each case $t_{so} = 0.4t$. Larger tunnel coupling results in larger hybridization between ABSs, in turn lowering the MP at a specific magnetic field. **(d)** Extraction of E_{det} for various values of detuning μ_R. In each case the slope at low fields corresponds to $2E_z$ (dashed grey line). The larger the detuning of μ_R, the longer this holds. The dashed black line shows the energy of the ABS E_{ABS}. At large detuning E_{det} will increase linearly with $2E_z$, until becoming of comparable E_{ABS} becomes the lowest energy scale.

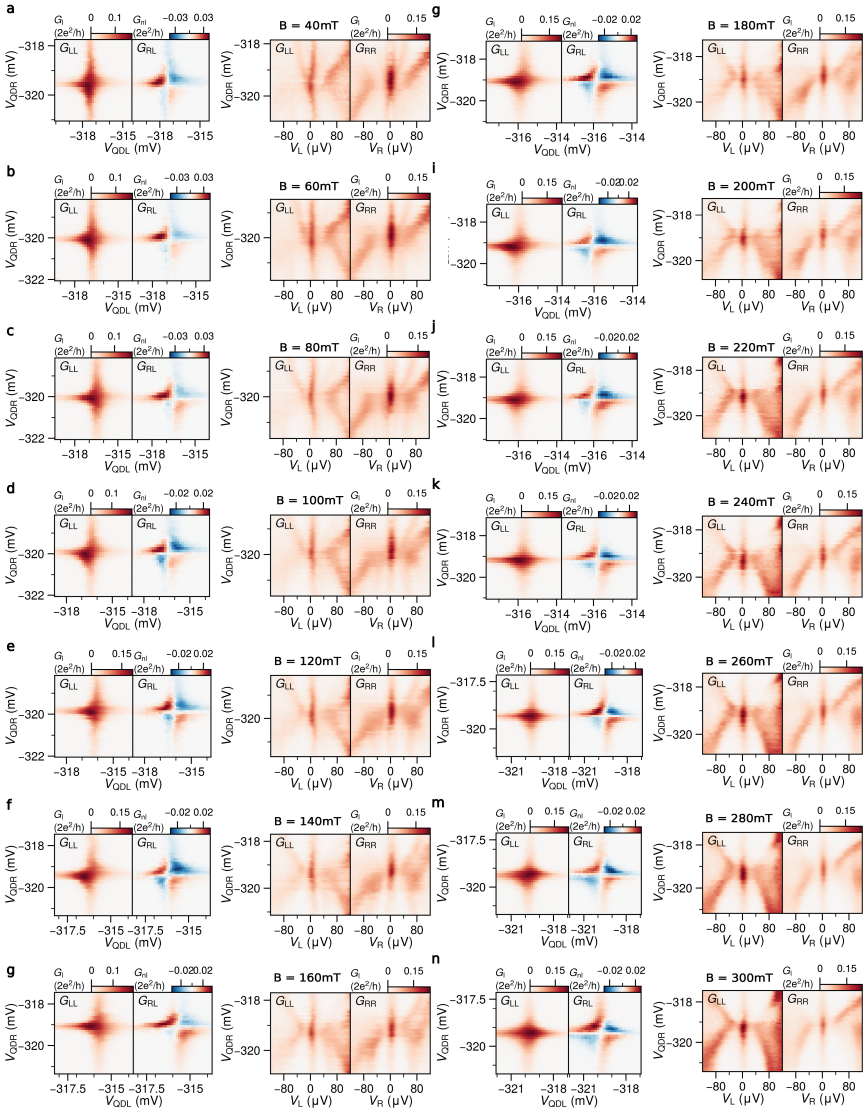

Figure ED9: **Raw datasets for Figure 4h.** Obtained 'sweet spots' at magnetic fields between 0 mT and 300 mT. **(a-i)** CSDs and tunnelling spectroscopy are measured at each sweet spot, where V_{QDR} is detuned. From these measurements E_{det} and E_{gap} are extracted, as described in the main text and in SI-Methods.

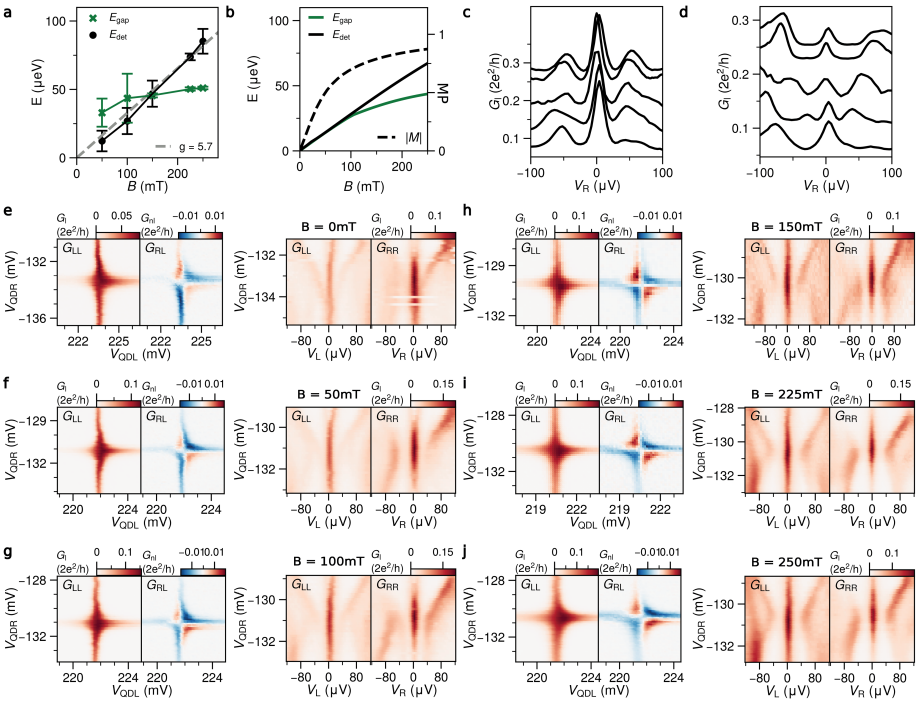

Figure ED10: **Extended datasets supporting Figure 4h.** Reproduction of the main results from Fig. 4, using the orbitals shown in Fig. 3. Data was obtained at 6 different field values B between 0 and 250 mT. At each field V_{ABS} is adjusted to tune to the sweet spot. **a** Extraction of E_{det} and E_{gap}, similar to the analysis presented in Fig. 4l. From a linear for of E_{det} a g-factor of 5.7 is estimated. **(b)** Numerically obtained E_{det} and E_{gap}, using parameters tuned to compare to (a). At 250mT, an estimate of $M \approx 0.9$ is obtained. Extrapolation for comparison to Fig. 4l yields $M \approx 0.92$ at 300mT. **(c)** and **(d)** Waterfall plots highlighting the line-traces used to extract the data in (a). **(e-j)** Raw datasets of CSDs and tunnelling spectroscopy measurements, from which (a-d) is extracted. Datasets at 150 mT and 225 mT datasets are repeated from Fig. 3 and Fig. S5 respectively.

7

Outlook

Life can only be understood backwards; but it must be lived forwards.

Søren Kierkegaard

7.1 A longer Kitaev chain

A two-site chain can host Majorana end modes, but lacks topological protection. Extending the chain length reduces the wave function overlap between end modes, and studies show that the protection of the MZMs against on-site electrostatic noise increases exponentially with the length of the chain [35].

The very next step is to add one more site and build a three-site chain. As straightforward as it may sound, the middle dot compromise the "bulk" of the system where one expect the closing and reopening of the superconducting gap at the system enters the topological phase. In hybrid nanowires, such a geometry has been recently studied with the demonstration of pairwise CAR and ECT between neighboring QD [113] and the observation of greater protection than a two-site chain configuration [114]. In a 2DEG platform, such a device has also been successfully fabricated Chapter 3, where the flexibility of a 2D platform allows us to incorporate a middle normal probe to directly probe the bulk spectrum. Measurements reveal an excitation gap in the bulk, correlated with the stable zero-bias peaks at the edges [49]. Additionally, the phase difference between the two hybrid segments has been extensively studied for its impact on the robustness of the MZMs.

To scale up, a five-site can be realized with the geometry presented in Figure 7.1. First, each QD here is paired with a normal contact, which is challenging to be implemented with hybrid nanowires. The bulk probes not only facilitates the device tune-up but also enables measurements of the spatial dependence of the local DOS. Secondly, each superconducting loop connects neighboring aluminum fingers to allow thee phase control. Since it is hard to control all of them with a global magnetic field, one should consider fabricate flux lines to locally tune the flux with a supplied current. Studies show that controlling the phase difference plays a crucial role in maximizing the excitation gap in the bulk [49]. Lastly, as the number of control gates increases, the parameter space expands rapidly, making automatic device tune-up strategies beneficial. Recent work [115] explores machine-learning based tuning to locate Majorana sweet spots, where the algorithm has shown significantly improved efficiency compared to manual tuning.

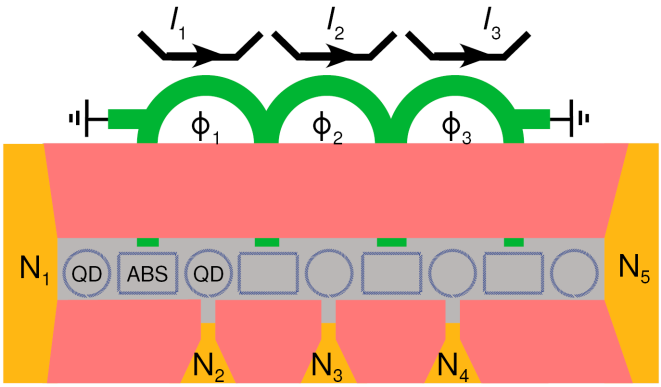

Figure 7.1: **A five-site Kitaev chain.** Three superconducting loops connect the four Al segments next to the ABS region. Flux lines are placed next to the loop for phase-biasing. Every QD can be probed with a nearby normal contact. For clarity the finger gates for the QD and ABS are omitted.

7.2 Parity readout

Beyond achieving a more robust topological phase in an extended Kitaev chain, another key element toward a topological qubit is to develop effective parity readout techniques. Unlike other qubit platforms, MZMs do not have distinct energy levels for the qubit states since they remain degenerate at zero energy. Instead, quantum information can be encoded with the parity of these fermionic modes. As an example, a prototypical parity qubit can be formed in a geometry where two two-site Kitaev chain are coupled with a normal QD [33]. The joint parity of the MZMs, which encodes the state of the qubit, is then inferred from the parity of the middle QD.

One method for parity measurement is parity-to-charge conversion [101]. The basic unit cell is illustrated in Figure 7.2a, with an operational scheme is shown in Figure 7.2b. A step-like tunnel pulse induces the Rabi oscillation between the chain and the dot. By modulating the tunnel strength between the normal dot and the chain, even and odd ground states can be identified based on charge occupation as a function of pulse duration (Figure 7.2c).

A proposed experimental realization based on the 2DEG platform is shown in Figure 7.2d. The left section resembles a standard two-site chain, except that the right depletion gate should be deposited in the second gate layer after placing the two arc-shaped fine gates. Energizing both types of gates creates a 1D-channel to further define a two-site chain, while the two arc-shaped gates control the the tunnel coupling between the QDS and the chain. This setup allows for studying the effect of maximum pulse strength on parity readout and characterizing leakage errors between the zero-energy ground state and higher-energy excited states.

Furthermore, a normal probe is attached to the other end of the QDS for charge occupation readout via dispersive techniques. However, a potential drawback is that pulsing the arc-shaped gates also alters the confinement potential in the Kitaev chain, causing shifts inμ_1 and μ_2. Keeping $\mu_{\max}$ small relative to Δ could mitigate this issue but comes with the cost of extended pulse duration, eventually limited by quasiparticle poisoning time [101].

Another parity readout method involves quantum capacitance measurement. Quantum capacitance is a correction to the capacitance of a system, arising from the extra kinetic energy needed to add charges beyond the electrostatic energy. This occurs because fermions must occupy distinct quantum states with corresponding eigenenergies [116]. Using the device setup shown in Figure 7.2e, it has been shown that the parity can be inferred by measuring the quantum capacitance C_q of a common gate connecting both QDs using RF reflectometry [38]. Here α_i is the lever arm of the superconductor relative to the QD *i*. Unlike the parity-to-charge conversion, this approach does not rely on an auxiliary charge sensor, simplifying the device implementation. The reflected C_q strongly depends on lever arm ratios:

$$C_q^{e,o} = \frac{1 \pm \sin(2\theta)}{4} \frac{\alpha^2}{\Delta}$$

where $\theta = arctan(\alpha_2/\alpha_1)$ and $\alpha = \sqrt{\alpha_1^2 + \alpha_2^2}$ and the dependence is plotted in Figure 7.2f. The readout visibility reaches the maximum when the two levers arms are equal ($\theta = \pi/4$), while it vanishes when one lever arm is zero ($\theta = \pi/2$). Intuitively, a common gate voltage V_g shifts the Fermi levels of both QDs, which will empty the dots and then re-fill them with two electron splitting from a Cooper pair, if the system was in an even ground state ($-\frac{1}{\sqrt{2}}(|00\rangle - |11\rangle)$), In an odd ground state, i.e. $\frac{1}{(\sqrt{2}}|01\rangle - |10\rangle)$,this process is forbidden. When one lever arm is zero, namely the common gate is only coupled to one QD, C_q vanishes because the measurement becomes purely local.

An equivalent measurement is to instead drive the central superconductor lead potential and measure its reflected signal, as shown in Figure 7.2g. The advantage is to avoid the usage of a common gate for both QDs, because the desired charge transitions often do not occur at the same plunger gate voltages. At the same time, one expect exactly the same behavior of C_q as discussed in the common gate case.

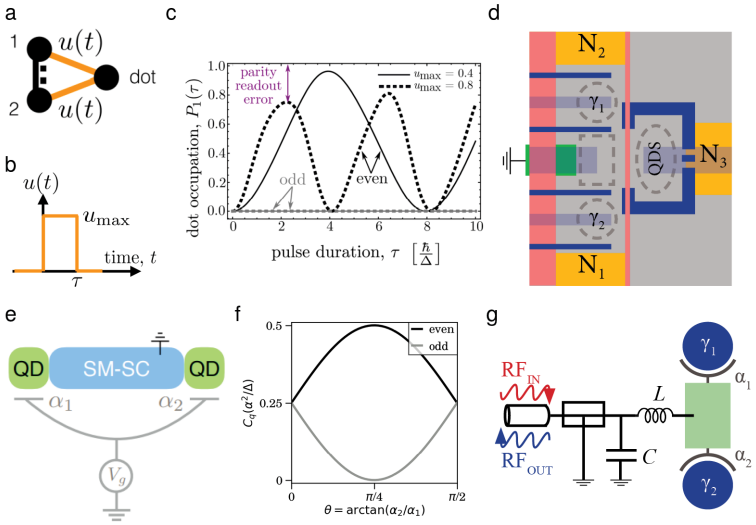

Figure 7.2: **Parity readout methods. (a)** A device structure for parity-to-charge conversion. By applying the pulsing sequence **(b)**, the charge occupation in the normal QD only oscillate as a function of pulse duration if the parity of the Kitaev chain is even. Figures a-c are taken from [101]. **(d)** A proposed geometry to realize **(a)** using the same color-code as in the Chapter 3. The plunger gates are all semi-transparent just for the visibility. Note that the right, thin depletion gate is one gate layer above the two arc-shaped gates. **(e)** A device layout for quantum capacitance C_q measurement. **(f)** The difference in C_q between even and odd ground depends on the ratio between lever arms $\frac{\alpha_2}{\alpha_1}$. **(g)** A equivalent device setup where the LC-resonator is connected directly to the superconducting lead. Figures e-f are adapted from [38].

7.3 Other material platforms

We shall also not forget the material aspect in those studies. This thesis employs InSbAs 2DEGs with an epitaxially grown Al superconductor as the platform for investigating Kitaev chains. While some material properties of this platform make it desirable to study topological superconductivity, InSbAs-based heterostructures has very low thermal budget (limiting available nanofabrication processes, as discussed in Ch. 3) and high-quality growth are not yet widely available to the scientific community. Accordingly, we turn to alternative platforms for proof-of-concept experiments, focusing on two-dimensional systems; 1D hybrid nanowires have been treated extensively elsewhere [53, 117].

InAs–Al hybrid 2DEG platform

A natural candidate is InAs-Al hybrid 2DEGs. Given the similarity of the semiconductor stack, one obvious advantage is that almost all fabrication techniques and design developed here are directly applicable to this more common material platforms. As a more establish material platform, the crucial Al etch process should be more reliable and a higher thermal budget should enable the usage of higher temperature processing, such as 150° ALD, to achieve higher quality of dielectric layer.

We assess the feasibility of implementing a Kitaev chain with hybrid quantum dots by examining some material properties. Starting with a smaller spin–orbit coupling in InAs 2DEGs. A Rashba parameter α of about 120 meVÅ at $n = 3 \times 10^{11}$ cm^{-2} has been reported in deep InAs quantum wells [118], slightly smaller than α of 220 meVÅ in an InSbAs stack with 13% As concentration at same density [29]. SOC will limits the coupling within the even parity section and thus eventually determines the excitation energy to the lowest excited states (the excitation gap in the limit of an infinite chain) [98]. An excitation gap directly improves the protection of MBS against external noise and would be required for operations testing non-Abelian protocols. Thus, the comparatively weaker SOC in InAs may limit the achievable gap size on Kitaev devices InAs–Al platforms. Note that Rashba SOC depends on electric field and crystal orientation, so its impact must be determined experimentally [119].

We now examine the implications of effective g factor in the hybrid QDs. In a spinful implementation the Zeeman splitting in each QD must exceed the effective inter-dot couplings to emulate a spinless Kitaev model [33, 35]. Additionally, Majorana polarization—i.e., the isolation of the two MBSs—increases with Zeeman energy [98]. A larger g therefore reaches a target E_Z at lower B, mitigating the suppression of E_{ABS} in the hybrid section and preserving the chain's excitation gap.

Empirically, the in-plane effective g_{dot} from QD spectroscopy is ~ -20 in CPS devices (weakly coupled, Ch. 5) and ~ -6 in our two-site chains (Ch. 6), both well

below the $g \approx -50$ reported for normal QDs on similar stacks [75]. For comparison, otherwise similar gate-defined dots in InAs 2DEGs (weakly coupled to an ABS) show $g_{\mathrm{dot}} \approx -8.5$ [120]. Despite InAs having a smaller bulk $|g|$ than InSb-based alloys, the *operative* dot $|g|$ in QD devices is set primarily by hybridization and confinement rather than the parent semiconductor. Consequently, InAs remains viable for Kitaev-chain physics. The outlook is to co-optimize g and coupling: increase g_{dot} via geometry/orientation (e.g., elongated dots, orbital tuning) while maintaining strong—but not overhybridized—coupling to maximize the excitation gap.

Ge/SiGe 2DHG heterostructure

The other interesting, emerging candidate is the Ge/SiGe planar heterostructure. Recent demonstrations of hard-gap proximitized devices, together with established spin-qubit readiness, position planar Ge/SiGe as a natural host for hybrid quantum-dot architectures [121]. A decisive advantage over III–V platforms is the weaker hyperfine coupling for holes and the possibility of isotopic purification, which can render devices effectively nuclear-spin-free. As a result, spin lifetime and coherence are not limited by nuclear spins. These features make Ge particularly attractive in experiments where a normal QD needs to be integrated into the setup (Fig. 7.2a), or for detecting entanglement by performing a Bell test with electrons from a Cooper pair [80].

A few material aspects central for hybrid QD-based Kitaev chains. First, induced superconductivity in planar Ge/SiGe 2DHGs can be achieved either via proximity to Al or via annealed Pt contacts (forming PtSiGe). The Al-route has demonstrated a hard induced gap in a shallow QW using ex-situ Al, reaching Δ^* up to 150 μeV. Adding a thin Nb overlayer on Al can further increase the effective gap and improve magnetic-field resilience [122]. However, discrete subgap states which are crucial in Kitaev chains remain to be resolved in this configuration. By contrast, a proximitized QD using an annealed polycrystalline PtSiGe superconductor has been realized [123], with a hard gap $\Delta^* \approx 70\,\mu$eV, an out-of-plane critical field $B_{\mathrm{c},\perp} \approx 0.90 \pm 0.04$ T, and clear YSR spectra. At present, this annealing-approach appears the more mature route for Kitaev-chain devices.

Second, the magnitude and anisotropy of the effective g factor are crucial. For heavy holes in quasi-2D Ge/SiGe one generally finds $|g_\perp| \gg |g_\parallel|$, together with strong electric-field tunability. In [123], an out-of-plane $g_\perp = 1.5 \pm 0.2$ (from YSR splitting) and $g_\perp \approx 4.5$ (from out-of-gap Coulomb diamonds) were reported, along with pronounced anisotropy of the subgap spectra, consistent with hybridization effects. For a target $E_Z = 80\,\mu$eV (Ch. 6), the required field is $B = E_Z/(|g|\mu_B) \approx 0.92$ T for $g = 1.5$, i.e., already comparable to the measured $B_{\mathrm{c},\perp}$. In parallel, spin–orbit coupling in the lowest HH subband is dominated by a *cubic* Rashba term (linear

contributions are negligible), with sub-meV to meV spin splitting at k_F and clear gate tunability; because it scales as k_F^3, operating at lower density suppresses SOC more strongly than in linear-Rashba systems [124, 125]. The precise impact of SOC on transport in hybrid devices remains to be established experimentally.

As a verdict, planar Ge/SiGe remains a strong candidate for QD-based Kitaev chains: hard gaps are available, nuclear-spin noise is minimal, and the near-term task is to engineer a larger g-factor of QD to reach a large Zeeman energy without compromising the induced gap.

A

Calculation of CAR and ECT interference

We report here a brief calculation showing the interference between the two CAR and ECT paths. Since CAR and ECT as second-order processes, their rate can be calculated using Fermi's golden rule

$$W_{i\to f} = \frac{2\pi}{\hbar}\left|\sum_{v}\frac{\langle f|H_T|v\rangle\langle v|H_T|i\rangle}{E_i - E_v}\right|^2 \delta(E_i - E_f) \tag{A.1}$$

where $|i\rangle$, $|v\rangle$ and $|f\rangle$ are the initial, intermediate and final combined state of the system, respectively. The number of intermediate states $|v\rangle$ determines the possible transport pathways. Interference between the possible paths affect the rate because their contributions are summed before taking the absolute value. H_T is the coupling between the ABS and QD and we can expand the Eq. 2.20 as

$$\begin{aligned} H_T = -\Big(& t_L d^\dagger_{L,\uparrow} c_\uparrow + t_L d^\dagger_{L,\downarrow} c_\downarrow + t_R d^\dagger_{R,\uparrow} c_\uparrow + t_R d^\dagger_{R,\downarrow} c_\downarrow + \\ & t_L c^\dagger_\uparrow d_{L,\uparrow} + t_L c^\dagger_\downarrow d_{L,\downarrow} + t_R c^\dagger_\uparrow d_{R,\uparrow} + t_R c^\dagger_\downarrow d_{R,\downarrow} \Big) \end{aligned} \tag{A.2}$$

For consistency we fix the signs with

$$\begin{aligned} |0,\uparrow\downarrow,0\rangle &= c^\dagger_\uparrow c^\dagger_\downarrow |0,0,0\rangle \\ |\uparrow,\uparrow,\downarrow\rangle &= d^\dagger_{L,\uparrow} c^\dagger_\uparrow d^\dagger_{R,\downarrow} |0,0,0\rangle \end{aligned} \tag{A.3}$$

We can now calculate the resulting transition rate for the examples given in the Figure 2.3b and c. Starting with ↑↓-CAR, the transition rate is

$$W = \frac{2\pi}{\hbar} t_L^2 t_R^2 \left|\frac{P_{\text{down}}}{E_0} + \frac{P_{\text{up}}}{E_0}\right|^2 \tag{A.4}$$

A

where P_{i} is the probability of a pathway and its subscript identifies the *doublet* state of the ABS in the intermediate state. In the context of Figure 2.3b, P_{down} is the upper path while P_{up} is the lower path. We can show that

$$\begin{aligned}
P_{\mathrm{down}} &= \langle f|H_T|v\rangle\ \langle v|H_T|i\rangle \\
&= \langle 0,S,0|d_{R,\uparrow}c_\uparrow^\dagger|0,\downarrow,\uparrow\rangle && \langle 0,\downarrow,\uparrow|d_{L,\downarrow}c_\downarrow^\dagger|\downarrow,S,\uparrow\rangle \\
&= \langle 0,S,0|d_{R,\uparrow}c_\uparrow^\dagger c_\downarrow^\dagger d_{R,\uparrow}^\dagger|0,0,0\rangle && \langle 0,\downarrow,\uparrow|d_{L,\downarrow}c_\downarrow^\dagger d_{L,\downarrow}^\dagger(u-vc_\uparrow^\dagger c_\downarrow^\dagger)d_{R,\uparrow}^\dagger|0,0,0\rangle \\
&\overset{!}{=} \langle 0,S,0|c_\uparrow^\dagger c_\downarrow^\dagger d_{R,\uparrow}d_{R,\uparrow}^\dagger|0,0,0\rangle && \langle 0,\downarrow,\uparrow|(-u)d_{L,\downarrow}d_{L,\downarrow}^\dagger c_\downarrow^\dagger d_{R,\uparrow}^\dagger|0,0,0\rangle \\
&= \langle 0,0,0|(u-vc_\uparrow^\dagger c_\downarrow^\dagger)|0,\uparrow\downarrow,0\rangle && -u\langle 0,\downarrow,\uparrow|0,\downarrow,\uparrow\rangle \\
&= (-v)(-u)
\end{aligned} \tag{A.5}$$

note that the exchange of the fermionic operator to the right order results into a global minus sign.

And the other path gives

$$\begin{aligned}
P_{\mathrm{up}} &= \langle f|H_T|v\rangle\ \langle v|H_T|i\rangle \\
&= \langle 0,S,0|d_{L,\downarrow}c_\downarrow^\dagger|\downarrow,\uparrow,0\rangle && \langle\downarrow,\uparrow,0|d_{L,\downarrow}c_\downarrow^\dagger|\downarrow,S,\uparrow\rangle \\
&= \langle 0,S,0|d_{R,\uparrow}c_\uparrow^\dagger c_\downarrow^\dagger d_{R,\uparrow}^\dagger|0,0,0\rangle && \langle\downarrow,\uparrow,0|d_{L,\downarrow}c_\downarrow^\dagger d_{L,\downarrow}^\dagger(u-vc_\uparrow^\dagger c_\downarrow^\dagger)d_{R,\uparrow}^\dagger|0,0,0\rangle \\
&\overset{!}{=} \langle 0,S,0|c_\uparrow^\dagger c_\downarrow^\dagger d_{R,\uparrow}d_{R,\uparrow}^\dagger|0,0,0\rangle && \langle\downarrow,\uparrow,0|(-u)d_{L,\downarrow}d_{L,\downarrow}^\dagger c_\downarrow^\dagger d_{R,\uparrow}^\dagger|0,0,0\rangle \\
&= \langle 0,0,0|(u-vc_\uparrow^\dagger c_\downarrow^\dagger)|0,\uparrow\downarrow,0\rangle && -u\langle\downarrow,\uparrow,0|0,\downarrow,\uparrow\rangle \\
&= (-v)(-u)
\end{aligned} \tag{A.6}$$

Bibliography

[1] Richard P Feynman. Simulating physics with computers. *International Journal of Theoretical Physics*, 21(6):467–488, June 1982.

[2] Ashley Montanaro. Quantum algorithms: an overview. *npj Quantum Information*, 2(1):15023, January 2016.

[3] Rajeev Acharya et al. Quantum error correction below the surface code threshold. *Nature*, 638(8052):920–926, February 2025.

[4] A.Yu. Kitaev. Fault-tolerant quantum computation by anyons, 1997.

[5] A Yu Kitaev. Unpaired Majorana fermions in quantum wires. *Physics-Uspekhi*, 44(10S):131, October 2001.

[6] Ali Yazdani, Felix von Oppen, Bertrand I. Halperin, and Amir Yacoby. Hunting for Majoranas. *Science*, 380(6651):eade0850, 2023.

[7] Elsa Prada, Pablo San-Jose, Michiel W. A. de Moor, Attila Geresdi, Eduardo J. H. Lee, Jelena Klinovaja, Daniel Loss, Jesper Nygård, Ramón Aguado, and Leo P. Kouwenhoven. From Andreev to Majorana bound states in hybrid superconductor–semiconductor nanowires. *Nature Reviews Physics*, 2(10):575–594, October 2020.

[8] Leo Kouwenhoven. Perspective on Majorana bound-states in hybrid superconductor-semiconductor nanowires. *Modern Physics Letters B*, 39(03):2540002, 2025.

[9] Morteza Aghaee, Arun Akkala, Zulfi Alam, et al. InAs-Al hybrid devices passing the topological gap protocol. *Phys. Rev. B*, 107:245423, June 2023.

[10] Richard Hess, Henry F. Legg, Daniel Loss, and Jelena Klinovaja. Trivial Andreev band mimicking topological bulk gap reopening in the nonlocal conductance of long rashba nanowires. *Phys. Rev. Lett.*, 130:207001, May 2023.

[11] Henry F. Legg. Comment on "InAs-Al hybrid devices passing the topological gap protocol", microsoft quantum, phys. rev. b 107, 245423 (2023). *arXiv:2502.19560*, 2025.

[12] Joseph M. Thijssen and Herre S.J. van der Zant. *Charge Transport and Single-Electron Effects in Nanoscale Systems*, chapter 2, pages 37–64. John Wiley & Sons, Ltd, 2010.

[13] Leo P. Kouwenhoven, Charles M. Marcus, Paul L. McEuen, Seigo Tarucha, Robert M. Westervelt, and Ned S. Wingreen. *Electron Transport in Quantum Dots*, pages 105–214. Springer Netherlands, Dordrecht, 1997.

[14] T. Ihn. *Semiconductor Nanostructures: Quantum States and Electronic Transport.* Oxford, 2010.

[15] Yuli V. Nazarov. Circuit theory of Andreev conductance. *Phys. Rev. Lett.*, 73:1420–1423, September 1994.

[16] S. Guéron, H. Pothier, Norman O. Birge, D. Esteve, and M. H. Devoret. Superconducting proximity effect probed on a mesoscopic length scale. *Phys. Rev. Lett.*, 77:3025–3028, September 1996.

[17] Silvano De Franceschi, Leo Kouwenhoven, Christian Schönenberger, and Wolfgang Wernsdorfer. Hybrid superconductor–quantum dot devices. *Nature Nanotechnology*, 5(10):703–711, October 2010.

[18] Anders Jellinggaard. *Quantum Dots Coupled to Superconductors.* PhD thesis, Niels Bohr Institute, 2016.

[19] Guanzhong Wang. *Quantum Dots Coupled to Superconductors.* PhD thesis, Delft University of Technology, 2023.

[20] Michael Tinkham. *Introduction to Superconductivity.* Dover Publications, 2 edition, 2004.

[21] Yuli V. Nazarov and Yaroslav M. Blanter. *Quantum Transport: Introduction to Nanoscience.* Cambridge University Press, 2009.

[22] E. Vecino, A. Martín-Rodero, and A. Levy Yeyati. Josephson current through a correlated quantum level: Andreev states and π junction behavior. *Phys. Rev. B*, 68:035105, July 2003.

[23] Tobias Meng, Serge Florens, and Pascal Simon. Self-consistent description of Andreev bound states in josephson quantum dot devices. *Phys. Rev. B*, 79:224521, June 2009.

[24] Anders Jellinggaard, Kasper Grove-Rasmussen, Morten Hannibal Madsen, and Jesper Nygård. Tuning Yu-Shiba-Rusinov states in a quantum dot. *Phys. Rev. B*, 94, 8 2016.

[25] K. Grove-Rasmussen, G. Steffensen, A. Jellinggaard, M. H. Madsen, R. Avitko, J. Paaske, and J. Nygård. Yu-Shiba-Rusinov screening of spins in double quantum dots. *Nature Communications*, 9, 12 2018.

[26] Francesco Zatelli, David van Driel, Di Xu, Guanzhong Wang, Chun-Xiao Liu, Alberto Bordin, Bart Roovers, Grzegorz P. Mazur, Nick van Loo, Jan C. Wolff, A. Mert Bozkurt, Michael Wimmer, Leo P. Kouwenhoven, Tom Dvir, and More Authors. Robust poor man's Majorana zero modes using Yu-Shiba-Rusinov states. *Nature Communications*, 15(1):7933, 2024.

[27] Chun-Xiao Liu, A. Mert Bozkurt, Francesco Zatelli, Sebastiaan L. D. ten Haaf, Tom Dvir, and Michael Wimmer. Enhancing the excitation gap of a quantum-dot-based Kitaev chain. *Communications Physics*, 7(1):235, July 2024.

[28] L. Hofstetter, S. Csonka, J. Nygård, and C. Schönenberger. Cooper pair splitter realized in a two-quantum-dot Y-junction. *Nature*, 461(7266):960–963, Oct 2009.

[29] Christian M. Möhle, Chung Ting Ke, Qingzhen Wang, Candice Thomas, Di Xiao, Saurabh Karwal, Mario Lodari, Vincent Van De Kerkhof, Ruben Termaat, Geoffrey C. Gardner, Giordano Scappucci, Michael J. Manfra, and Srijit Goswami. InSbAs two-dimensional electron gases as a platform for topological superconductivity. *Nano Lett.*, 21:9990–9996, 12 2021.

[30] Chun-Xiao Liu, Guanzhong Wang, Tom Dvir, and Michael Wimmer. Tunable superconducting coupling of quantum dots via Andreev bound states in semiconductor-superconductor nanowires. *Phys. Rev. Lett.*, 129, 12 2022.

[31] Alberto Bordin, Guanzhong Wang, Chun-Xiao Liu, Sebastiaan L. D. ten Haaf, Nick van Loo, Grzegorz P. Mazur, Di Xu, David van Driel, Francesco Zatelli, Sasa Gazibegovic, Ghada Badawy, Erik P. A. M. Bakkers, Michael Wimmer, Leo P. Kouwenhoven, and Tom Dvir. Tunable crossed Andreev reflection and elastic cotunneling in hybrid nanowires. *Phys. Rev. X*, 13:031031, September 2023.

[32] Ramón Aguado. Majorana quasiparticles in condensed matter. *La Rivista del Nuovo Cimento*, 40(11):523–593, 2017.

[33] Martin Leijnse and Karsten Flensberg. Parity qubits and poor man's Majorana bound states in double quantum dots. *Phys. Rev. B*, 86, 10 2012.

[34] A. Mert Bozkurt, Sebastian Miles, Sebastiaan L. D. ten Haaf, Chun-Xiao Liu, Fabian Hassler, and Michael Wimmer. Interaction-induced strong zero

modes in short quantum dot chains with time-reversal symmetry. *SciPost Physics*, 18(6), June 2025.

[35] Jay D Sau and S Das Sarma. Realizing a robust practical Majorana chain in a quantum-dot-superconductor linear array. *Nature communications*, 3(1):964, July 2012.

[36] David Aasen, Michael Hell, Ryan V. Mishmash, Andrew Higginbotham, Jeroen Danon, Martin Leijnse, Thomas S. Jespersen, Joshua A. Folk, Charles M. Marcus, Karsten Flensberg, and Jason Alicea. Milestones toward Majorana-based quantum computing. *Phys. Rev. X*, 6:031016, August 2016.

[37] Torsten Karzig, Christina Knapp, Roman M. Lutchyn, Parsa Bonderson, Matthew B. Hastings, Chetan Nayak, Jason Alicea, Karsten Flensberg, Stephan Plugge, Yuval Oreg, Charles M. Marcus, and Michael H. Freedman. Scalable designs for quasiparticle-poisoning-protected topological quantum computation with Majorana zero modes. *Phys. Rev. B*, 95, 6 2017.

[38] Chun-Xiao Liu, Haining Pan, F. Setiawan, Michael Wimmer, and Jay D. Sau. Fusion protocol for Majorana modes in coupled quantum dots. *Phys. Rev. B*, 108:085437, August 2023.

[39] Georg W. Winkler, QuanSheng Wu, Matthias Troyer, Peter Krogstrup, and Alexey A. Soluyanov. Topological phases in $InAs_{1-x}Sb_x$: From novel topological semimetal to Majorana wire. *Phys. Rev. Lett.*, 117:076403, August 2016.

[40] William Mayer, William F. Schiela, Joseph Yuan, Mehdi Hatefipour, Wendy L. Sarney, Stefan P. Svensson, Asher C. Leff, Tiago Campos, Kaushini S. Wickramasinghe, Matthieu C. Dartiailh, Igor Žutić, and Javad Shabani. Superconducting proximity effect in InAsSb surface quantum wells with in situ Al contacts. *ACS Applied Electronic Materials*, 2(8):2351–2356, August 2020.

[41] S. Metti, C. Thomas, D. Xiao, and M. J. Manfra. Spin-orbit coupling and electron scattering in high-quality $insb_{1-x}as_x$ quantum wells. *Phys. Rev. B*, 106:165304, October 2022.

[42] Fabrizio Nichele, Asbjørn C. C. Drachmann, Alexander M. Whiticar, Eoin C. T. O'Farrell, Henri J. Suominen, Antonio Fornieri, Tian Wang, Geoffrey C. Gardner, Candice Thomas, Anthony T. Hatke, Peter Krogstrup, Michael J. Manfra, Karsten Flensberg, and Charles M. Marcus. Scaling of Majorana zero-bias conductance peaks. *Phys. Rev. Lett.*, 119:136803, September 2017.

[43] C. Thomas, R. E. Diaz, J. H. Dycus, M. E. Salmon, R. E. Daniel, T. Wang, G. C. Gardner, and M. J. Manfra. Toward durable Al-InSb hybrid heterostructures via epitaxy of 2ml interfacial InAs screening layers. *Phys. Rev. Mater.*, 3:124202, December 2019.

[44] Christian M. Möhle. *Induced superconductivity in antimony-based two-dimensional electron gases.* PhD thesis, Delft University of Technology, 2023.

[45] H. J. Suominen, M. Kjaergaard, A. R. Hamilton, J. Shabani, C. J. Palmstrøm, C. M. Marcus, and F. Nichele. Zero-energy modes from coalescing Andreev states in a two-dimensional semiconductor-superconductor hybrid platform. *Phys. Rev. Lett.*, 119:176805, October 2017.

[46] Haining Pan and S. Das Sarma. Physical mechanisms for zero-bias conductance peaks in Majorana nanowires. *Phys. Rev. Res.*, 2:013377, March 2020.

[47] R. Hanson, L. P. Kouwenhoven, J. R. Petta, S. Tarucha, and L. M. K. Vandersypen. Spins in few-electron quantum dots. *Rev. Mod. Phys.*, 79:1217–1265, October 2007.

[48] X. Croot, S. Pauka, M. C. Jarratt, H. Lü, A. C. Gossard, J. Watson, G. C. Gardner, S. Fallahi, M. J. Manfra, and D. Reilly. Gate-sensing charge pockets in the semiconductor-qubit environment. *Physical Review Applied*, 11, 2019.

[49] Sebastiaan L. D. ten Haaf, Yining Zhang, Qingzhen Wang, Alberto Bordin, Chun-Xiao Liu, Ivan Kulesh, Vincent P. M. Sietses, Christian G. Prosko, Di Xiao, Candice Thomas, Michael J. Manfra, Michael Wimmer, and Srijit Goswami. Observation of edge and bulk states in a three-site kitaev chain. *Nature*, 641(8064):890–895, May 2025.

[50] Tom Dvir, Guanzhong Wang, Nick van Loo, Chun Xiao Liu, Grzegorz P. Mazur, Alberto Bordin, Sebastiaan L.D. ten Haaf, Ji Yin Wang, David van Driel, Francesco Zatelli, Xiang Li, Filip K. Malinowski, Sasa Gazibegovic, Ghada Badawy, Erik P.A.M. Bakkers, Michael Wimmer, and Leo P. Kouwenhoven. Realization of a minimal Kitaev chain in coupled quantum dots. *Nature*, 614:445–450, 2 2023.

[51] Roman M. Lutchyn, Jay D. Sau, and S. Das Sarma. Majorana fermions and a topological phase transition in semiconductor-superconductor heterostructures. *Phys. Rev. Lett.*, 105:077001, August 2010.

[52] Yuval Oreg, Gil Refael, and Felix von Oppen. Helical liquids and Majorana bound states in quantum wires. *Phys. Rev. Lett.*, 105:177002, October 2010.

[53] Nick Van Loo. *Shadow-wall lithography as a novel approach to Majorana devices.* PhD thesis, Delft University of Technology, 2023.

[54] Anna Grivnin, Ella Bor, Moty Heiblum, Yuval Oreg, and Hadas Shtrikman. Concomitant opening of a bulk-gap with an emerging possible Majorana zero mode. *Nature Communications*, 10:1940, 04 2019.

[55] Ji-Yin Wang, Nick van Loo, Grzegorz P. Mazur, Vukan Levajac, Filip K. Malinowski, Mathilde Lemang, Francesco Borsoi, Ghada Badawy, Sasa Gazibegovic, Erik P. A. M. Bakkers, Marina Quintero-Pérez, Sebastian Heedt, and Leo P. Kouwenhoven. Parametric exploration of zero-energy modes in three-terminal InSb-Al nanowire devices. *Phys. Rev. B*, 106:075306, August 2022.

[56] Nick van Loo, Grzegorz P. Mazur, Tom Dvir, Guanzhong Wang, Robin C. Dekker, Ji-Yin Wang, Mathilde Lemang, Cristina Sfiligoj, Alberto Bordin, David van Driel, Ghada Badawy, Sasa Gazibegovic, Erik P. A. M. Bakkers, and Leo P. Kouwenhoven. Electrostatic control of the proximity effect in the bulk of semiconductor-superconductor hybrids. *Nature Communications*, 14(1):3325, 2023.

[57] Chetan Nayak, Steven H. Simon, Ady Stern, Michael Freedman, and Sankar Das Sarma. Non-Abelian anyons and topological quantum computation. *Rev. Mod. Phys.*, 80:1083–1159, September 2008.

[58] Tudor D. Stanescu, Sumanta Tewari, Jay D. Sau, and S. Das Sarma. To close or not to close: The fate of the superconducting gap across the topological quantum phase transition in Majorana-carrying semiconductor nanowires. *Phys. Rev. Lett.*, 109:266402, December 2012.

[59] R. M. Lutchyn, E. P. A. M. Bakkers, L. P. Kouwenhoven, P. Krogstrup, C. M. Marcus, and Y. Oreg. Majorana zero modes in superconductor–semiconductor heterostructures. *Nature Reviews Materials*, 3(5):52–68, May 2018.

[60] G. Kells, D. Meidan, and P. W. Brouwer. Near-zero-energy end states in topologically trivial spin-orbit coupled superconducting nanowires with a smooth confinement. *Phys. Rev. B*, 86:100503, Sep 2012.

[61] Elsa Prada, Pablo San-Jose, and Ramón Aguado. Transport spectroscopy of NS nanowire junctions with Majorana fermions. *Phys. Rev. B*, 86(18):180503, November 2012.

[62] Diego Rainis, Luka Trifunovic, Jelena Klinovaja, and Daniel Loss. Towards a realistic transport modeling in a superconducting nanowire with Majorana fermions. *Phys. Rev. B*, 87(2):024515, 2013.

[63] Dibyendu Roy, Nilanjan Bondyopadhaya, and Sumanta Tewari. Topologically trivial zero-bias conductance peak in semiconductor Majorana wires from boundary effects. *Phys. Rev. B*, 88(2):020502(R), 2013.

[64] Fernando Peñaranda, Ramón Aguado, Pablo San-Jose, and Elsa Prada. Quantifying wave-function overlaps in inhomogeneous Majorana nanowires. *Phys. Rev. B*, 98(23):235406, 2018.

[65] Adriaan Vuik, Bas Nijholt, Anton R. Akhmerov, and Michael Wimmer. Reproducing topological properties with quasi-Majorana states. *SciPost Phys.*, 7:061, 2019.

[66] T. Ö. Rosdahl, A. Vuik, M. Kjaergaard, and A. R. Akhmerov. Andreev rectifier: A nonlocal conductance signature of topological phase transitions. *Phys. Rev. B*, 97:045421, January 2018.

[67] D. Puglia, E. A. Martinez, G. C. Ménard, A. Pöschl, S. Gronin, G. C. Gardner, R. Kallaher, M. J. Manfra, C. M. Marcus, A. P. Higginbotham, and L. Casparis. Closing of the induced gap in a hybrid superconductor-semiconductor nanowire. *Phys. Rev. B*, 103:235201, June 2021.

[68] Andreas Pöschl, Alisa Danilenko, Deividas Sabonis, Kaur Kristjuhan, Tyler Lindemann, Candice Thomas, Michael J. Manfra, and Charles M. Marcus. Nonlocal conductance spectroscopy of Andreev bound states in gate-defined InAs/Al nanowires. *Phys. Rev. B*, 106:L241301, December 2022.

[69] Vukan Levajac, Ji-Yin Wang, Cristina Sfiligoj, Mathilde Lemang, Jan Cornelis Wolff, Alberto Bordin, Ghada Badawy, Sasa Gazibegovic, Erik P A M Bakkers, and Leo P Kouwenhoven. Subgap spectroscopy along hybrid nanowires by nm-thick tunnel barriers. *Nature Communications*, 14(1):6647, October 2023.

[70] Tudor D. Stanescu and Sankar Das Sarma. Building topological quantum circuits: Majorana nanowire junctions. *Phys. Rev. B*, 97:045410, January 2018.

[71] Andreas Pöschl, Alisa Danilenko, Deividas Sabonis, Kaur Kristjuhan, Tyler Lindemann, Candice Thomas, Michael J. Manfra, and Charles M. Marcus. Nonlocal signatures of hybridization between quantum dot and Andreev bound states. *Phys. Rev. B*, 106:L161301, October 2022.

[72] Marco Valentini, Fernando Peñaranda, Andrea Hofmann, Matthias Brauns, Robert Hauschild, Peter Krogstrup, Pablo San-Jose, Elsa Prada, Ramón Aguado, and Georgios Katsaros. Nontopological zero-bias peaks in full-shell nanowires induced by flux-tunable Andreev states. *Science*, 373(6550):82–88, 2021.

[73] Michiel W A de Moor, Jouri D S Bommer, Di Xu, Georg W Winkler, Andrey E Antipov, Arno Bargerbos, Guanzhong Wang, Nick van Loo, Roy L M Op het Veld, Sasa Gazibegovic, Diana Car, John A Logan, Mihir Pendharkar, Joon Sue Lee, Erik P A M Bakkers, Chris J Palmstrøm, Roman M Lutchyn, Leo P Kouwenhoven, and Hao Zhang. Electric field tunable superconductor-semiconductor coupling in Majorana nanowires. *New Journal of Physics*, 20(10):103049, October 2018.

[74] S. Vaitiekėnas, M.-T. Deng, J. Nygård, P. Krogstrup, and C. M. Marcus. Effective g factor of subgap states in hybrid nanowires. *Phys. Rev. Lett.*, 121:037703, July 2018.

[75] S. Metti, C. Thomas, and M. J. Manfra. Electronic g factor and tunable spin-orbit coupling in a gate-defined InSbAs quantum dot. *Phys. Rev. B*, 108:235306, December 2023.

[76] Seongjin Ahn, Haining Pan, Benjamin Woods, Tudor D. Stanescu, and Sankar Das Sarma. Estimating disorder and its adverse effects in semiconductor Majorana nanowires. *Phys. Rev. Mater.*, 5:124602, December 2021.

[77] Esteban A. Martinez, Andreas Poschl, Esben Bork Hansen, May An Y. van de Poll, Saulius Vaitiekėnas, Andrew P. Higginbotham, and Lucas Casparis. Measurement circuit effects in three-terminal electrical transport measurements. *arXiv:2104.02671*, 2021.

[78] Patrik Recher, Eugene V. Sukhorukov, and Daniel Loss. Andreev tunneling, Coulomb blockade, and resonant transport of nonlocal spin-entangled electrons. *Phys. Rev. B*, 63:165314, April 2001.

[79] Nikolai M. Chtchelkatchev, Gianni Blatter, Gordey B. Lesovik, and Thierry Martin. Bell inequalities and entanglement in solid-state devices. *Phys. Rev. B*, 66:161320, October 2002.

[80] Bernd Braunecker, Pablo Burset, and Alfredo Levy Yeyati. Entanglement detection from conductance measurements in carbon nanotube Cooper pair splitters. *Phys. Rev. Lett.*, 111:136806, September 2013.

[81] Waldemar Kłobus, Andrzej Grudka, Andreas Baumgartner, Damian Tomaszewski, Christian Schönenberger, and Jan Martinek. Entanglement witnessing and quantum cryptography with nonideal ferromagnetic detectors. *Phys. Rev. B*, 89:125404, March 2014.

[82] F. Brange, O. Malkoc, and P. Samuelsson. Minimal entanglement witness from electrical current correlations. *Phys. Rev. Lett.*, 118:036804, January 2017.

[83] Piotr Busz, Damian Tomaszewski, and Jan Martinek. Spin correlation and entanglement detection in Cooper pair splitters by current measurements using magnetic detectors. *Phys. Rev. B*, 96:064520, August 2017.

[84] J. Gramich, A. Baumgartner, and C. Schönenberger. Andreev bound states probed in three-terminal quantum dots. *Phys. Rev. B*, 96:195418, November 2017.

[85] Jeroen Danon, Anna Birk Hellenes, Esben Bork Hansen, Lucas Casparis, Andrew P. Higginbotham, and Karsten Flensberg. Nonlocal conductance spectroscopy of Andreev bound states: Symmetry relations and bcs charges. *Phys. Rev. Lett.*, 124:036801, January 2020.

[86] R. S. Deacon, Y. Tanaka, A. Oiwa, R. Sakano, K. Yoshida, K. Shibata, K. Hirakawa, and S. Tarucha. Kondo-enhanced Andreev transport in single self-assembled InAs quantum dots contacted with normal and superconducting leads. *Phys. Rev. B*, 81:121308, March 2010.

[87] J. Gramich, A. Baumgartner, and C. Schönenberger. Resonant and inelastic Andreev tunneling observed on a carbon nanotube quantum dot. *Phys. Rev. Lett.*, 115:216801, November 2015.

[88] J. Schindele, A. Baumgartner, and C. Schönenberger. Near-unity Cooper pair splitting efficiency. *Phys. Rev. Lett.*, 109:157002, 10 2012.

[89] Guanzhong Wang, Tom Dvir, Grzegorz P. Mazur, Chun-Xiao Liu, Nick van Loo, Sebastiaan L. D. ten Haaf, Alberto Bordin, Sasa Gazibegovic, Ghada Badawy, Erik P. A. M. Bakkers, Michael Wimmer, and Leo P. Kouwenhoven. Singlet and triplet Cooper pair splitting in hybrid superconducting nanowires. *Nature*, 612(7940):448–453, December 2022.

[90] W. G. van der Wiel, S. De Franceschi, J. M. Elzerman, T. Fujisawa, S. Tarucha, and L. P. Kouwenhoven. Electron transport through double quantum dots. *Rev. Mod. Phys.*, 75:1–22, December 2002.

[91] S. Nadj-Perge, S. M. Frolov, J. W.W. Van Tilburg, J. Danon, Yu V. Nazarov, R. Algra, E. P.A.M. Bakkers, and L. P. Kouwenhoven. Disentangling the effects of spin-orbit and hyperfine interactions on spin blockade. *Phys. Rev. B*, 81:201305, 5 2010.

[92] J. Danon and Yu V. Nazarov. Pauli spin blockade in the presence of strong spin-orbit coupling. *Phys. Rev. B*, 80:041301, 8 2009.

[93] Arunav Bordoloi, Valentina Zannier, Lucia Sorba, Christian Schönenberger, and Andreas Baumgartner. Spin cross-correlation experiments in an electron entangler. *Nature*, 612(7940):454–458, December 2022.

[94] M. C. Hels, B. Braunecker, K. Grove-Rasmussen, and J. Nygård. Noncollinear spin-orbit magnetic fields in a carbon nanotube double quantum dot. *Phys. Rev. Lett.*, 117:276802, December 2016.

[95] Jason Alicea, Yuval Oreg, Gil Refael, Felix von Oppen, and Matthew P. A. Fisher. Non-Abelian statistics and topological quantum information processing in 1D wire networks. *Nature Physics*, 7(5):412–417, May 2011.

[96] Christian M. Möhle, Prasanna K. Rout, Nayan A. Jainandunsing, Dibyendu Kuiri, Chung Ting Ke, Di Xiao, Candice Thomas, Michael J. Manfra, Michał P. Nowak, and Srijit Goswami. Controlling Andreev bound states with the magnetic vector potential. *Nano Letters*, 22(21):8601–8607, 2022.

[97] Ion C. Fulga, Arbel Haim, Anton R. Akhmerov, and Yuval Oreg. Adaptive tuning of Majorana fermions in a quantum dot chain. *New Journal of Physics*, 15, 4 2013.

[98] Athanasios Tsintzis, Rubén Seoane Souto, and Martin Leijnse. Creating and detecting poor man's Majorana bound states in interacting quantum dots. *Phys. Rev. B*, 106:L201404, November 2022.

[99] Athanasios Tsintzis, Rubén Seoane Souto, Karsten Flensberg, Jeroen Danon, and Martin Leijnse. Majorana qubits and non-abelian physics in quantum dot–based minimal kitaev chains. *PRX Quantum*, 5(1), February 2024.

[100] Chun-Xiao Liu, Jay D. Sau, Tudor D. Stanescu, and S. Das Sarma. Andreev bound states versus Majorana bound states in quantum dot-nanowire-superconductor hybrid structures: Trivial versus topological zero-bias conductance peaks. *Phys. Rev. B*, 96:075161, August 2017.

[101] Gábor Széchenyi and András Pályi. Parity-to-charge conversion for readout of topological Majorana qubits. *Phys. Rev. B*, 101:235441, June 2020.

[102] Péter Boross and András Pályi. Braiding-based quantum control of a Majorana qubit built from quantum dots. *Physical Review B*, 109(12), March 2024.

[103] N. Sedlmayr and C. Bena. Visualizing Majorana bound states in one and two dimensions using the generalized Majorana polarization. *Phys. Rev. B*, 92:115115, September 2015.

[104] K. Grove-Rasmussen, H. I. Jørgensen, B. M. Andersen, J. Paaske, T. S. Jespersen, J. Nygård, K. Flensberg, and P. E. Lindelof. Superconductivity-enhanced bias spectroscopy in carbon nanotube quantum dots. *Phys. Rev. B*, 79, 4 2009.

[105] R. S. Deacon, Y. Tanaka, A. Oiwa, R. Sakano, K. Yoshida, K. Shibata, K. Hirakawa, and S. Tarucha. Tunneling spectroscopy of Andreev energy levels in a quantum dot coupled to a superconductor. *Phys. Rev. Lett.*, 104, 2 2010.

[106] Eduardo J.H. Lee, Xiaocheng Jiang, Manuel Houzet, Ramon Aguado, Charles M. Lieber, and Silvano De Franceschi. Spin-resolved Andreev levels and parity crossings in hybrid superconductor-semiconductor nanostructures. *Nature Nanotechnology*, 9:79–84, 2014.

[107] Qingzhen Wang, Sebastiaan L. D. ten Haaf, Ivan Kulesh, Di Xiao, Candice Thomas, Michael J. Manfra, and Srijit Goswami. Triplet correlations in Cooper pair splitters realized in a two-dimensional electron gas. *Nature Communications*, 14(1):4876, August 2023.

[108] Li Dai, Watson Kuo, and Ming-Chiang Chung. Extracting entangled qubits from Majorana fermions in quantum dot chains through the measurement of parity. *Scientific Reports*, 5(1):11188, June 2015.

[109] D. Michel Pino, Rubén Seoane Souto, and Ramón Aguado. Minimal Kitaev-transmon qubit based on double quantum dots. *Physical Review B*, 109(7), February 2024.

[110] David J. Clarke. Experimentally accessible topological quality factor for wires with zero energy modes. *Phys. Rev. B*, 96:201109, November 2017.

[111] Elsa Prada, Ramón Aguado, and Pablo San-Jose. Measuring Majorana nonlocality and spin structure with a quantum dot. *Phys. Rev. B*, 96:085418, August 2017.

[112] Rubén Seoane Souto, Athanasios Tsintzis, Martin Leijnse, and Jeroen Danon. Probing majorana localization in minimal kitaev chains through a quantum dot. *Physical Review Research*, 5(4), November 2023.

[113] Alberto Bordin, Xiang Li, David van Driel, Jan Cornelis Wolff, Qingzhen Wang, Sebastiaan L. D. ten Haaf, Guanzhong Wang, Nick van Loo, Leo P. Kouwenhoven, and Tom Dvir. Crossed Andreev reflection and elastic cotunneling in three quantum dots coupled by superconductors. *Phys. Rev. Lett.*, 132:056602, Feb 2024.

[114] Alberto Bordin, Chun-Xiao Liu, Tom Dvir, Francesco Zatelli, Sebastiaan L. D. ten Haaf, David van Driel, Guanzhong Wang, Nick van Loo, Yining Zhang, Jan Cornelis Wolff, Thomas Van Caekenberghe, Ghada Badawy, Sasa Gazibegovic, Erik P. A. M. Bakkers, Michael Wimmer, Leo P. Kouwenhoven, and Grzegorz P. Mazur. Enhanced Majorana stability in a three-site Kitaev chain. *Nature Nanotechnology*, 20(6):726–731, March 2025.

[115] David van Driel, Rouven Koch, Vincent P. M. Sietses, Sebastiaan L. D. ten Haaf, Chun-Xiao Liu, Francesco Zatelli, Bart Roovers, Alberto Bordin, Nick van Loo, Guanzhong Wang, Jan Cornelis Wolff, Grzegorz P. Mazur, Tom Dvir, Ivan Kulesh, Qingzhen Wang, A. Mert Bozkurt, Sasa Gazibegovic, Ghada Badawy, Erik P. A. M. Bakkers, Michael Wimmer, Srijit Goswami, Jose L. Lado, Leo P. Kouwenhoven, and Eliska Greplova. Cross-platform autonomous control of minimal Kitaev chains. *arXiv:2405.04596*, 2024.

[116] Florian Vigneau, Federico Fedele, Anasua Chatterjee, David Reilly, Ferdinand Kuemmeth, M. Fernando Gonzalez-Zalba, Edward Laird, and Natalia Ares. Probing quantum devices with radio-frequency reflectometry. *Applied Physics Reviews*, 10(2):021305, 02 2023.

[117] Alberto Bordin. *Engineering the Kitaev chain.* PhD thesis, Delft University of Technology, 2025.

[118] A. T. Hatke, T. Wang, C. Thomas, G. C. Gardner, and M. J. Manfra. Mobility in excess of $10^6 \mathrm{cm}^2/\mathrm{Vs}$ in InAs quantum wells grown on lattice mismatched InP substrates. *Applied Physics Letters*, 111(14), 2017.

[119] Roland Winkler. *Spin-orbit Coupling Effects in Two-Dimensional Electron and Hole Systems.* Springer-Verlag: Berlin, 2003.

[120] Alisa Danilenko, Andreas Pöschl, Deividas Sabonis, Vasileios Vlachodimitropoulos, Candice Thomas, Michael J. Manfra, and Charles M. Marcus. Spin spectroscopy of a hybrid superconducting nanowire using side-coupled quantum dots. *Phys. Rev. B*, 108:054514, August 2023.

[121] Giordano Scappucci, Christoph Kloeffel, Floris A. Zwanenburg, Daniel Loss, Maksym Myronov, Jian-Jun Zhang, Silvano De Franceschi, Georgios Katsaros,

and Menno Veldhorst. The germanium quantum information route. *Nature Reviews Materials*, 6(10), 2020.

[122] Kushagra Aggarwal, Andrea Hofmann, Daniel Jirovec, Ivan Prieto, Amir Sammak, Marc Botifoll, Sara Martí-Sánchez, Menno Veldhorst, Jordi Arbiol, Giordano Scappucci, Jeroen Danon, and Georgios Katsaros. Enhancement of proximity-induced superconductivity in a planar Ge hole gas. *Phys. Rev. Res.*, 3:L022005, April 2021.

[123] Lazar Lakic, William I. L. Lawrie, David van Driel, Lucas E. A. Stehouwer, Yao Su, Menno Veldhorst, Giordano Scappucci, Ferdinand Kuemmeth, and Anasua Chatterjee. A quantum dot in germanium proximitized by a superconductor. *Nature Materials*, 24(4):552–558, April 2025. Publisher: Nature Publishing Group.

[124] Rai Moriya, Kentarou Sawano, Yusuke Hoshi, Satoru Masubuchi, Yasuhiro Shiraki, Andreas Wild, Christian Neumann, Gerhard Abstreiter, Dominique Bougeard, Takaaki Koga, and Tomoki Machida. Cubic rashba spin-orbit interaction of a two-dimensional hole gas in a strained-Ge/SiGe quantum well. *Phys. Rev. Lett.*, 113:086601, August 2014.

[125] C.-T. Chou, N. T. Jacobson, J. E. Moussa, A. D. Baczewski, Y. Chuang, C.-Y. Liu, J.-Y. Li, and T. M. Lu. Weak anti-localization of two-dimensional holes in germanium beyond the diffusive regime. *Nanoscale*, 10:20559–20564, 2018.

Acknowledgments

My PhD journey has been a long one, filled with ups and downs. I want to use this space to thank all the people who helped me along the way and made the path not only possible, but also memorable.

First of all, thank you **Srijit** for taking me on as a PhD student. You've been a great team leader, always bringing the group together with activities that left me with many good memories (including those darts times and debates over random topics). I've benefited enormously from your hands-on supervision throughout. Especially I appreciate your patience and support during the final, long stretch of the PhD. I also want to thank **Leo**, for his feedback over the years. And my gratitude goes to **Yuli, Sander, Ferdinand, Christian, and Giordano** for reviewing my thesis and being part of the committee..

Bas, it's been such a pleasure working with you. I'm really glad you joined our group after showing your talent during your master's thesis. You taught me so much physics, and our joint work was a true highlight of my PhD. I will always remember your kindness and support — and that unforgettable March Meeting road trip! Best of luck with the writing and the bright future ahead. **Ivan**, so many of my cleanroom memories (and traumas) are with you. You've helped me a lot from cooling down Janis fridges to pushing me through the final thesis sprint. I was constantly surprised by how quickly you picked up new skills and turned ideas into practice — a trait that will surely make you excel at ASML! **Yining**, thank you for being my paranymph. I'm really glad you stayed with hybrid physics after a rough master project. I admire your calmness and emotional steadiness, and your passion for Zelda eventually made me give it a try (though it's not my game). I hope you'll get that bigger flat along the river, a second cat soon-ish.

Christian M, I really appreciated all the time we spent together in the cleanroom and lab. I hope to visit you in Sydney one day — it looks like you've also become quite an experienced runner! **Ting**, thank you for all your help over the years. Your passion and deep curiosity for physics have always been inspiring to me, and I hope to visit you one day as a Qblox expert in Academic Sinica. **Saurabh**, you've always known how to laugh things off — inside or outside the cleanroom. I've appreciated your career advice, and I wish you all the best as you continue your journey at TNO. **Fokko**, thank you for guiding me at the very beginning of my PhD and you have taught me the importance of keeping good logs for both fabrication and measurements. Too bad the SNAKE project did not work out before

you left for your graphene journey. I am also grateful for your introduction to Qblox last year! I want to thank **Wietze**, **Sebas**, **DJ**, **Rebecca**, **Prasanna**, **Nikos** and other 2D topo members for the many coffee chats and discussions. We may not have chosen the easiest path in the field, but I hope each of you finds your way through the journey and grows as much as you wish along the way.

Within QuRe, **Di**, thank you for taking me in as a master's student back in 2017 and for introducing me to the restaurants and museums around town. I'll always remember the piano lesson (a pity we didn't continue!). To me you are an example of living fully in the present, and fueling everything with seemingly endless curiosity and imagination. I've always valued your advice and guidance whenever I was in doubt or facing a dilemma. All the best with your career in Q. Motion. **Lin**, you are a natural storyteller — as I've often said, you really should write a book! It's wonderful to see you've grown stronger over the years and are finding your inner peace now after all. I wish you all the best going forward with you enjoying your career. **Nick**, thank you for the countless coffee chats. Your cheerful character always made it easy for me to reach out. A special thanks as well for pushing me to finish the Multiprobe paper, together with **Greg**. **Greg**, your humor and charm left a big impression, and I wish you the best with your new lab in the US. **Alberto**, your ever-enthusiastic attitude toward life has been truly inspiring! Best of luck with your startups and your academic career. **Chun-Xiao**, thank you for many discussions we had about the physics and for writing the LDOS script for the multiprobe in the end. I wish you all the best in building your new group. **Tom** you have been an amazing and smart physicist with strong intuition. I learned a lot for all the discussions with you and wish you all the best at QM. **Yang**, it's always fun hanging out with you — and thanks again for hosting me during my short stay in Stuttgart. Running in the forest and watching Korean dramas on your big TV definitely (did not) help with my paper preparation and thesis writing! **Xin**, thank you for all your extra help with spin-qubit knowledge. I've really enjoyed our coffee chats, hope everything is going well with Groove. I also want to thank all my friends and colleagues in QuRe and QuTech for the many chats, discussions, and shared moments that made this journey lighter and more enjoyable.

Thanks to the technical support team — without **Olaf** and **Jason**, our experiments would never have run so smoothly. I also owe similar gratitude to the staff at the **Kavli Nanolab**, who kept the equipment operational and made possible all the nanoelectronics work in my PhD.

Running has been such an important part of my life and connected me with so many friends over the past years. **Lukas** and **Christian**, you're definitely not forgotten! I'm so grateful we found each other in a similar pace range (well, Lukas can be way faster, but thanks for bearing with us :)). We've kept our group runs going for so long — Strava tells me it goes all the way back to September 2020 -

can you believe it?! Let's plan a *QuTech marathon prep* reunion someday!

Jin, I am truly grateful for all your cheerful messages whenever I was frustrated with setbacks, especially in the final year of my PhD. It's always fun hanging out with you in those mini-trips and and I'm glad to see you becoming an even stronger runner. Best of luck with the progress on your thesis and everything that follows! **Hong**, I'm always impressed by your cooking skills. Let's keep our tennis matches going, and good luck finishing your thesis writing.

When I was looking for the next position in 2024, I met Qblox. A big thanks to **Willemijn** who has given me a wonderful guide tour and share her experience with working. I have join the QSE team since November 2024 and I'm truly grateful to the whole team — **Adith, Roger, Ark, David, Chih-Hsien and Parahm** — who not only provide world-class technical support to our customers but have also been incredibly kind and generous in helping me develop myself. Many thanks!

I want to thank my **parents** for their unwavering support over all these years. Despite their limitations, ever since my bachelor studies they have always respected my important life choices and given me all the support they could. I wish them to stay healthy and happy.

Lastly, **Yihan**, I cannot imagine how the past few years would be like without those time spent with your presence, whether in real-life or virtually. With you by my side, I truly feel like the luckiest man in the world. I am looking forward to the years to come and 好好过日子。

Qingzhen Wang
Delft, August 2025

Curriculum Vitæ

Qingzhen Wang

1993/12/31	Born in Qingdao, China
2011 - 2015	**BEng in Materials Science and Engineering** Focus: Metallurgy and Ceramic Materials Xiamen University, China *Thesis*: The grain size dependence of Eu-doped Si_3N_4 on its fluorescence spectrum.
2015 - 2018	**MSc in Materials Science** Focus: Nanotechnology and Electronic Materials RWTH Aachen, Germany *External Thesis*: Transport properties of InSb selective-area growth nanowires: a new platform for scalable Majorana devices (Delft University of Technology, The Netherlands)
2018-2025	**PhD in Physics** Delft University of Technology, The Netherlands *Thesis*: Artificial Kitaev chains in Two-Dimensional Electron Gases Promotor: Prof.dr.ir. L.P. Kouwenhoven Co-promotor: Dr. Srijit Goswami

List of Publications

9. *Flux-controlled two-site Kitaev chain*
Ivan Kulesh†, Sebastiaan L. D. ten Haaf†, **Qingzhen Wang**, Vincent P. M. Sietses, Yining Zhang, Sebastiaan R. Roelofs, Christian G. Prosko, Di Xiao, Candice Thomas, Michael J. Manfra, and Srijit Goswami
Phys. Rev. Lett., 135, 056301 (2025)

8. *Observation of edge and bulk states in a three-site Kitaev chain*
Sebastiaan L. D. ten Haaf, Yining Zhang, **Qingzhen Wang**, Alberto Bordin, Chun-Xiao Liu, Ivan Kulesh, Vincent P. M. Sietses, Christian G. Prosko, Di Xiao, Candice Thomas, Michael J. Manfra, Michael Wimmer, and Srijit Goswami
Nature, 641, 890–895 (2025)

7. *A two-site Kitaev chain in a two-dimensional electron gas*
Sebastiaan L. D. ten Haaf†, **Qingzhen Wang**†, A. Mert Bozkurt, Chun-Xiao Liu, Ivan Kulesh, Philip Kim, Di Xiao, Candice Thomas, Michael J. Manfra Tom Dvir, Michael Wimmer and Srijit Goswami
Nature **630**, 329–334 (2024)

6. *Crossed Andreev Reflection and Elastic Cotunneling in Three Quantum Dots Coupled by Superconductors*
Alberto Bordin, Xiang Li, David Van Driel, Jan Cornelis Wolff, **Qingzhen Wang**, Sebastiaan L.D. Ten Haaf, Guanzhong Wang, Nick Van Loo, Leo P. Kouwenhoven, Tom Dvir
Phys. Rev. Lett. 132, 056602 (2024)

5. *Spatial dependence of local density of states in semiconductor-superconductor hybrids*
Qingzhen Wang, Yining Zhang, Saurabh Karwal and Srijit Goswami
Nano Letters, 24 (43), 13558-13563 (2024)

4. *Cross-Platform Autonomous Control of Minimal Kitaev Chains*
David van Driel, Rouven Koch, Vincent P. M. Sietses, Sebastiaan L. D. ten Haaf, Chun-Xiao Liu, Francesco Zatelli, Bart Roovers, Alberto Bordin, Nick van Loo, Guanzhong Wang, Jan C. Wolff, Grzegorz P. Mazur, Tom Dvir, Ivan Kulesh, **Qingzhen Wang**, A. Mert Bozkurt, Sasa Gazibegovic, Ghada

Badawy, Erik P. A. M. Bakkers, Michael Wimmer, Srijit Goswami, Jose L. Lado, Leo P. Kouwenhoven, and Eliska Greplova
arXiv:2405.04596 (2024)

3. *Triplet correlations in Cooper pair splitters realized in a two-dimensional electron gas*
Qingzhen Wang†, Sebastiaan L. D. ten Haaf†, Ivan Kulesh, Di Xiao, Candice Thomas, Michael J. Manfra and Srijit Goswami
Nature Communications, 14, 4876 (2023)

2. *InSbAs two-dimensional electron gases as a platform for topological superconductivity*
Christian M Möhle†, Chung Ting Ke†, **Qingzhen Wang**, Candice Thomas, Di Xiao, Saurabh Karwal, Mario Lodari, Vincent van de Kerkhof, Ruben Termaat, Geoffrey C Gardner, Giordano Scappucci, Michael J Manfra, Srijit Goswami
Nano Letters, 21 (23), 9990-9996 (2021)

1. *In-plane selective area InSb–Al nanowire quantum networks*
Roy L. M. Op het Veld†, Di Xu†, Vanessa Schaller, Marcel A. Verheijen, Stan M. E. Peters, Jason Jung, Chuyao Tong, **Qingzhen Wang**, Michiel W. A. de Moor, Bart Hesselmann, Kiefer Vermeulen, Jouri D. S. Bommer, Joon Sue Lee, Andrey Sarikov, Mihir Pendharkar, Anna Marzegalli, Stephan Koelling, Leo P. Kouwenhoven, Luciano Miglio, Chris J. Palmstrøm, Hao Zhang, and Erik P. A. M. Bakkers
Communications Physics 3, 59 (2020)

Included in this thesis.
† Equal Contribution.

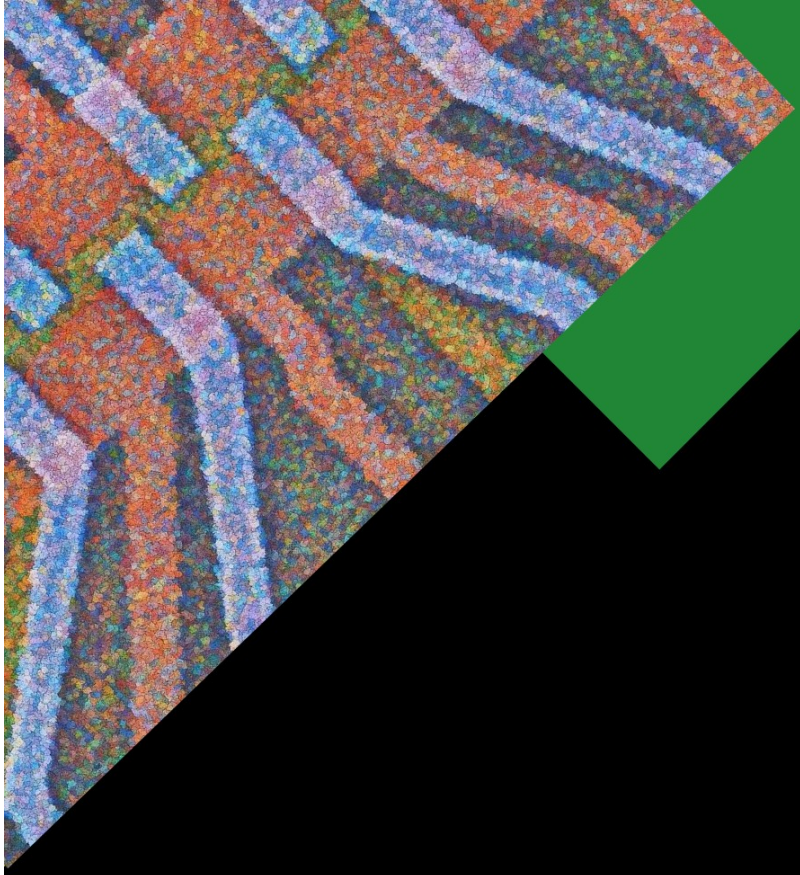

ISBN 978-94-6384-830-5